Passive Acoustic Array Modelling and Processing for a Wave-Propelled Unmanned Surface Vessel

Anthony Treloar, Alfie

Award date:
2022

Awarding institution:
University of Bath

Passive Acoustic Array Modelling and Processing for a Wave-Propelled Unmanned Surface Vessel

Anthony Treloar, Alfie

Award date:
2022

Awarding institution:
University of Bath

Passive Acoustic Array Modelling and Processing for a Wave-Propelled Unmanned Surface Vessel

submitted by

Alfred Oliver Anthony Treloar

for the degree of Doctor of Philosophy

of the

University of Bath

Mechanical Engineering

March 2022

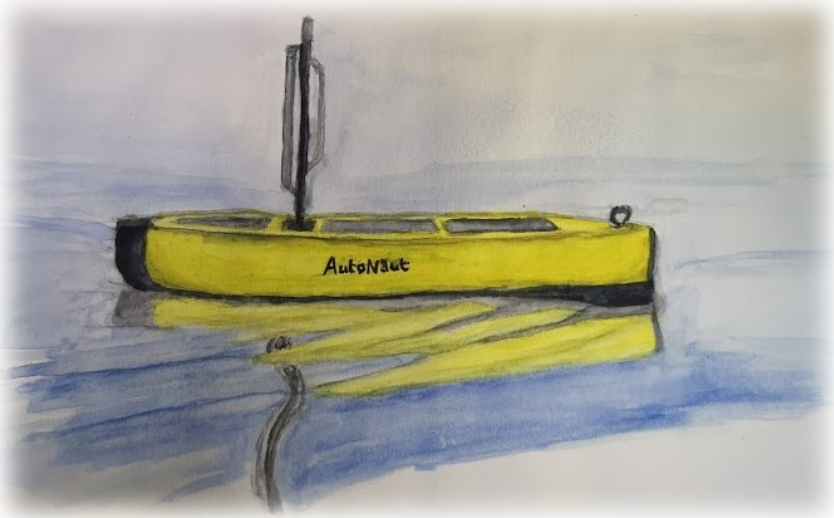
AutoNaut

Abstract

The AutoNaut USV is a novel wave-propelled vessel with a very low noise profile. As such, it is uniquely suited to passive acoustic monitoring, which can be carried out using a towed hydrophone array. However, the method of propulsion inherently presents some challenges to employing bearing estimation techniques by potentially exacerbating the uncertainty in array shape. The aim of this research is to investigate and demonstrate the capabilities of such a vessel, to quantify its performance and to evaluate the steps required to fully realise its potential.

A recursive Bayesian array shape estimation method was developed to combine the data from all available sensors on the array. This was tested and verified with simulated data and then used to estimate the motion of an array in operation during the Unmanned Warrior '16 trial. This trial data was used to demonstrate bearing estimation to a sound source, with an analysis of the performance increase from compensating for the perturbed shape. The outcomes of this were then used to investigate the optimal positioning of non-acoustic sensors on an array.

The main result was the successful demonstration of bearing estimation to a sound source from experimental data. The results of the array shape estimation process suggest that the array is tilted and periodically perturbed into a bowing shape with an amplitude of less than 0.1m. Compensating for this results in up to a 5.8dB increase in the output spectrum from the MUSIC bearing estimation algorithm.

While a perturbed array shape results in a slight drop in performance, a conclusion of this work is that the tilt on the array and the resulting detection of a multipath arrival presents a further challenge in interpreting the results. Nonetheless the research presented here represents a successful first step to enabling the AutoNaut's full capabilities.

Contents

Acknowledgements

Firstly, I'd like to thank my supervisor Alan Hunter for providing reliable and enthusiastic support. Although it hurts whenever the red pen comes out, it's always invaluable advice and feedback (and it probably hurts just as much as reading some of the stuff I give him). Thanks also to my examiners, Mike Warner and Manuchehr Soleimani, for a good discussion in my viva and some very helpful notes to improve my thesis.

I am extremely grateful to the EPSRC for providing funding for my PhD and to all of the people at Seiche Ltd. and Autonaut Ltd. for provision of the experimental dataset that is central to this thesis. Particular thanks go to Phil Johnston and Jan Bujalka for always being available for any questions and queries I have had along the way. I would also like to acknowledge the financial support from Seiche Ltd. allowing me to attend my first conference in Italy.

I'd like to thank Ciaran, Zo and Ben (The Sonar Guys) for making the office somewhere I actually enjoyed being rather than just a place of work. Also thanks for always enthusiastically helping out whenever I've needed a sounding board or am struggling with understanding a topic. The past year or so of isolation and writing have not been nearly as fun as the preceding few and I look forward to getting back to the pub with you all.

Finally I would like to thank all of my family and friends who have supported me so much throughout my life and especially over the past few years. Especially: Will, for providing welcome respite from writing and patiently sitting through my complaining; and my housemate, Tash, for putting up with my being a recluse and cheerleading whenever I enter the room. I'd like to thank my Dad, my BP Rupert, Chris, all my siblings. And lastly I'd like to express my most immense gratitude to my Mum for always pushing me to seize opportunities, encouraging me to do the things I enjoy and supporting me in whatever I chose to do.

Preface

The first three chapters of this thesis present the background and motivation for this work. The subsequent four chapters present novel contributions in the form of a simulation process, an array shape estimation algorithm, an experimental investigation and a simulated investigation.

The scope of this project changed a considerable amount with the Covid19 pandemic, resulting in fewer experimental datasets to work with. This has meant a slightly higher reliance on simulated data in the final work, but has resulted in the development of a more accurate, refined simulator.

Conferences

The work detailed in this thesis has been presented at a number of local and international conferences.

Conference Articles

- A. A. Treloar, A. J. Hunter, J. Bujalka and P. Johnston, "Passive Acoustic Monitoring Using a Towed Array from a Wave-Propelled USV" in *Proceedings of the Underwater Acoustics Conference and Exhibition (UACE)*, 2019 [Online]. Available: http://www.uaconferences.org/docs/2019_papers/UACE2019_831_Anthony%20Treloar.pdf

- B. W. Metcalfe, B. W. Thomas, A. A. Treloar, Z. Rymansaib, A. J. Hunter, and P. R. Wilson, "A compact, low-cost unmanned surface vehi cle for shallow inshore applications", in *Intelligent Systems Conference, IntelliSys*, 2017, pp. 961-968. [Online]. Available: https://ieeexplore.ieee.org/document/8324246

Conferences Presentations

- UK Acoustics Network (UKAN) Special Interest Group for Underwater Acoustics (SIGUA) PhD Student Symposium 2019 in Bath, UK
- Underwater Acoustics Conference and Exhibition (UACE) 2019 in Crete, Greece
- The 8th International Workshop on Detection, Classification, Localization, and Density Estimation of marine mammals using passive acoustics 2018 in Paris, France
- Centre for Innovative Ultrasound Solutions (CIUS) spring conference 2018 in Trondheim, Norway
- 4th Workshop on Military Applications of Underwater Glider Technology 2017 in La Spezia, Italy

Impact Statement

The outcomes from this work is being used to inform a current Knowledge Transfer Partnership project being undertaken by Ahsan Jafri with Seiche Ltd. and the University of Bath. This project is looking into the FPGA implementation of beamforming capabilities for persistent use from the Autonaut and the development process of the array for the project utilised the analysis tools and results presented in this thesis.

The simulator is also being used to predict system performance and inform experiment design in an ongoing Impact Acceleration Account (IAA) funded project with the University of Bath, Autonaut and Seiche Ltd.

List of Figures

List of Symbols

Symbol	Description	Unit
c	sound speed	m/s
$\mathbb{E}$	mathematical expectation	
f	frequency	Hz
$\mathcal{F}$	Fourier transform	
ϕ	phase	radians
k	hydrophone index	
K	number of hydrophones	
λ	acoustic wavelength	m
m	particle index	
M	number of particles	
$\mathcal{N}$	sample from continuous normal distribution	
n	time step	
NL	noise level	dB
ω	angular frequency	rad/s
P	power	W
p	pressure	Pa
$\mathbb{P}$	conditional probability	
ψ	pitch	^{o}
q	impinging wave index	
Q	number of impinging waves	
$\boldsymbol{R}$	covariance matrix	
σ	standard deviation	
SL	source level	dB
SNR	signal-to-noise ratio	dB
SPL	sound pressure level	dB
TL	transmission loss	dB
t	time	s

List of Symbols

Symbol	Description	Unit
τ	time delay or lag	s
θ	bearing	^{o}
$\mathcal{U}$	sample from continuous uniform distribution	

List of Acronyms

Acronym	Full term
ASW	anti-submarine warfare
AUV	autonomous underwater vehicle
CAPT	compass, attitude, pressure and temperature
CPSD	cross power spectral density
CRLB	Cramer Rao lower bound
CSM	cross-spectral matrix
dB	decibels
DFT	discrete Fourier transform
DOA	direction of arrival
DTLA	digital thin line array
ESPRIT	estimation of signal parameters via rotational invariance technique
FFT	fast Fourier transform
FNBW	first null beam width
FT	Fourier transform
HLA	horizontal line array
HPBW	half power beam width
IFT	inverse Fourier transform
MC	Monte-Carlo
MUSIC	multiple signal classification
MVDR	minimum variance distortionless response
NL	noise level
PAM	passive acoustic monitoring
PDF	probability density function
PHAT	phase transform
PSD	power spectral density
RL	receive level
RMS	root mean square

List of Acronyms

Acronym	**Full term**
SL	source level
SNR	signal-to-noise ratio
SPL	sound pressure level
SSP	sound speed profile
STFT	short-time Fourier transform
TL	transmission loss
ULA	uniform linear array
USV	uncrewed surface vessel
VLA	vertical line array

Chapter 1

Introduction

1.1 Passive Underwater Acoustic Sensing

The underwater environment presents a unique challenge for surveillance and monitoring of sound sources of interest. Due to the rapid attenuation of light in water, usual methods of visual tracking and detection are rendered mostly useless. However, acoustic waves travel roughly five times as fast and are significantly less attenuated [1]. As such, sound is of key importance to understanding and investigating the underwater environment, hence sonar being the most ubiquitous of underwater sensing modalities.

Sonar, which stands for *so*und *na*vigation and *r*anging, refers to use of sound propagation in order to navigate, or to detect other objects or vessels in the water. Unlike active sonar, which emits an acoustic wave and measures the response, passive sonar uses the sound generated by a source of interest to infer its identity or its location.

1.2 Applications

Passive sonar is an excellent tool for monitoring a sound-producing source in situations where it may not be desirable to produce any sound, with its application varying from environmental conservation, scientific and military uses.

1.2.1 Marine Mammal Monitoring

The vocal nature of marine mammals makes them excellent candidates for the use of passive sonar. Marine mammal enumeration and location tracking is not only important for environmental conservation studies to document their behaviour, it can also be preventative as in marine mammal mitigation zones. Seismic surveys and the naval use of high-powered active sonar have been linked to numerous cases of mass marine

mammal strandings [2][3][4][5] to the point where in certain instances it has resulted in government-imposed bans [6] and federal court cases [7]. Around all types of anthropogenic noise, from active sonar to offshore oil and gas developments, it is required to have a mitigation zone to reduce the impact of the loud sounds on the health of nearby marine mammals. This is a defined area in which the presence of a marine mammal will require the activity to cease. Often done through visual surface sighting when a whale breaches, the use of passive acoustic monitoring (PAM) provides a potentially more reliable and persistent tool to aid fulfilment of this requirement.

1.2.2 Port and Harbour Security

From a commercial and a defence point of view, ports and harbours are a point of weakness which hostile parties may look to exploit. As a location containing expensive equipment, sensitive data and cargo, and large numbers of personnel it is integral to have robust security measures in place. Divers entering unseen from the surface present a danger which can potentially be detected and tracked using passive sonar techniques on the acoustic emissions from their rebreathers [8].

1.2.3 Anti-Submarine Warfare

Also in a military context, anti-submarine warfare (ASW) is an application of passive sonar that has been around since the beginning of the 20th century. Vital to success in military conflicts involving submarines is the knowledge of the location and identity of enemy vessels. Passive sonar offers a method of gaining this information without highlighting the presence of or compromising the location of your own vessel.

1.3 Deployment methods

There are a number of different commonly used methods of deployment for a passive sonar system, each with their own advantages and disadvantages.

1.3.1 Bottom Deployed

Sea bed mounted hydrophones [9][10][11] are typically mounted on frames or anchored to the floor and attached to a short buoy to keep them in position. They are relatively inexpensive and can cover wide areas persistently. However, they are static, potentially difficult to accurately position and sometimes require retrieval for accessing the data, which can make them logistically more complicated to implement.

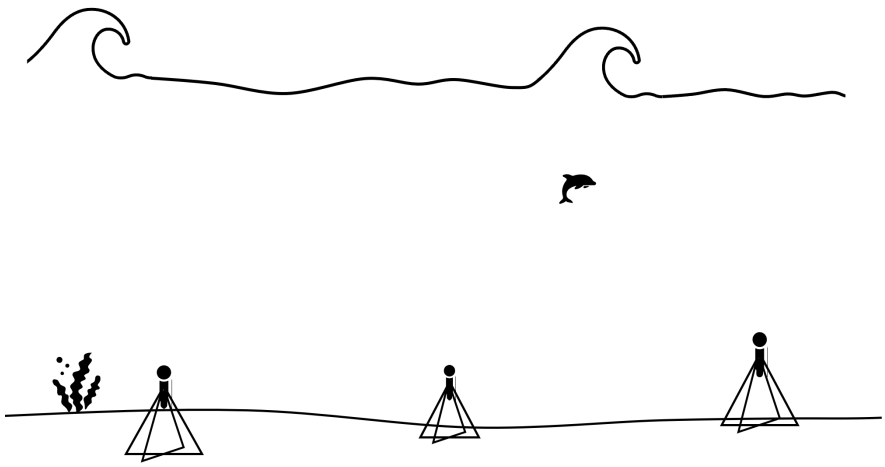

Figure 1-1: Bottom-deployed hydrophones

1.3.2 Buoy-Mounted

A slightly more mobile solution is known as a sonobuoy [12][11], introduced in the 1940s for ASW deployed from aircraft. One or more hydrophones is connected at a certain depth to a floating buoy, which gives them the advantage of being able to cover a variable area, and of better connectivity as the data can be transmitted via radio to a nearby crewed vessel. These are often expendable and deliberately sunk after a certain period of time, making them somewhat expensive and wasteful, as well as not having any active control over their position once deployed.

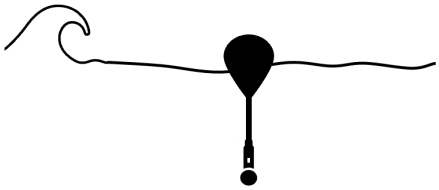

Figure 1-2: Buoy-mounted hydrophone

1.3.3 Towed

The most mobile style of deployment of passive sonar is a towed array behind a vessel. This method was originally developed during World War I [13] and is extremely ubiquitously used for many things from ASW to seismic surveys. They were developed to overcome the effects of vessel noise from hull-mounted hydrophones and also offer the benefit of increased array aperture. They are versatile and capable of monitoring

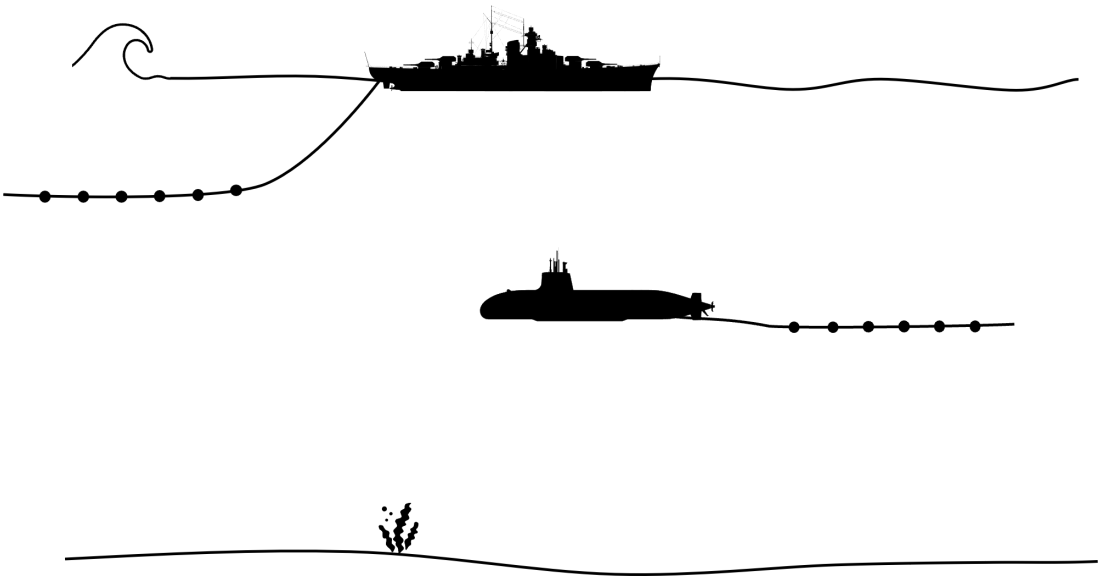

Figure 1-3: Towed array

a variable wide area. These arrays can range from tens of metres all the way up to multiple kilometres in length [13] and are typically deployed from large tow vessels such as ships and submarines. More recently, due to their rapidly improving capabilities, uncrewed autonomous vessels have started being more widely used, with tow vessels such as autonomous underwater vehicles (AUVs) [14][15] and uncrewed surface vessels (USVs) [16][17].

1.4 AutoNaut USV and Thin-Line Array

The AutoNaut wave-propelled USV, Figure 1-4, presents a novel tool for wide-area persistent passive acoustic monitoring. It fits somewhere between a sonobuoy and a standard tow vessel in terms of its capabilities, with convenient deployment and autonomous operation. Combined with renewable power for sensor payloads, it offers reduced risk and cost compared to crewed vessels, and is capable of mission durations up to months in length [17]. The low acoustic profile of the propulsion method makes them uniquely suited to passive acoustics as self-noise is much less of an issue than is typically the case with towed arrays deployed from powered vessels.

The Seiche digital thin line array (DTLA) was developed as a low-profile array to reduce drag and allow deployment from lower-power vessels. It is tens of metres in length and can be configured for up 32 hydrophones, making it a perfect companion to the AutoNaut for passive acoustic monitoring.

Figure 1-4: AutoNaut Uncrewed Surface Vessel [18]

There are, however, some inherent challenges to implementing passive acoustic monitoring techniques from a towed array behind a wave-propelled USV. The method of propulsion exacerbates the problem of array shape uncertainty, potentially introducing problems for localisation algorithms which require accurate knowledge of the sensor positions. This can lead to sub-optimal performance, inaccuracies and mis-detections. In addition to this, the limited tow power also necessitates a shorter array which has implications on the tow depth and operating frequencies at which the array can be used.

1.5 Aims and Objectives

The aim of the research presented in this thesis is:

To investigate and demonstrate passive acoustic monitoring capabilities from a wave-propelled uncrewed surface vessel

To this end the following objectives will be completed:

1. Array shape estimation algorithm
   (a) Develop a method to estimate array shape from Autonaut trial data, as the array is too long for a controlled experiment in a water tank
   (b) Use the method to quantify array shape in the field

2. Perform passive array beamforming on trial data
    (a) Demonstrate that bearing estimation is feasible from this vessel
    (b) Quantify the performance
    (c) Quantify improvement offered by array shape estimation
3. Develop simulation model
    (a) Incorporate the array motion
    (b) Model a sound source
    (c) Capture accurate acoustic propagation
    (d) Validate against experimental data
4. Use the model to investigate array designs
    (a) Non-acoustic sensor placement
    (b) Propose optimal design for a future array

1.6 Thesis Outline

The thesis is structured with Chapters 2 and 3 presenting the relevant background theory and literature:

Chapter 2 covers the fundamental acoustic theory required to understand the content of this thesis, spanning acoustic signals, Fourier domain analysis and underwater propagation.

Chapter 3 describes the techniques used in the processing of hydrophone arrays. An exploration of bearing estimation methods is presented with an analysis of their performance. This leads into a review of the approaches to the challenge of array shape estimation and an examination of their applicability to a wave-propelled vessel.

The novel contributions are introduced in Chapter 4, 5, 6 and 7, as follows:

Chapter 4 presents the developed simulation process for both acoustic and non-acoustic data, and the simulated datasets used in subsequent chapters are introduced.

Chapter 5 describes the development of the particle filtering based array shape estimation process with an analysis of its application to simulated data. This objective is an especially relevant topic for a morphing sensor array, as is the case here, with ongoing active research into this field in defence research [19].

Chapter 6 describes the experimental data from the Unmanned Warrior '16 trial. This data is then used as experimental validation for the simulation process introduced in Chapter 4. Finally, the results of applying the array shape estimation algorithm presented in Chapter 5 are assessed and examined, as well as the results of applying various bearing estimation algorithms.

Chapter 7 details a simulated study on the optimal configuration of non-acoustic sensors for an array in the absence of acoustic data, using the tools developed in Chapter 4 and Chapter 5.

Chapter 8 presents the conclusions and findings of this work, as well as suggestions for follow-on work.

Chapter 2

Fundamentals of Underwater Acoustics

This section describes the underwater acoustics theory and concepts required to understand this thesis.

2.1 Acoustic Waves

Acoustic waves are mechanical vibrations that travel through a medium. In water they propagate as a longitudinal pressure wave, alternately compressing and expanding the medium. Mathematically their propagation is described by the scalar wave equation which describes the local pressure deviation in time and space [20],

$$\frac{\partial^2 p}{\partial t^2} - c^2 \frac{\partial^2 p}{\partial \boldsymbol{x}^2} = 0 \tag{2.1}$$

where p is the local pressure deviation from ambient, t is time, x is the spatial coordinate and c is the speed of sound. This is derived through linearisation and manipulation of the continuity equation, the Navier-Stokes equation and the general heat transfer equation, and assumes a quiescent fluid medium. One of the most simple solutions to this equation is known as d'Alembert's solution. In 1-D the general solution is

$$p(x,t) = F(x - ct) + G(x + ct) \tag{2.2}$$

where F and G are arbitrary functions, determined by the boundary and initial conditions. This solution describes both the wave in the positive direction (the F function) and the negative direction (the G function), so to allow a general orientation of the

coordinate system, the pressure for a free field plane wave can be written as

$$p(x,t) = F(nx - ct) \tag{2.3}$$

where n is a unit vector describing the direction of propagation. A time harmonic plane wave of frequency, f, is usually written [20] in complex form as Equation 2.4.

$$p(x,t) = A(x,t)e^{j(2\pi ft - 2\pi fx/c + \varphi)} \tag{2.4}$$

where A is the amplitude and φ is some arbitrary starting phase. The physical quantity is described by the real part of this function. Splitting up the exponent into a signal term and a propagation term results in Equation 2.5.

$$p(x,t) = A(x,t)\underbrace{e^{j(2\pi ft+\varphi)}}_{\text{signal}}\underbrace{e^{j(-2\pi fx/c)}}_{\text{propagation}} \tag{2.5}$$

Abbreviating the signal term to $s(t)$ and using the angular frequency, $\omega = 2\pi f$, we arrive at the simplified 1D wave equation for a monochromatic plane wave, Equation 2.6.

$$p(x,t) = A(x,t)s(t)e^{-j(\omega x/c+\varphi)} \tag{2.6}$$

2.1.1 Frequency and Wavelength

The frequency of a wave is the number of full periods of oscillation occurring per second, expressed in Hz. The relation between the frequency and the wavelength of an acoustic wave can be described as

$$f = \frac{c}{\lambda} \tag{2.7}$$

where λ is wavelength in m and c is propagation speed in m/s, which is dependent on the medium (expanded upon in Section 2.3.2). This can also be expressed as angular frequency, ω in rad/s, which is related to frequency as

$$\omega = 2\pi f \tag{2.8}$$

2.1.2 Phase Angle

The phase angle specifies in radians where in its cycle the wave is at some reference point (typically at $t = 0$). A sine wave starting at $t = 0$ would be described as having a phase of zero whereas one starting at a quarter of a wavelength would have a phase of $\frac{\pi}{2}$ rad, all the way up to a phase of 2π rad which would be brought forward a full

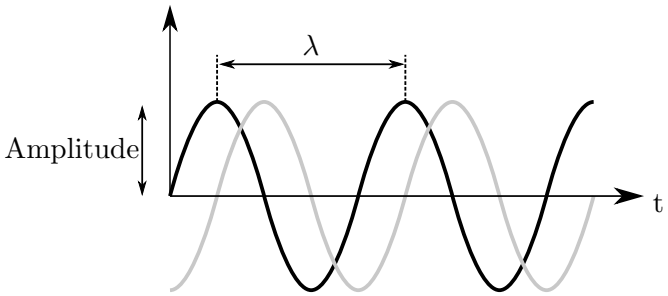

Figure 2-1: Sinusoidal waves with a $\pi/2$ phase offset between them

cycle. This angle can be used to describe the offset between two sinusoids of the same frequency, as shown in Figure 2-1, where the grey sinusoid is offset from the black by a phase of $-\frac{\pi}{2}$ rad.

2.1.3 Amplitude

The amplitude of a wave is the peak deviation from zero. In acoustics, this is defined as the deviation from the hydrostatic pressure of the medium and is often expressed in decibels (dB) as the sound pressure level (SPL),

$$\mathrm{SPL} = 10\log\left(\frac{{p_{\mathrm{rms}}}^2}{{p_{\mathrm{ref}}}^2}\right) = 20\log\left(\frac{p_{\mathrm{rms}}}{p_{\mathrm{ref}}}\right) \tag{2.9}$$

where p_{rms} is the root mean square (RMS) value of the pressure deviation and p_{ref} is the reference pressure which, for underwater applications, is assigned a value of 1μPa.

2.1.4 Fourier Domain Representation

More complicated waveforms can be described using a decomposition into monochromatic waves, as illustrated in Figure 2-2 where the signal on the left is composed of the three on the right. The Fourier transform (FT) is a mathematical operation which decomposes a function into its constituent frequencies. For a function of time, this will result in a complex-valued series of frequency components. Their magnitudes represent the amount of that frequency in the original signal and their angles are the phase offset of that frequency. This is defined as

$$\mathcal{F}\{u(t)\} = U(f) = \int_{-\infty}^{\infty} u(t)e^{-j2\pi ft}dt \tag{2.10}$$

where $u(t)$ is the function of time and $U(f)$ is the resulting FT spectrum, a function of frequency. $\mathcal{F}$ is used to denote the Fourier transformation. Conversely, the function

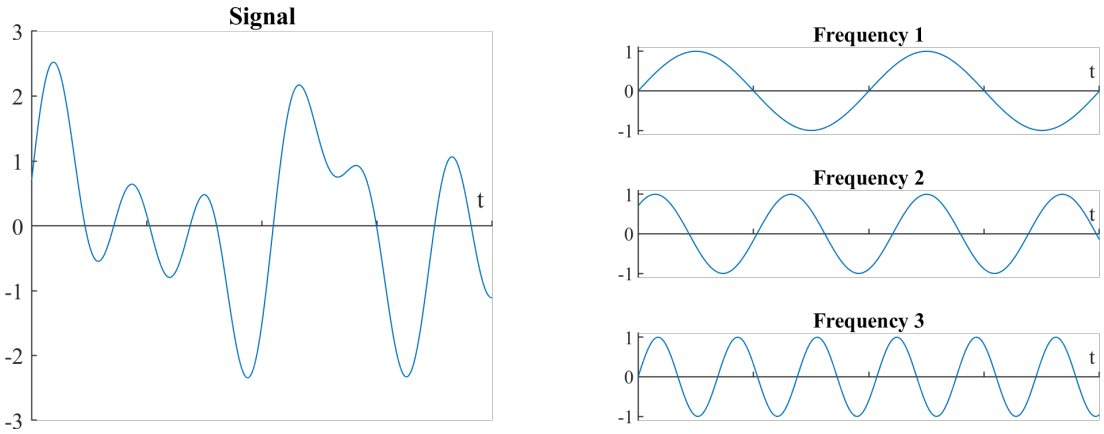

Figure 2-2: Example signal made up of three sinusoids

$u(t)$ can be obtained from $U(f)$ through an inverse Fourier transform (IFT), as defined in Equation 2.11.

$$\mathcal{F}^{-1}\{U(f)\} = u(t) = \int_{-\infty}^{\infty} U(f)e^{j2\pi ft}df \tag{2.11}$$

In practice, the time series data will be finite is length and discretely sampled in time, therefore the discrete Fourier transform (DFT) operation is used, defined as

$$U(k) = \sum_{n=0}^{N-1} u(n)e^{-j2\pi kn/N}, \quad k = 0, \ldots, N-1 \tag{2.12}$$

This is most commonly implemented using the efficient fast Fourier transform (FFT) implementation. This converts the finite sequence, $u(n)$, into the equal length sequence, $U(k)$. The number of points used for the DFT, N, determines the frequency resolution of the resulting spectrum, defined as f_s/N, i.e. the larger the number of points, the better the resolution (limited by the number of data points available).

Another limitation of discretely sampled data is a phenomenon known as the Nyquist-Shannon sampling theorem, which states that any frequency component above half the sampling frequency(known as the Nyquist frequency) is indistinguishable from a lower frequency component [21]. This is illustrated for two discretely sampled sinusoids in Figure 2-3, where one sinusoid is at a frequency, f_1, below the Nyquist frequency and then the higher frequency sinusoid is at $f_s + f_1$.

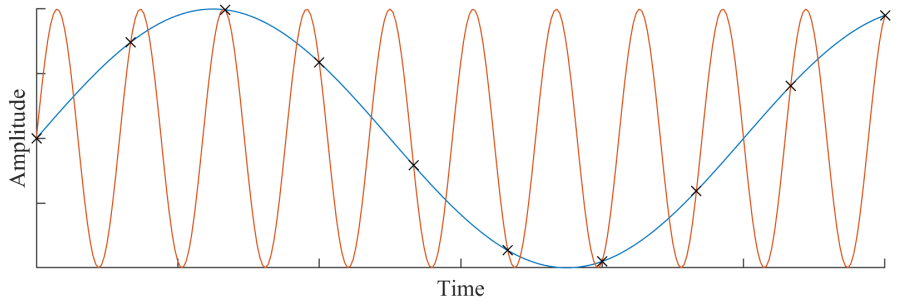

Figure 2-3: Aliasing illustration, with "x" denoting the sampling points

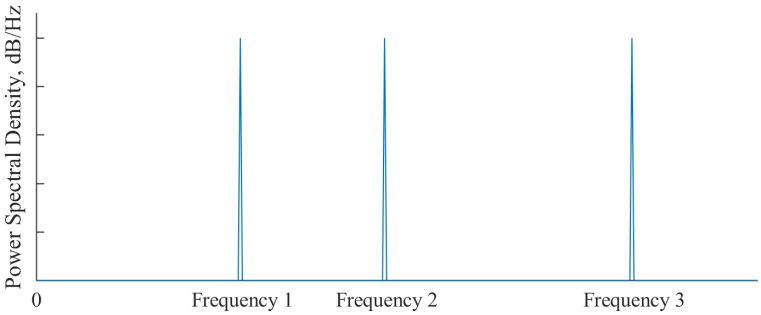

Figure 2-4: Illustrative frequency decomposition for the case presented in Figure 2-2

2.1.4.1 Fourier Domain Time Shifting

A basic property of the FT is the principle that a shift in the time domain of τ is interpreted as a complex phase shift in the Fourier domain, as in Equation 2.13.

$$\mathcal{F}\{u(t-\tau)\} = e^{-j2\pi f\tau}U(f) \tag{2.13}$$

2.1.4.2 Power Spectral Density

The power spectral density (PSD) is a measure of the signal's power versus frequency, defined as

$$S_{uu}(f) = \lim_{T\to\infty} \frac{1}{T} |U_T(f)|^2 \tag{2.14}$$

It is useful for characterising a signal's frequency content and can be can be visualised in a PSD plot. For example, the Figure 2-4 would be the simplified PSD plot of the example in Figure 2-2, with a spike in magnitude at each of the frequencies. This is useful for analysing the frequency content of data and can be used to detect the presence of a signal. In real data there's some frequency content at all frequencies, as in the example shown in Figure 2-5, which shows the PSD of a recording of a humpback whale call.

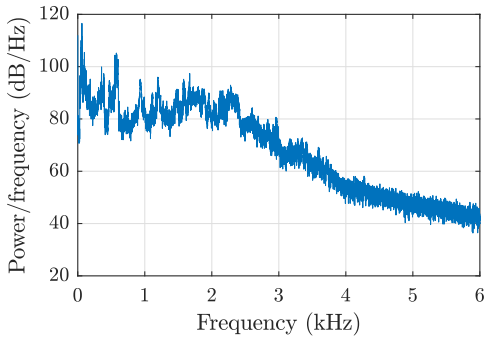

Figure 2-5: Example PSD plot(Humpback whale call [22])

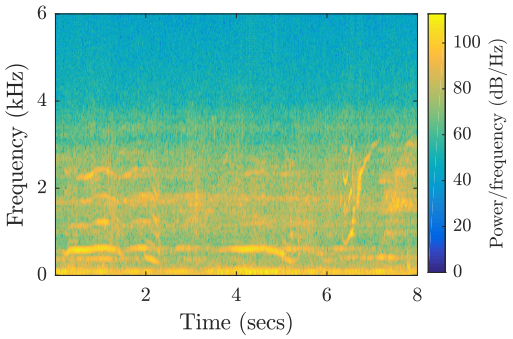

Figure 2-6: Example spectrogram (Humpback whale call [22])

2.1.4.3 Short-Time Fourier Transform

It is often useful to view how the frequency content changes as a function of time, which can be computed using a short-time Fourier transform (STFT). This splits the data into overlapping, windowed subsequences and computes each of their FTs,

$$U(\tau, f) = \int_{-\infty}^{\infty} u(t)w(t-\tau)e^{-i2\pi ft}dt \tag{2.15}$$

where $u(t)$ is the data being transformed and $w(t-\tau)$ is the window function used to reduce artefacts at the edges of each data segment (often a Hann window). As previously stated, the length of the subsequences relates to the frequency resolution (larger FT, better resolution). However, it also relates to the temporal resolution, so clearly there is a compromise that needs to be made when selecting the parameters for a STFT [23].

The power estimate of the STFT, is known as a spectrogram and can show the time-varying frequency component magnitudes, useful for the detection of signals and visualising data. The spectrogram of the same humpback whale call can be seen in Figure 2-6, showing the frequency modulation in its call.

2.2 Passive Sonar Equation

Central to the theory for passive sonar is the passive sonar equation. It provides a systematic way of computing the signal-to-noise ratio (SNR) [24] which describes whether a sound source will be detected given the propagation of the emitted wave and the noise present in the scenario.

The sound source radiates a signal with a source level (SL), a measure of the SPL at a distance of 1m. This is reduced in intensity by a transmission loss (TL) from the sound propagating through the water to the receiver, resulting in the signal receive level (RL),

$$\mathrm{RL} = \mathrm{SL} - \mathrm{TL} \tag{2.16}$$

Finally, the SNR is computed as a ratio of this RL to the noise level (NL) at the receiver. As all the quantities are in dB this is computed as another subtraction, resulting in the passive sonar equation for a single hydrophone:

$$\mathrm{SNR} = \mathrm{SL} - \mathrm{TL} - \mathrm{NL} \tag{2.17}$$

The following two sections will go into more detail on the estimation of the propagation losses and the causes of noise.

2.3 Acoustic Wave Propagation

2.3.1 Propagation Losses

There are several mechanisms by which the amplitude of an acoustic wave is reduced as it travels. The two main mechanisms of TL are through geometric spreading and absorption.

$$\mathrm{TL} = \mathrm{TL}_{\mathrm{geom}} + \mathrm{TL}_{\mathrm{absorption}} \tag{2.18}$$

2.3.1.1 Geometric Spreading Loss

The geometric spreading loss occurs because as an acoustic wave travels further from its source, its power is spread over a larger area, defined as a ratio of intensities:

$$\mathrm{TL}_{\mathrm{geom}} = 10 \log_{10} \left(\frac{I_0}{I} \right) \tag{2.19}$$

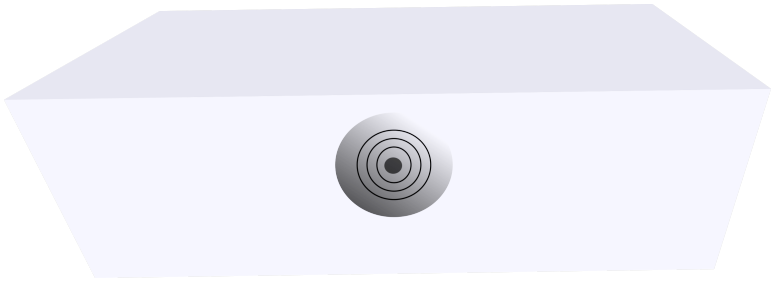

Figure 2-7: Spherical spreading

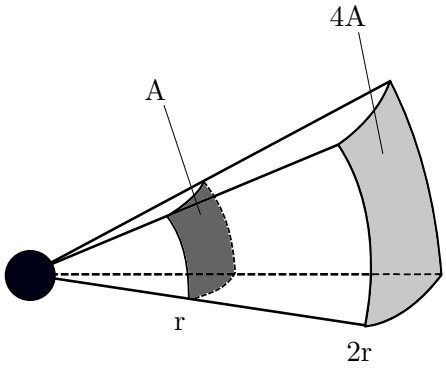

Figure 2-8: Illustration of the increased surface area from spherical geometric spreading loss

where I is the acoustic intensity, defined as the power, P, per unit area, A, as in Equation 2.20, and I_0 is the source acoustic intensity at $r = 1$m.

$$I = \frac{P}{A} \tag{2.20}$$

Spherical spreading assumes the sound is propagating uniformly in all directions, illustrated in Figures 2-7 and 2-8. Inserting the formula for the area of a sphere in Equation 2.20 results in

$$I = \frac{P}{4\pi r^2} \tag{2.21}$$

showing that the area the source power, P, is spread over changes as a function of r^2. The ratio of intensities then becomes

$$\frac{I_0}{I} = \frac{4\pi P r^2}{4\pi P r_0^2} = \frac{r^2}{r_0^2} \tag{2.22}$$

and with $r_0 = 1$, Equation 2.19 is equal to $10\log_{10}(r^2) = 20\log_{10}(r)$.

After a certain range, spherical spreading can no longer be assumed accurate as the sound waves will be reflected from the sea surface and the seafloor. A simple

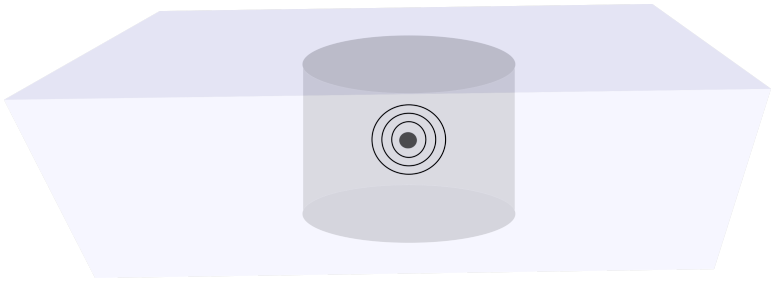

Figure 2-9: Cylindrical spreading

approximation is therefore to assume that the sound power is distributed uniformly over the surface of a column of height h, i.e. $A_{\text{cyl}} = 2\pi hr$. Illustrated in Figure 2-9, this is known as cylindrical spreading and leads to an equation where TL_{geom} varies proportional to r, resulting in half the spreading loss of the spherical case.

$$\text{TL}_{\text{geom}} = \begin{cases} 20\log_{10} r & \text{if spherical} \\ 10\log_{10} r & \text{if cylindrical} \end{cases} \tag{2.23}$$

where TL is the transmission loss in dB and r is the distance the wave has travelled in m.

2.3.1.2 Absorption Loss

The other term in Equation 2.18 is the absorption loss of the transmission medium, which varies depending on frequency, temperature, salinity, acidity and pressure. This is caused by energy absorption from particle motion and from chemical excitation. The range dependant coefficient, α, can be calculated using an accurate empirically-derived formula, shown in Equation 2.24 [25], which can then be used to predict the attenuation over the distance.

$$\alpha = \alpha_1 + \alpha_2 + \alpha_3 \tag{2.24}$$

with the boric acid contribution

$$\alpha_1 = 0.101 \frac{f_1 f^2}{f_1^2 + f^2} e^{(pH-8)/0.57} \tag{2.25}$$

$$f_1 = 0.91 \left(\frac{S}{35}\right)^2 e^{T/33} \tag{2.26}$$

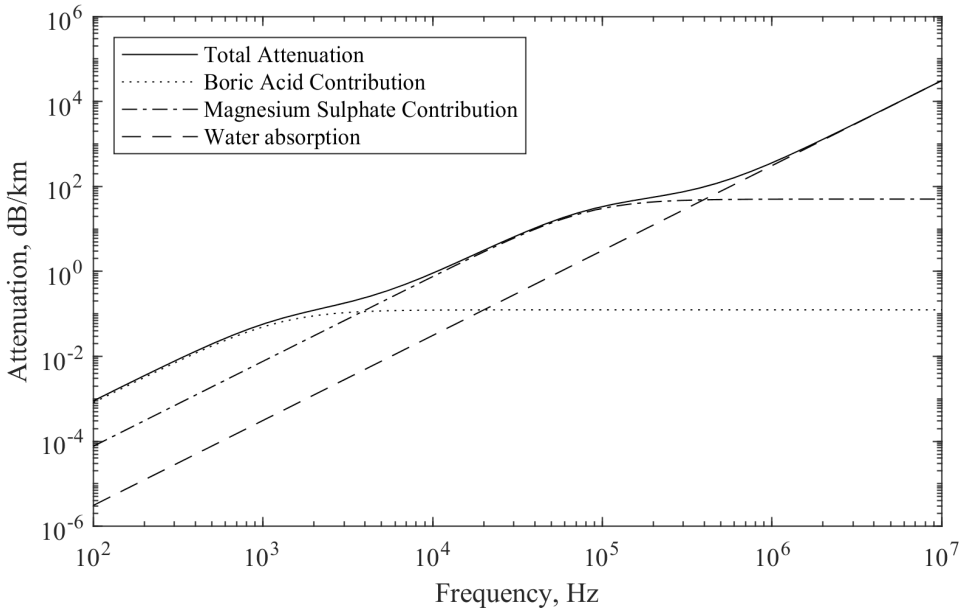

Figure 2-10: Attenuation due to absorption for representative conditions of depth = 100m, pH = 8, salinity = 35ppt and temperature = 10^{o}C, with the respective contributions from boric acid, magnesium sulphate and water

the contribution from magnesium sulphate

$$\alpha_2 = 0.56\left(1+\frac{T}{76}\right)\left(\frac{S}{35}\right)\left(\frac{f_2 f^2}{f_2^2+f^2}\right)e^{-z/4.9} \tag{2.27}$$

$$f_2 = 46.6e^T/18 \tag{2.28}$$

and finally the freshwater absorption

$$\alpha_3 = A_3 P_3 f^2 \tag{2.29}$$

$$A_3 = 4.937\times10^{-4} - 2.59\times10^{-5}T + 9.11\times10^{-7}T^2 - 1.5\times10^{-8}T^3, \quad \text{for } T \leq 20^oC \tag{2.30}$$

$$A_3 = 3.964\times10^{-4} - 1.146\times10^{-5}T + 1.45\times10^{-7}T^2 - 6.5\times10^{-10}T^3, \quad \text{for } T > 20^oC \tag{2.31}$$

$$P_3 = 1 - 3.83\times10^{-2}z + 4.9\times10^{-4}z^2 \tag{2.32}$$

where f is the frequency(kHz), pH is the acidity, S is the salinity in ppt, T is the temperature in ^{o}C and z is the depth(km).

The resulting attenuation coefficient, α, is in dB/km and can be used to estimate

the propagation loss due to absorption as

$$\mathrm{TL}_{\mathrm{absorption}} = \alpha r \times 1{\times}10^{-3} \tag{2.33}$$

Figure 2-10 shows how the attenuation coefficient varies with frequency for some representative conditions. As can be seen, the attenuation from absorption is less than 1dB/km for all frequencies below 10kHz, indicating that the geometric spreading will dominate the transmission loss at low frequencies.

2.3.2 Refraction and the Sound Speed Profile

The propagation speed of an acoustic wave is a property of the transmission medium. For sea water this varies between roughly 1450m/s and 1570m/s based on the temperature (T), salinity (S) and pressure (p) [26]. For typical conditions of $T = 10°$, $S = 35$ and $p = p_{\mathrm{atm}}$, a value of $c = 1490$m/s can be used [27].

In practice, these three properties vary with depth beneath the surface of the sea, resulting in a non-linear sound speed profile (SSP), an example of which is shown in Figure 2-11. At the sea surface, the effect of water temperature dominates, hence the higher sound speed that comes with higher temperature. As the temperature gradually decreases towards 1km depth, the sound speed also decreases. This then increases with depth as the temperature levels off and pressure increases, causing an increase in sound speed.

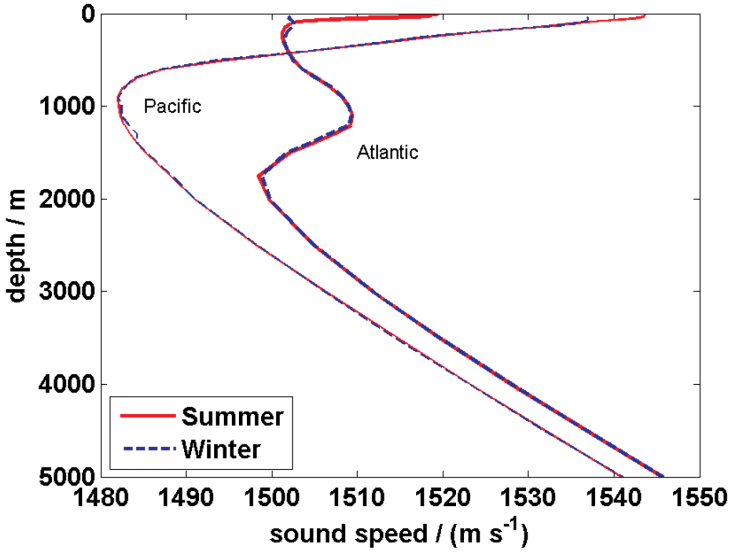

Figure 2-11: Non-linear sound speed profile for the Pacific ocean and the Atlantic ocean [28]

A variation in sound speed is important to take into account when considering underwater acoustic propagation as it causes acoustic waves to refract and follow a curved path between source and receiver [29]. There are numerous phenomena which arise from this. One often exploited is known as the SOFAR channel, which is a horizontal layer of water whose axis is at the depth where the sound speed is at its minimum. The bending of the acoustic waves back towards this depth results in a region in which low frequency sound waves can travel for many more kilometres than they otherwise would. In certain other circumstances it can also be a detriment, such as a surface duct. If the sound speed is decreasing towards the surface, as is typical in winter conditions, sound is refracted upwards and can become trapped near the surface.

2.3.3 Multipath Reflections

Not only does an acoustic wave potentially travel in a curved path between source and receiver, but it can also travel to it via multiple separate paths. The wave can reflect off the sea floor and the sea surface a number of times before reaching the receiver. This is referred to as multipath propagation, with the 0^{th} order path being direct, the 1^{st} order path having reflected off only one surface, 2^{nd} order off two surfaces etc. as illustrated in Figure 2-12. Typically the higher order the multipath, the weaker the signal as some energy is usually lost in each reflection and in the extra distance travelled.

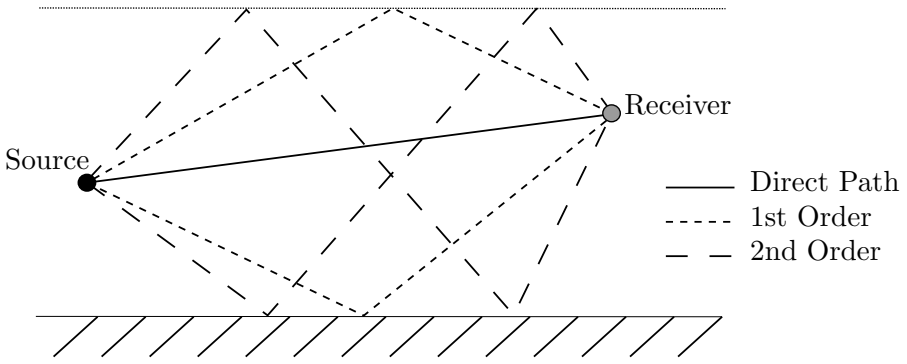

Figure 2-12: Illustration of direct path and first and second order multipaths

The arrival of the same signal can complicate the received signal's information. For example, a sound arriving at a receiver via both direct paths and a surface reflection produces a phenomenon know as the Lloyd's mirror interference patterns [30]. The arrivals of the two signals on the receiver cause constructive or destructive interference based on the relative position of the source, resulting in an interference pattern. This has implications for the detectability of a signal.

2.3.4 Propagation Models

The complicated propagation characteristics of underwater sound are often modelled using a number of different methods [31][32]. The sound field underwater can be described using the time-independent form of the wave equation, known as the Helmholtz equation:

$$\left(\nabla^2 + \frac{\omega^2}{c^2}\right) \phi(\mathbf{r}, \omega) = 0 \tag{2.34}$$

where ∇^2 is the Laplace operator. Each method uses different assumptions and techniques to find solutions to this equation to obtain an estimate of the wavefield.

2.3.4.1 Ray Tracing

The most intuitive method, known as ray tracing, follows the trajectory of individual rays of sound from the source and determines the pressure along these lines using the solution to the wave equation introduced in Equation 2.4. A system of ray equations is used to compute the curvature and beamwidth of each ray as a function of arc length [33].

Given launching angles, the source position and the sound speed, this results in an amplitude function and a phase function which can be coherently summed at a point of interest for many simulated rays to estimate the TL [34]. This also captures the effects of different angles of arrival from source to receiver and the effects of reflections off the seabed and sea surface. A commonly used implementation of this is the Bellhop program [35] which has been implemented efficiently in Fortran, Matlab and Python, in conjunction with the Bounce model to include the effects of seafloor reflections [33]. Unlike the other methods listed, Bellhop can be used relatively efficiently with broadband signals [36] as you can use the time difference of arrival to estimate the propagation of multiple frequencies simultaneously.

2.3.4.2 Normal Mode Theory

Normal mode theory considers the wave equation as range and depth dependent functions, assuming all the energy is trapped as stationary waves in the waveguide between the seabed and the sea surface [37]. The acoustical field in the vertical direction is generated as a sum of normal modes, taking into account soundspeed and density discontinuities. The method used to estimate it in the horizontal direction depends on the range-dependence of the environment, with increasing complexity for increasing range-dependence [32]. The number of modes to include in the solution scales linearly with frequency making this method well-suited for low frequencies.

2.3.4.3 Parabolic Equation Models

Parabolic equation methods derive a solution from the Helmholtz equation considering only the outgoing wave, reducing it to an initial value problem. The wave field is then calculated to the required distance step-by-step [32]. The computational requirements increase with the square of the frequency so this method is generally used for frequencies of <1kHz.

2.4 Ambient Noise

Any acoustic waves received by a hydrophone that are not signals of interest can be considered noise. The background, or ambient, noise in the ocean varies with frequency and location due to a wide range of causes, depicted in Figure 2-13. These vary from natural physical processes, marine life and anthropogenic sources, and can be split into three approximate frequency bands.

2.4.1 Low Frequency(10Hz-500Hz)

The reduced attenuation of low frequency sound causes the SPL of ambient noise to be significantly greater at lower frequencies. Occupying this low frequency range are natural and biological sources such as large marine mammals and seismic waves from earthquakes. However, the anthropogenic contributions are increasingly prevalent, due to the vast increase in shipping activity. Although natural noise sources have remained fairly constant, commercial shipping ambient noise levels in the ocean have increased by about 3.3dB per decade for the past 70 years [38].

2.4.2 Medium Frequency (500Hz-25kHz)

In the medium frequency range, the dominant source of natural ambient noise is ocean surface waves, depending on the sea state [39]. Precipitation can have a large effect too, causing a marked increase towards the higher frequency end of the band for rainfall and with a very broad peak at 3kHz [40]. Anthropogenic noise such as active sonar, small boats and machinery also contribute. Another very troublesome source of noise are snapping shrimp, which are present in various bays around the world. They produce extremely loud, broadband noise which spans the entire spectrum and makes acoustic measurement of other sources in the vicinity all but impossible [41].

2.4.3 High Frequency (>25kHz)

At very high frequencies the attenuation of sound is extremely high, therefore any noise sources will be in the immediate vicinity of the receiver. Nearby active sonar and marine mammals' echolocation calls [42] are the main sources of sound at these frequencies, with thermal noise being the other contributor. When all other noise sources have been removed, the only remaining sound is the thermal agitation of seawater molecules which puts the limit on acoustic detection sensitivity.

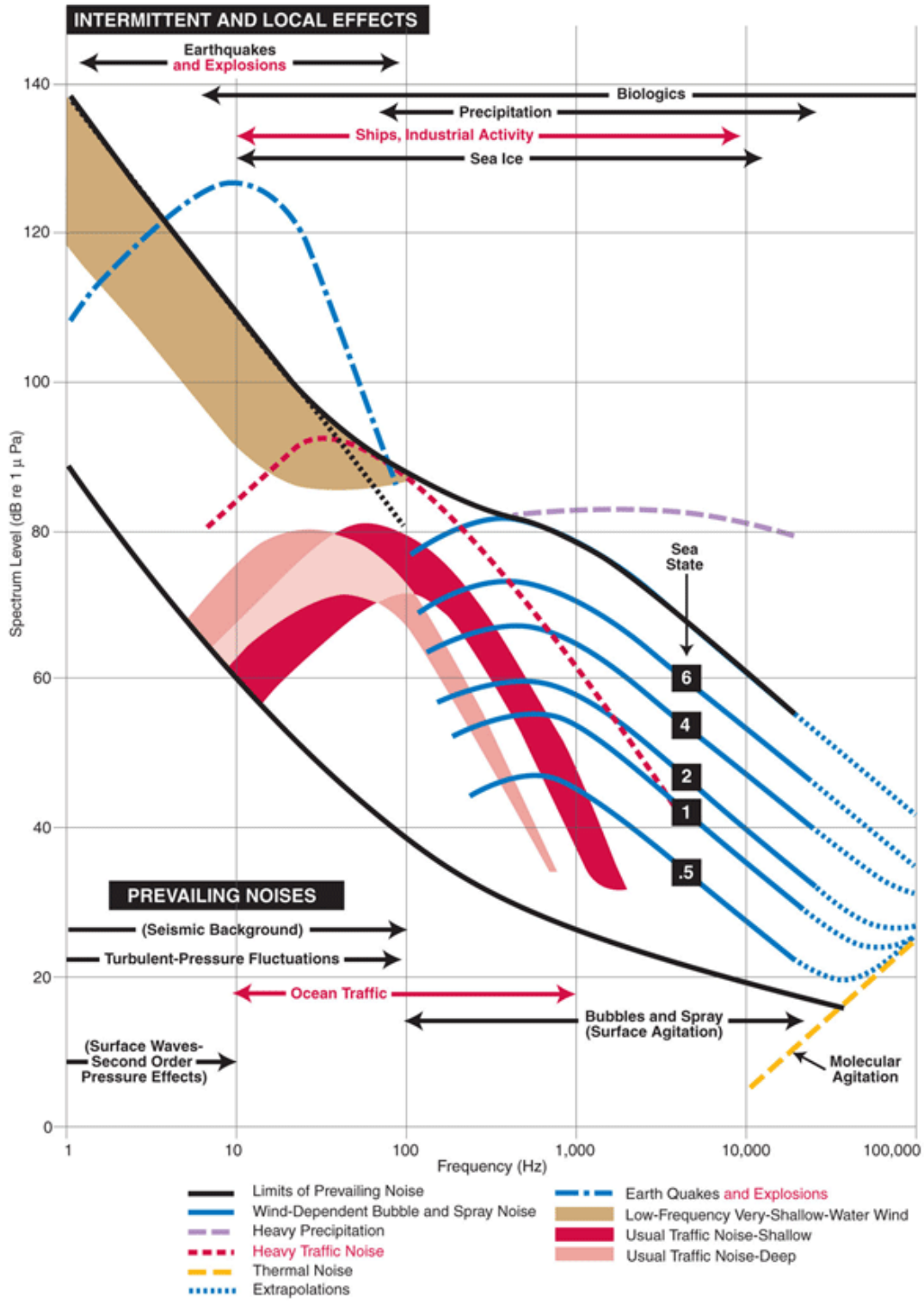

Figure 2-13: Wenz Curve [43], originally from [44]

Chapter 3

Passive Array Processing

An array of hydrophones offers certain benefits over the use of a single hydrophone. Through the application of processing algorithms it is possible to spatially filter the data to increase the SNR of a signal of interest, enumerate the number of sources with impinging signals and estimate the bearing to these sources.

3.1 Bearing Estimation

For a plane wave from a sound source in the far field, a linear array allows estimation of the bearing to a target sound source through the use of direction of arrival (DOA) estimation algorithms. There are various literature reviews of DOA algorithms [45][46][47][48][49][50], which highlight some of the most prominent methods of estimation. These algorithms are presented here, with examples of their use and an assessment of their advantages, disadvantages and suitability to the problem.

3.1.1 Cross-Correlation

A simple but fundamental processing method using two sensors, the cross-correlation can provide an estimate of the DOA to an impinging sound source using the data from two hydrophones and knowledge of their relative locations. The core concept relies on the assumption that a wavefront will be registered by the closest hydrophone at a certain point in time and then by the second hydrophone at a later point in time. The cross-correlation, defined in Equation 3.1, gives a measure of the similarity between two signals as a function of the lag, τ, of one signal relative to the other.

$$r_{12}(\tau) = \frac{1}{T-\tau}\int_{\tau}^{T} u_1(t)u_2(t-\tau)\mathrm{d}t \tag{3.1}$$

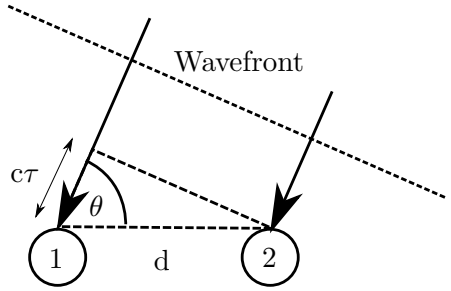

Figure 3-1: Geometric considerations to estimate DOA from the time delay

where T is the observation interval, τ is the lag or time delay between the signals, and u_m is the time series data received on the m^{th} hydrophone. This function can then be used to provide an estimate of the time difference of arrival between the two hydrophones using the location of the maximum:

$$\tilde{\tau} = \underset{\tau}{\text{argmax}}\{r_{12}(\tau)\} \tag{3.2}$$

Using this estimated time delay, a direction to the impinging sound source can be estimated using trigonometry, as in Figure 3-1,

$$\theta = \cos^{-1}\left(\frac{c\tilde{\tau}}{d}\right) \tag{3.3}$$

where c is the propagation speed, d is the inter-sensor distance and $\tilde{\tau}$ is the estimate for the inter-sensor time delay.

Equivalently, the cross-correlation can be computed in the Fourier domain. Using the fact that complex conjugation in the Fourier domain is equivalent to a time reversal in the time domain, cross-correlation can be computed as

$$S_{12}(f) = U_1(f)U_2(f)^* \tag{3.4}$$

where $U(f) = \mathcal{F}\{u(t)\}$ and * refers to the complex conjugate. This is termed the cross power spectral density (CPSD). This is linked to the PSD described in the previous chapter except it describes the relationship between the frequency content of two signals.

The cross-correlation can then be computed using the inverse Fourier transform of this function:

$$r_{12}(\tau) = \mathcal{F}^{-1}\{G_{12}(f)\} \tag{3.5}$$

The point at which this function reaches a maximum provides an estimate of the time

delay.

Another related concept is coherence. The coherence[1] function, $C_{12}(f)$, is a measure of how closely one signal corresponds to another at each frequency and is defined as

$$C_{12}(f) = \frac{|S_{12}(f)|^2}{S_{11}(f)S_{22}(f)} \tag{3.6}$$

where $S_{11}(f)$ and $S_{22}(f)$ are the auto-PSD for $u_1(t)$ and $u_2(t)$ respectively. This will vary between 0 and 1 for any given f, with 1 being perfect coherence.

This Fourier domain formulation of the cross-correlation function allows the use of weights to be applied to modify the shape of the $r_{12}(\tau)$ function [51][52], leading to the generalised cross-correlation function, G_{12} in Equation 3.7.

$$G_{12}(f) = U_1(f)U_2(f)^*W(f) \tag{3.7}$$

where $W(f)$ is the weighting function. As before, the cross-correlation function is computed as $r_{12}(\tau) = \mathcal{F}^{-1}\{G_{12}(f)\}$.

The choice of weighting function depends on the specific characteristics of the signals and noise, but the most commonly applied is the phase transform (PHAT) weighting [50][53][10], where the weighting is equivalent to the reciprocal of the cross-spectrum magnitude,

$$G_{\text{PHAT}}(f) = \frac{U_1(f)U_2(f)^*}{|U_1(f)U_2(f)^*|} \tag{3.8}$$

This leaves only the phase information and has the effect of reducing the spreading of the correlation peak, but is found not to perform well in channels dominated by multipath [54].

The cross-correlation method is often only used for source localisation with widely-spaced sparsely distributed hydrophones [55][56][9] or small arrays with few hydrophones [57]; however, the concepts involved provide the building blocks for the processing algorithms of even larger multi-sensor arrays.

3.1.2 Array Signal Model

The subsequent multi-sensor array processing methods described all assume a commonly used narrowband model which arises through consideration of the acoustic wave equation, described in Section 2.1, extended into the x and y dimensions for each sensor [46]. The wavefield measured at a receiver due to a narrowband source from a given

[1] Technically this is the magnitude-squared coherence but the two terms are used interchangeably

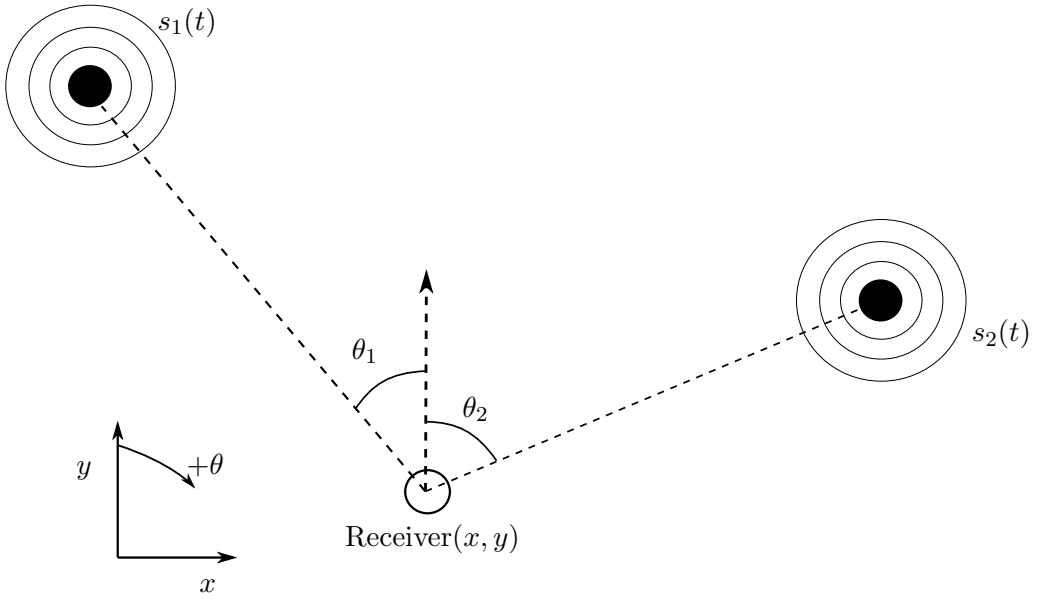

Figure 3-2: Illustration of a sensor and two sources in 2D

bearing can be described as in Equation 3.9.

$$u_q(t) = \exp(-j\omega(x \sin\theta_q + y \cos\theta_q)/c) s_q(t) \tag{3.9}$$

$$= a(\theta_q) s_q(t) \tag{3.10}$$

where x and y are the Cartesian co-ordinates of the receiver, $s_q(t)$ describes the signal for source q and θ_q is its bearing, measured clockwise from the positive y direction (North) as in Figure 3-2.

The steering factor, $a(\theta)$, can then be formed for each sensor and grouped into the steering vector. Placing sensor one at the origin and defining the rest of the sensors' positions relative to it results in a steering vector generalised to arbitrary array geometries, as

$$\boldsymbol{a}(\theta) = \left[\; 1, \quad \exp(-j\omega r_1(\theta)/c), \quad \ldots, \quad \exp(-j\omega r_K(\theta)/c) \; \right]^{\mathrm{T}} \tag{3.11}$$

where $r_k(\theta) = x_k \sin\theta + y_k \cos\theta$, and K is the number of sensors.

For Q sound sources each at their own respective bearings, this can be extended to a vector of signal waveforms and a steering matrix, as in Equations 3.12 and 3.13 respectively.

$$\boldsymbol{s}(t) = \left[\; s_1(t), \quad \ldots \quad s_Q(t) \; \right]^{\mathrm{T}} \tag{3.12}$$

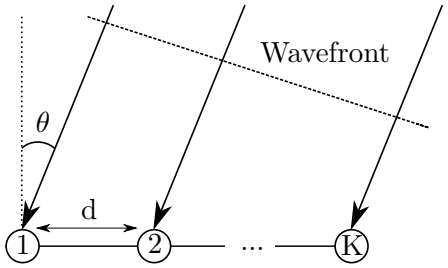

Figure 3-3: Uniform line array

$$\boldsymbol{A} = \begin{pmatrix} a_1(\theta_1) & a_1(\theta_2) & \dots & a_1(\theta_Q) \\ a_2(\theta_1) & a_2(\theta_2) & \dots & a_2(\theta_Q) \\ \vdots & \vdots & \ddots & \vdots \\ a_K(\theta_1) & a_K(\theta_2) & \dots & a_K(\theta_Q) \end{pmatrix} \tag{3.13}$$

Including an additive white noise vector term, $\boldsymbol{n}(t)$, this then results in the final array data model for multiple narrowband sources in the same frequency band, Equation 3.14.

$$\boldsymbol{u}(t) = \boldsymbol{A}\boldsymbol{s}(t) + \boldsymbol{n}(t) \tag{3.14}$$

3.1.3 Covariance Matrix

Building upon the cross-correlation theory discussed earlier in this chapter, the covariance matrix[2], $\boldsymbol{R}$, is of core importance to array processing. It describes the relationship between the signals received on each of the sensors with that of every other sensor. Along the diagonal is the variance of each sensor with the off-diagonal elements being the covariances of each sensor pair:

$$\boldsymbol{R} = \begin{pmatrix} r_{1,1} & r_{1,2} & \dots & r_{1,K} \\ r_{2,1} & r_{2,2} & \dots & r_{2,K} \\ \vdots & \vdots & \ddots & \vdots \\ r_{K,1} & r_{K,2} & \dots & r_{K,K} \end{pmatrix} \tag{3.15}$$

where $r_{1,2}$ is the covariance between the 1st and 2nd sensor. The lower triangle of off-diagonal elements are equal to the complex conjugate of those in the upper triangle ($r_{1,2} = r^*_{2,1}$), hence the matrix is always Hermitian (equal to its own conjugate transpose).

[2]Also known as the spatial covariance matrix, cross-covariance matrix or sample covariance matrix

Mathematically the covariance matrix is defined as

$$\boldsymbol{R} = \mathbb{E}\{\boldsymbol{u}(t)\boldsymbol{u}^H(t)\} \tag{3.16}$$

$$= \boldsymbol{A}\mathbb{E}\{\boldsymbol{s}(t)\boldsymbol{s}^{\mathrm{H}}(t)\}\boldsymbol{A}^{\mathrm{H}} + \mathbb{E}\{\boldsymbol{n}(t)\boldsymbol{n}^{\mathrm{H}}(t)\} \tag{3.17}$$

where $\mathbb{E}\{\}$ denotes the statistical expectation. Simplifying the signal covariance matrix, $\mathbb{E}\{\boldsymbol{s}(t)\boldsymbol{s}^H(t)\}$, to $\boldsymbol{S}$ and the noise covariance matrix, $\mathbb{E}\{\boldsymbol{n}(t)\boldsymbol{n}^H(t)\}$ to $\sigma^2\boldsymbol{I}$ this results in the following

$$\boldsymbol{R} = \boldsymbol{A}\boldsymbol{S}\boldsymbol{A}^{\mathrm{H}} + \sigma^2\boldsymbol{I} \tag{3.18}$$

where σ^2 is the variance of the noise and $\boldsymbol{I}$ is the identity matrix.

In a practical application the covariance matrix is not known and there is limited discretely sampled data. Therefore in practice, an estimate of the cross power spectral density matrix is used, or cross-spectral matrix (CSM) for short. This can be estimated a number of ways and a commonly used technique is Welch's method [58]. The STFT of the data is taken to produce the complex valued observations for each frequency, ω, at each time step, n, which are then averaged across time to produce a statistically consistent estimate of the true CSM which takes into account correlations from multiple sources [59]. Note, this is the same as the intermediate step when computing a cross-correlation in the Fourier domain, except computed for all sensor pairs.

$$\hat{\boldsymbol{R}}(\omega) = \frac{1}{N}\sum_{n=1}^{N}\boldsymbol{U}(n,\omega)\boldsymbol{U}^{\mathrm{H}}(n,\omega) \tag{3.19}$$

where N is the total number of observations, $\boldsymbol{U}(n,\omega)$ is the STFT data from each sensor and $^{\mathrm{H}}$ denotes the conjugate transpose. This produces a $K \times K$ CSM for each frequency. For continuous estimation of time-varying signals, a moving average can be used which will result in a CSM for each time step and at each frequency, $\hat{\boldsymbol{R}}(n,\omega)$.

3.1.4 Beamforming

Beamforming is a term for steering the transmission or reception of a sensor array. By weighting the received data from each sensor in such a way that they coherently sum in a desired direction one can increase the gain of impinging signals from that bearing. The output signal from beamforming a narrowband signal at frequency, ω, in a given direction, θ, is given by

$$y(t,\theta,\omega) = \sum_{p=1}^{P} w_k^{\mathrm{T}}(\theta,\omega)u_k(t,\omega) = \boldsymbol{w}^{\mathrm{H}}(\theta,\omega)\boldsymbol{u}(t,\omega) \tag{3.20}$$

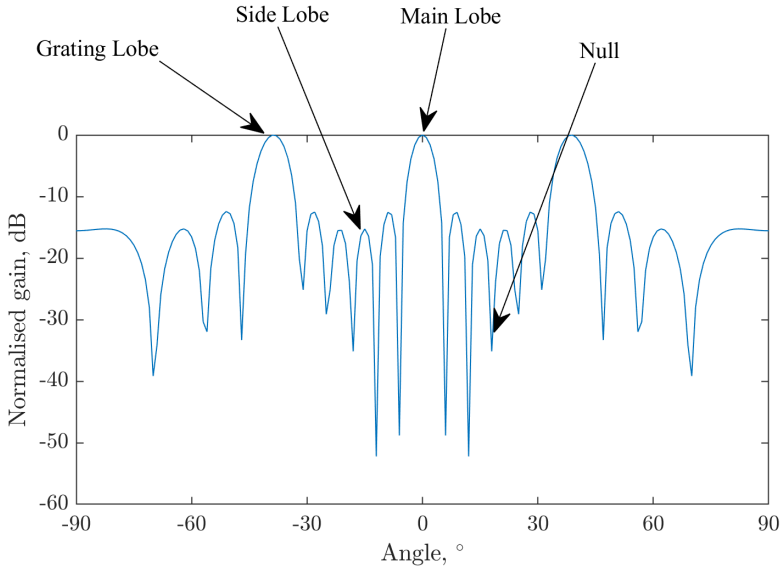

Figure 3-4: Illustration explaining beampattern terminology for a six-sensor array at a single frequency steered to 0^o

where $\boldsymbol{w}(\theta, \omega)$ is the vector of complex-valued weights applied to steer the beam in the direction θ and modify the beampattern and u_k is the k^{th} sensor's data. The estimated output power in a given direction can therefore be estimated as

$$\begin{aligned} P(\theta, \omega) = \mathbb{E}\{|y(t, \theta, \omega)^2|\} &= \boldsymbol{w}^{\mathrm{H}}(\theta, \omega)\mathbb{E}\{\boldsymbol{u}(t, \omega)\boldsymbol{u}^{\mathrm{H}}(t, \omega)\}\boldsymbol{w}(\theta, \omega) \\ &= \boldsymbol{w}^{\mathrm{H}}(\theta, \omega)\boldsymbol{R}(\omega)\boldsymbol{w}(\theta, \omega) \end{aligned} \tag{3.21}$$

3.1.4.1 Array Response

An important feature of the power estimates of DOA algorithms is the angular and frequency dependency of the produced spatial spectrum, which will affect the ability to resolve a target in space. This is described as a beampattern, illustrated for a single frequency in Figure 3-4. The main lobe is the maximum power peak in the steered direction, with grating lobes which are ambiguities caused by spatial undersampling. Then there are side lobes, which are lower gain peaks at other bearings, and nulls, which are the minima in between peaks, both of which are a function of the array aperture.

Beampattern Assuming a planar incoming wave, the beampattern can be computed for a given frequency by computing the expected phase differences based on the array

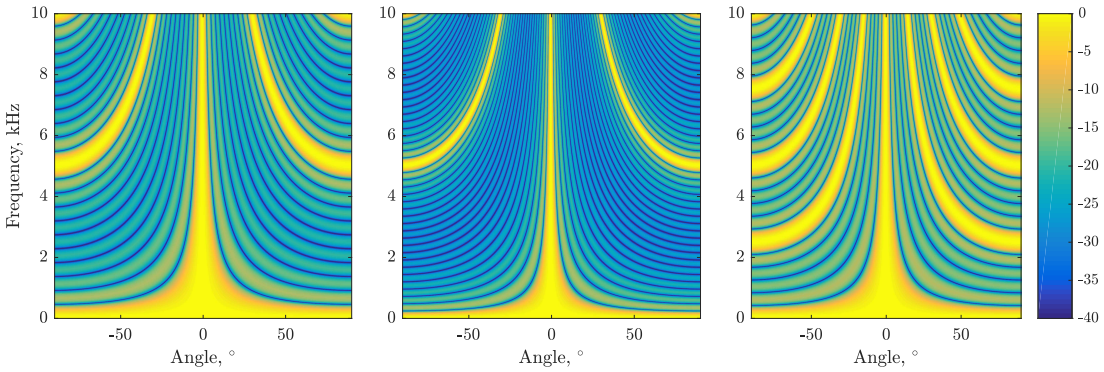

(a) d, L (b) $d, 2L$ (c) $2d, L$

Figure 3-5: Example array response with spacing d and array length L for a range of angles and frequencies

geometry and summing,

$$G(\theta) = 20\log_{10}\left(\frac{1}{K}\sum_{k=0}^{K-1} e^{j2\pi fkd\sin(\theta)/c} e^{j2\pi fkd\sin(\phi)/c}\right) \tag{3.22}$$

where K is the number of sensors, f is the frequency, d is the inter-sensor distance, θ is the beamsteering angle, ϕ is the angle and c is the speed of sound. When computed for multiple frequencies this can be viewed as a frequency response plot, examples of which are shown in Figure 3-5.

Main Lobe The main lobe width can be described using either the half power beam width (HPBW), the width of the beam at half the maximum gain, or the first null beam width (FNBW), the angle between the first nulls either side of the main lobe, described for a broadside detection in Equations 3.23 and 3.24 [60].

$$\text{HPBW} = 0.891\frac{c}{dKf} \tag{3.23}$$

$$\text{FNBW} = 2\frac{c}{dKf} \tag{3.24}$$

As can be seen in Figure 3-5, this results in a decrease in the bearing resolution as frequency decreases.

Side Lobes With an increasing numbers of equally-spaced sensors, K, the number of side lobes increases and the level of the side lobes decreases, as illustrated in Figures 3-5a and 3-5b. The peak of the first side lobe occurs either side of the main lobe at an

angle of

$$\theta_{\mathrm{s}} = \pm\frac{3\pi}{K} \tag{3.25}$$

with a gain of

$$G\left(\pm\frac{3\pi}{K}\right) \approxeq \frac{1}{K\sin\left(3\pi/2K\right)} \tag{3.26}$$

Grating Lobes The concept for grating lobes is the spatial equivalent to the Nyquist-Shannon sampling theorem, described in Section 2.1.4. In this case, it depends on the wavelength of the frequency of interest and the spatial sampling. Grating lobes occur when the wavelength of the signal is a multiple of the distance travelled between sensors in the direction of the wave:

$$\theta = \sin^{-1}\left(\frac{nc}{fd}\right) \tag{3.27}$$

where θ is the perceived bearing of the nth grating lobe. Similarly Equation 3.28 shows the maximum inter-sensor spacing to avoid aliasing at a given frequency [60].

$$d = \frac{c}{f(1+\sin(\theta))} = \frac{\lambda}{1+\sin(\theta)} \tag{3.28}$$

Thus, a spacing of $\lambda/2$ results in a beampattern that will not alias at any steer direction.

Ambiguity The final point to note on array response is that for a linear array, there is a rotational ambiguity about the axis of the array, as illustrated in Figure 3-6. This results in an inability to determine with confidence the precise DOA to a sound source without other knowledge. In practice a towed linear array will be nominally horizontal, which reduces it to a left-right ambiguity for incoming horizontal plane waves.

3.1.4.2 Conventional Beamformer (Bartlett)

The most basic beamforming algorithm is the conventional, or Bartlett [61], beamformer. This uses weights equivalent to the steering vector for the angle and frequency of interest, as in Equation 3.29. Note, the denominator of this weight is purely for scaling, to limit the output gain to unity.

$$\boldsymbol{w}_{\mathrm{bartlett}}(\theta,\omega) = \frac{\boldsymbol{a}(\theta,\omega)}{\sqrt{\boldsymbol{a}^{\mathrm{H}}(\theta,\omega)\boldsymbol{a}(\theta,\omega)}} \tag{3.29}$$

This weighting results in the power estimate,

$$P_{\mathrm{bartlett}}(\theta,\omega) = \frac{\boldsymbol{a}^{\mathrm{H}}(\theta,\omega)\hat{\boldsymbol{R}}(\omega)\ \boldsymbol{a}(\theta,\omega)}{\boldsymbol{a}^{\mathrm{H}}(\theta,\omega)\boldsymbol{a}(\theta,\omega)} \tag{3.30}$$

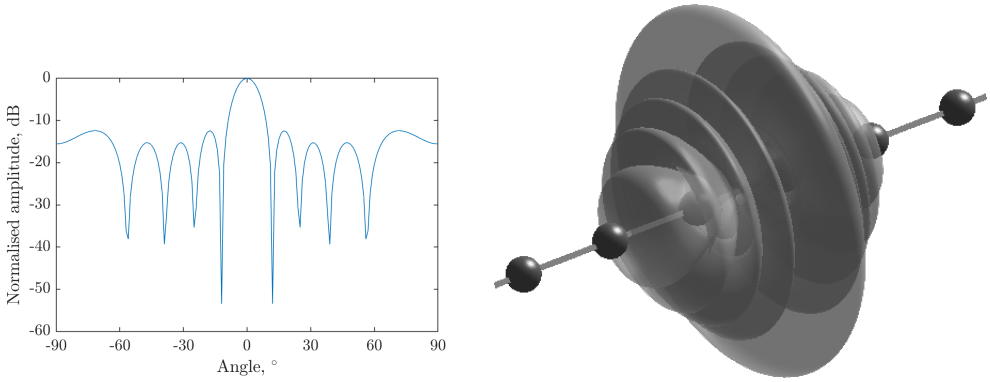

(a) (b)

Figure 3-6: Example array response in 2D (a) with corresponding 3D response (b) showing the rotational ambiguity

This method is very commonly used due to its ease of implementation. However, it suffers from a broad main lobe in its beampattern, especially at low frequencies. That and the relatively prominent sidelobes limit its capability to resolve closely spaced sound sources.

3.1.4.3 Capon's Beamformer

Capon's beamformer, commonly referred to as minimum variance distortionless response (MVDR), is the most notable extension to conventional beamforming. As opposed to the conventional algorithm which simply maximises the power in a desired direction, MVDR attempts to reduce the noise power in all other directions while maintaining the power in the steered direction [62]. This results in the weighting,

$$\boldsymbol{w}_{\text{mvdr}}(\theta,\omega) = \frac{\hat{\boldsymbol{R}}^{-1}(\omega)\boldsymbol{a}(\theta,\omega)}{\sqrt{\boldsymbol{a}^{\text{H}}(\theta,\omega)\hat{\boldsymbol{R}}^{-1}(\omega)\boldsymbol{a}(\theta,\omega)}} \tag{3.31}$$

The use of the data to adapt the weights in order to provide the estimate puts this in a category known as adaptive beamforming.

Inserting this into Equation 3.21 results in the power estimate for Capon's beamformer,

$$P_{\text{mvdr}}(\theta,\omega) = \frac{1}{\boldsymbol{a}^{\text{H}}(\theta,\omega)\hat{\boldsymbol{R}}^{-1}(\omega)\boldsymbol{a}(\theta,\omega)} \tag{3.32}$$

This provides a significant improvement in the beampattern with a reduction in the magnitude of the sidelobes and a narrower mainlobe width compared to the conventional beamformer, improving its capability to resolve closely spaced sources, as

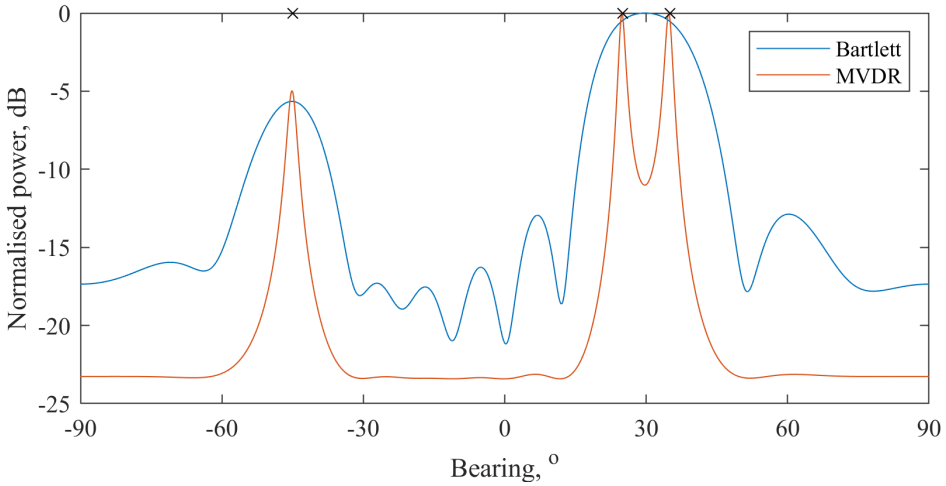

Figure 3-7: Comparison of the conventional beamformer and the MVDR beamformer with three sources at various bearings(denoted by the "x"s) for a 10 sensor uniform linear array (ULA) with spacing $\lambda/2$ and an SNR of 20dB

shown in Figure 3-7. This is at the cost of computational efficiency as the algorithm requires inversion of the covariance matrix. The potential for such a significant increase in performance has inspired a lot of research into developing extensions and principles to aid the design of an optimal adaptive beamformer [63]. It is very commonly used, with experimental examples on a number of arrays, stationary [8], towed [64] and volumetric [65].

The main causes of degradation in performance for this algorithm are inaccurate estimation of the covariance matrix and uncertainty in the steering vector. Inaccurate estimates of the covariance matrix from computation with limited samples can result in significant degradation in performance, potentially rendering it worse in performance than the conventional beamformer. This can happen as a result of the matrix becoming singular and therefore not able to be accurately inverted. A common remedy for such a situation is a method known as diagonal loading [66][67], where some value is added to the diagonal elements of the covariance matrix. A sensible method for selecting such a value is the standard deviation of the diagonal elements of the covariance matrix [68] as in Equation 3.33, which can be used as an indication of the covariance matrix error.

$$\gamma_{\mathrm{DL}} = \mathrm{std}(\mathrm{diag}(\hat{\boldsymbol{R}})) \tag{3.33}$$

where γ_{DL} is the diagonal loading value and std denotes the standard deviation. This is incorporated into the beamforming process by adjusting the covariance matrix prior

to beamforming,

$$\tilde{\boldsymbol{R}} = \hat{\boldsymbol{R}} + \gamma_{\mathrm{DL}}\boldsymbol{I} \tag{3.34}$$

where $\boldsymbol{I}$ is the identity matrix. Another proposed method is termed spatial smoothing and involves averaging across subarrays in the covariance matrix [69], in order to make the matrix full rank.

The characteristics of the noise environment also have an effect on the SNR increase from applying the MVDR beamformer. For example, reverberant conditions tend to significantly reduce the SNR gain [70].

3.1.5 MUSIC and Other Subspace Algorithms

While similar in implementation to beamforming algorithms, subspace algorithms, such as the popular multiple signal classification (MUSIC) algorithm [71], are slightly different in concept to the beamforming algorithms already described. As opposed to a power maximisation or minimisation, they arise through considering the geometric structure of the covariance matrix. The concept is that the eigendecomposition of the covariance matrix, as described in Equation 3.35, can be split into two subspaces: a signal subspace, with eigenvectors $\boldsymbol{V}_s$ and eigenvalues $\boldsymbol{\Lambda}_s$, and a noise subspace, with eigenvectors $\boldsymbol{V}_n$ and eigenvalues $\boldsymbol{\Lambda}_n$, as in Equation 3.37.

$$\boldsymbol{R} = \boldsymbol{A}\boldsymbol{S}\boldsymbol{A}^{\mathrm{H}} + \sigma^2\boldsymbol{I} \tag{3.35}$$

$$= \boldsymbol{V}\boldsymbol{\Lambda}\boldsymbol{V}^{\mathrm{H}} \tag{3.36}$$

$$= \boldsymbol{V}_s\boldsymbol{\Lambda}_s\boldsymbol{V}_s^{\mathrm{H}} + \boldsymbol{V}_n\boldsymbol{\Lambda}_n\boldsymbol{V}_n^{\mathrm{H}} \tag{3.37}$$

The MUSIC algorithm uses the fact that the covariance matrix is necessarily Hermitian and therefore symmetric, meaning the set of eigenvectors, $\boldsymbol{V}$, is guaranteed to be an orthogonal matrix. Assuming there are Q incident waves on the array, the subspace spanned by the eigenvectors corresponding to the largest Q eigenvalues can be denoted as the signal subspace and the noise subspace spanned by the $K-Q$ remaining eigenvectors. Minimising the Euclidean distance between the steering vector and the noise subspace can then provide a spatial pseudo-spectrum for DOA estimation,

$$P_{\mathrm{MUSIC}}(\theta,\omega) = \frac{1}{\boldsymbol{a}^{\mathrm{H}}(\theta,\omega)\boldsymbol{V}_n(\omega)\boldsymbol{V}_n^{\mathrm{H}}(\omega)\boldsymbol{a}(\theta,\omega)} \tag{3.38}$$

The prior knowledge of the number of sources effectively allows precise minimisation of the noise components of the data, resulting in a significant increase in the detection

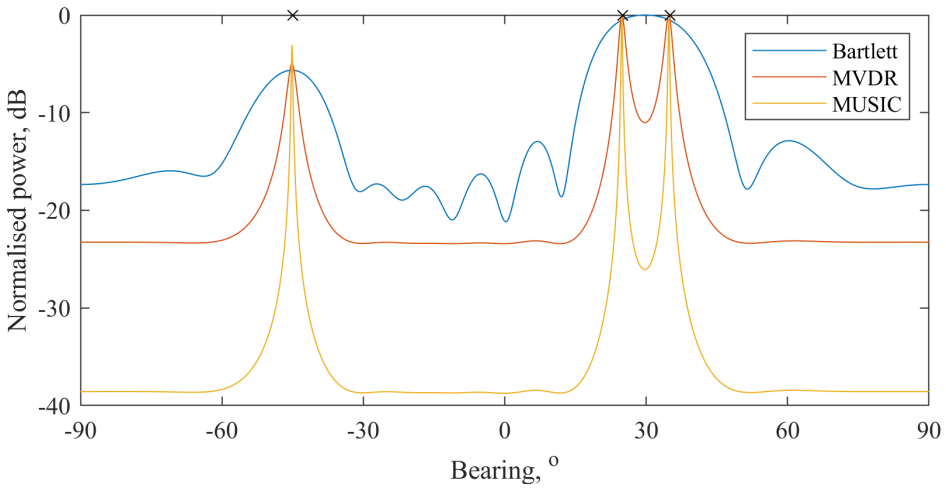

Figure 3-8: Comparison of the conventional beamformer, the MVDR beamformer and the MUSIC algorithm with three sources at various bearings(denoted by the "x"s) for a 10 sensor ULA with spacing $\lambda/2$ and an SNR of 20dB

capabilities of this algorithm, as shown in Figure 3-8, where the peaks are even more distinct than those of MVDR.

There are a number of extensions to the MUSIC algorithm, most notably the Root-MUSIC algorithm, which is a computationally more efficient polynomial-rooting version of the algorithm [72][73] and the Min-Norm algorithm, which is effectively a weighting applied to the MUSIC algorithm. This weighting resulted in an algorithm that exhibits lower bias and better resolution when applied to ULAs [74], however not so with arrays with arbitrary geometries [75].

Another subspace algorithm of note is the estimation of signal parameters via rotational invariance technique (ESPRIT) algorithm, which is distinct in that it does not require a search step, thereby making it computationally significantly faster and resulting in a single value for the DOA estimate rather than a spatial spectrum. However, it requires a specific type of array geometry, with the array split into sensor doublets in order to implement it [76][77].

One of the main drawbacks of using a subspace technique is the requirement to know the dimension of the signal subspace, which is to say the number of sources impinging on the array. For circumstances where this cannot be assumed beforehand, the problem of source enumeration has been approached a number of ways [78][79], often using information criterion or the eigenvalues of the covariance matrix [80][81].

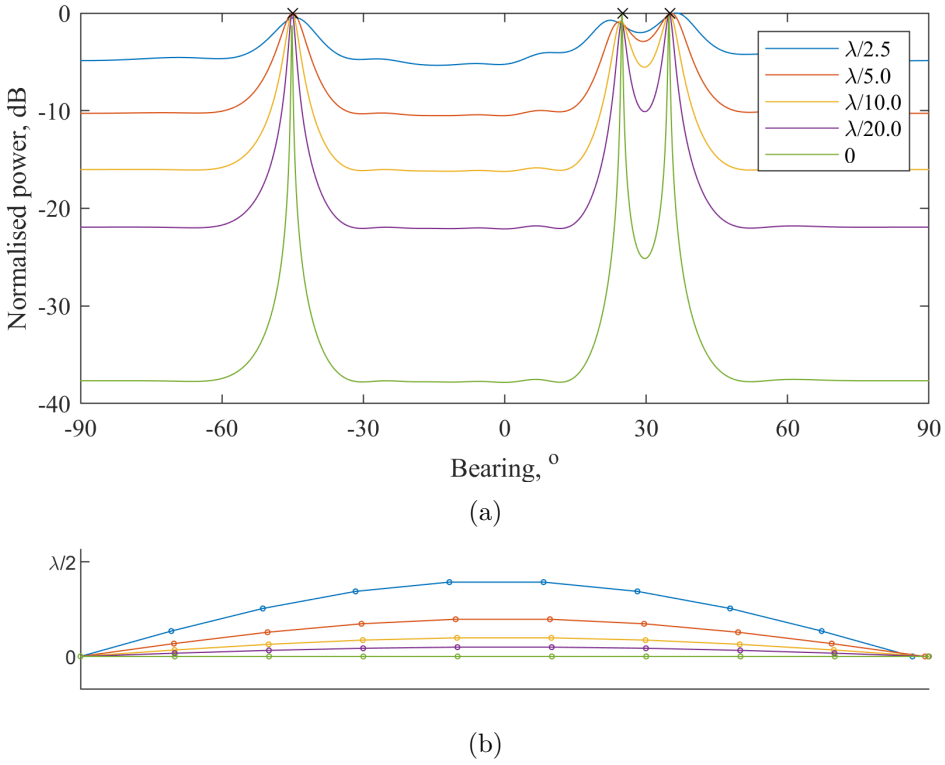

Figure 3-9: (a)MUSIC pseudo-spectrum assuming a straight array for a 10-sensor ULA with increasing levels of "bow" amplitude in the array. The 'x's indicate the true bearing to the source. (b) The corresponding bow amplitudes.

3.1.6 Effects of Inaccuracies

To fully access the benefits of the high resolution DOA algorithms requires highly accurate sensor position information. Figure 3-9a shows the effect of a perturbed, bow-shaped array on the MUSIC pseudo-spectrum assuming a straight array when formulating the steering vector. The amplitude of the bow-shape being just a fraction of the wave-length, $\lambda/20$, results in a significant reduction in the gain of the detection peak. At even higher levels of perturbation, the detections start to deviate slightly from the true bearings.

A common rule of thumb is that sensor positions need to be known to within $\lambda/10$ to ensure a loss of less than 1dB in array gain for conventional beamforming [82]. As can be seen from Figure 3-10, for an array with a bow-shape of amplitude $\lambda/10$ the advantage of increased gain with MVDR and MUSIC is mostly lost, although the resolution improvement remains. Also notable is the loss of the large performance difference between MVDR and MUSIC, present in Figure 3-8, with their resolution

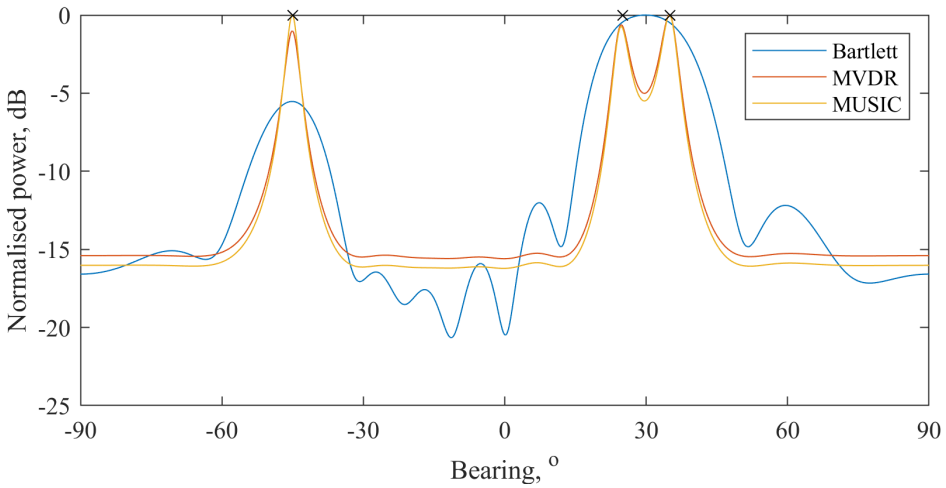

Figure 3-10: Comparison of DOA algorithm spectrums assuming a straight array for a 10-sensor ULA with a $\lambda/10$ bow in it

and gain being mostly equivalent.

3.2 Array Shape Estimation

The steering vector is core to successful implementation of the DOA algorithms. Inaccurate steering vectors can result in degraded performance with reduced array gain, bearing errors and spurious detection peaks [83][84]. This therefore requires precise knowledge of the location of each of the sensors in the array.

3.2.1 Array Models

For ULAs, there are a number of often used array models assumed in array shape estimation methods. These vary by the number of parameters they use to describe the array shape. The most basic involves simplifying the array to a bow shape [85][86][87], as in Figure 3-11, parametrised with α as the bow parameter and β as the angle at a specific position on the array. This allows the array shape to be defined with two dimensions in 2D space and 4 dimensions in 3D space (azimuth, elevation and bow parameter in horizontal and vertical plane). This is often useful for use with an array being perturbed by a manoeuvring vessel as the array will often follow the path of the vessel. Extending this concept further is the use of spline interpolation or curve fitting [88][89] to approximate the array shape. This offers slightly more flexibility in terms of the array shapes it can define, but is still limited by the order of the polynomial used.

Another model is known as a piecewise linear model [90][91][92][93][94], where

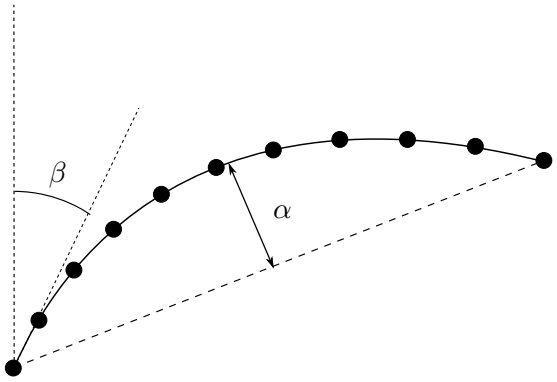

Figure 3-11: Bow-shape parametrised array model

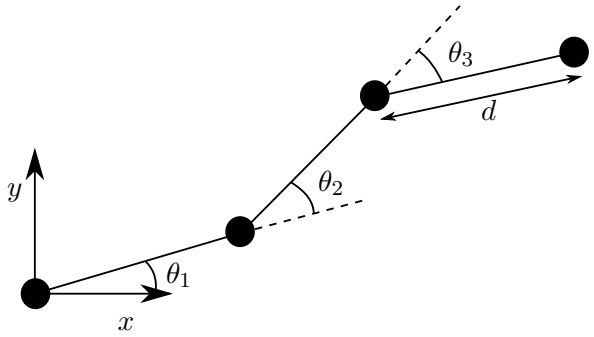

Figure 3-12: Piecewise linear array model

the array is composed of sensors with linear joints, as in Figure 3-12. With a fixed inter-sensor distance, d, this allows an K hydrophone array to be defined by $K-1$ parameters$\{\theta_1, \theta_2, \ldots, \theta_{K-1}\}$, in 2D space and $2(K-1)$ in 3D space. This parametrisation is useful for allowing unusual shapes.

Array shape estimation algorithms can be broadly split into techniques that use: non-acoustic data, such as heading sensors and depth sensors; acoustic data, either from opportunistic sources or from calibration sources placed in the water; or a combination of the two.

3.2.2 Non-Acoustic Methods

One of the earliest examples of spatial sensor-based estimation [95] provides a mathematical basis for the estimation of the shape of an array from heading and depth sensors placed along it. There are various examples of methods estimating the shape as an interpolated spline in experiments and simulation [96][89], as well as combining heading sensor data with a Kalman filter to improve the robustness to sensor failure [97]. As would be expected, however, all of these methods require a well-instrumented array to

be effective.

A further improvement was made introducing the water-pulley model [98], derived from the Paidoussis equation [99], given in Equation 3.39 [100]. This partial differential equation describes a flexible cylindrical body of circular cross-section with an incompressible fluid flowing around it at a uniform velocity and takes into account inertial forces, bending stiffness, drag and tow speed.

$$\begin{aligned} &\overbrace{m\frac{\partial^2 y}{\partial t^2}}^{\text{Cylinder inertial force}} + \overbrace{M\left[\frac{\partial}{\partial t}+U\frac{\partial}{\partial x}\right]^2 y}^{\text{Fluid mass inertial force}} + \overbrace{EI\frac{\partial^4 y}{\partial x^4}}^{\text{Bending stiffness}} \\ &+ \overbrace{\frac{\partial}{\partial x}\left[\left[\frac{1}{2}c_t\left[\frac{L-x}{d}\right]+\frac{1}{2}c_t'\right]MU^2\frac{\partial y}{\partial x}\right]}^{\text{Tension stiffness due to longitudinal drag}} \\ &+ \overbrace{\frac{1}{2\pi}c_n\frac{MU}{d}\left[\frac{\partial y}{\partial t}+U\frac{\partial y}{\partial x}\right]}^{\text{Damping term due to transverse drag}} = 0 \end{aligned} \tag{3.39}$$

where m is the cylinder linear mass, M is the fluid linear mass, d is the cylinder diameter, E is the cylinder elastic modulus, I is the cylinder moment of inertia, c_t is the tangential drag coefficient and c_n is the normal drag coefficient, U is the flow velocity in the x direction, L is the cable length, and (x, y) are the spatial coordinates of the cable.

Assuming a flexible array with a free end and whose length is far greater than its diameter, the small-diameter Paidoussis equation is derived,

$$c_t(\xi-1)\frac{\partial^2\eta}{\partial\xi^2}+c_n\left(\frac{\partial\eta}{\partial\tau}+\frac{\partial\eta}{\partial\xi}\right)=0 \tag{3.40}$$

In practice, the ratio $c_t/c_n \approx 0$ which then results in the simplified water-pulley model,

$$\frac{\partial\eta}{\partial\tau}+\frac{\partial\eta}{\partial\xi}=0 \tag{3.41}$$

where $\tau = tU/L$, $\eta = y(t,x)/L$ and $\xi = x/L$. This describes that the effects of the motion of the tow vessel propagate down the array undamped at close to the tow speed [101]. It has been demonstrated in simulation combined with depth sensors and compasses using a Kalman filter [91] and various methods have also incorporated the tow vessel GPS co-ordinates into the estimation, using the water-pulley model to estimate the resulting dynamics of the array [101][85].

Aside from the traditional use of auxiliary compasses and pressure sensors, it has also been demonstrated that the hydrostatic pressure at a hydrophone can be measured

using optical fibre hydrophones, which can then be interpolated to estimate array shapes in the vertical plane [102].

3.2.3 Acoustic Data-Driven Methods

Another style of array shape estimation involves the use of the acoustic data gathered on the hydrophones. This reduces the need for extra compasses or depth sensors as it uses data that would always be gathered in circumstances where knowledge of the sensor positions is advantageous.

3.2.3.1 Iterative Approaches

The first type of acoustic data-driven methods is the iterative method.

One style of iterative method involves maximising some cost function related to the array sensor positions to get a maximum likelihood estimate. This cost function has been implemented as a beamformer power output [103], or a spatial spectrum peak sharpness with conventional beamforming [104] and MVDR [105]. Some methods use sources in unknown locations [106][107], although these often require knowledge of one of the sensor's positions and the direction to another sensor in order to operate. The use of calibration sources in known locations gets around this requirement [108][109] but is often more practical for a one-off sensor position estimates.

Another iterative method in the literature is somewhat different and based on the assumption of a nominally straight array [110]. The time delay measurement from underwater lightbulb explosions in approximately known positions is estimated, and an iterative linearised inversion method is used to find the simplest array shape consistent with the data (i.e. with the least curvature). The optimal configuration of the calibrating sources has also been considered [82], looking at the effects of parameter errors, measurement errors, source positions and number of sources. This sensitivity study is formulated for the general cases of static seabed mounted horizontal line arrays (HLAs) and dynamic vertical line array (VLA), and is predominantly focused on the optimal design of an array sensor localisation system.

For continual estimation, a source or multiple sources can be constantly pinging in known locations as in [111], which utilises two sparker sources and a tail sensor on each array to estimate the shape of a number of streamers being towed behind an AUV. This also shows an investigation into different configurations of available data, finding that using both sources and the tail sensors significantly outperforms alternatives, as would be expected. Near-field calibrating sources and their multipath arrivals have also been used [112] with a maximum likelihood estimator that works well at high SNR and in

the presence of multipath, approaching the Cramer Rao lower bound (CRLB).

A distinctly different iterative approach is known as subspace fitting. This is more similarly related to the subspace beamforming algorithms, utilising the same concept of array model as detailed in Section 3.1.5. Again similarly, these are based on splitting the sample covariance matrix into subspaces and fitting the signal subspace [113][114] or utilising both subspaces [93]. This method has also been generalised for use with non-plane waves in the near-field [115], approaching the CRLB for high SNR. It also investigates the effect of the DOAs of the references sources, finding that they need to be separated by at least 15^o and ideally at broadside to the array.

3.2.3.2 Direct Inversion Methods

The more computationally efficient style of estimation is to perform a direct inversion. This requires taking some measurement of either inter-sensor phase difference or time delay and then using it to compute an estimate of the hydrophones' relative positions.

The eigendecomposition of the CSM (introduced in Section 3.1.3) can be used to provide estimates of the inter-sensor phase differences, as introduced in [116], which provides a generalised basis for the use of eigenvectors in three distinct cases of propagation, with and without multipath. This often used technique [117][118] is referred to as the eigenvector method and uses the eigenvector corresponding to the maximum eigenvalue as an estimate of the complex components of an impinging signal. This can then be used to compute the angle of the complex value as an estimate of the phase,

$$\hat{\boldsymbol{\phi}} = \arg(\boldsymbol{v}_1) \tag{3.42}$$

where $\hat{\boldsymbol{\phi}}$ is the set of phase estimates for each hydrophone's data and $\boldsymbol{v}_1$ is the $K \times 1$ column eigenvector corresponding to the maximum eigenvalue of $\hat{\boldsymbol{R}}$. This maximum-likelihood estimate can then be used to compute the relative locations of each hydrophone assuming a piecewise linear model:

$$x_k = \sum_{i=2}^{k} \hat{l}_{i-1,i} \cos\theta + \sum_{i=2}^{k} (d^2 - \hat{l}_{i-1,i}^2)^{1/2} \sin\theta \tag{3.43}$$

$$y_k = \sum_{i=2}^{k} \hat{l}_{i-1,i} \sin\theta + \sum_{i=2}^{k} (d^2 - \hat{l}_{i-1,i}^2)^{1/2} \cos\theta \tag{3.44}$$

where $\hat{l}_{i-1,i} = (\lambda/2\pi)\hat{\phi}_{i-1,i}$, d is the inter-sensor distance and θ is the impingement angle of the incoming wave. It has been shown to have a lower RMS error than the iterative beamformer output sharpness method detailed above [90]. This method has

also been extended to decrease the computational cost of the eigendecomposition with long arrays [92]. Using the knowledge that the estimation bias and variance is not significantly affected by the number of sensors, the array can be partitioned and each subarray processed instead. A more recent implementation of the eigenvector technique is demonstrated in [94] with single and double near-field calibrating sources. In this case, the top two eigenvectors are used as estimates for the phase differences from two spatially separated impinging sound sources. This requires sources to be spectrally or temporally disjoint to ensure a non-singular covariance matrix.

Another method similar to the eigenvector technique is presented in [119], using a Hidden Markov model to introduce temporal continuity to the estimates. This incorporates statistical likelihood when considering the acoustic estimates used to infer the array shape, which is modelled as piecewise linear. It is shown in simulation to outperform maximum likelihood methods at low SNR.

Experimentally there have also been examples of opportunistic sources used for array shape estimation, using cross-correlations of ship noise [120] and time-averaged ambient ocean noise [121].

3.2.3.3 Data Fusion

Some of the limitations of the above methods can be alleviated using a combination of techniques. This can be achieved by using the acoustic estimates when available and combining with compasses and depth sensors based on the statistical likelihood of their accuracy. One such example uses ambient noise field directionality mapping fused with heading sensor data to estimate an bow-shaped array travelling through a turn [86]. Unlike previous methods, it uses a stochastic noise field model that captures discrete and distributed noise sources as opposed to a deterministic system model.

3.2.4 Summary

The array shape estimation algorithms presented here each make their own assumptions in order to solve the problem with the available data. However, many of these assumptions do not necessarily hold true for a wave-propelled vessel.

Bow-shape Parametrising the array as a bow shape may be too simplistic for the potentially chaotic shape induced by the wave-propulsion.

Vessel motion extrapolation Due to the unpredictable and relatively slow nature of the vessel motion, methods using the water-pulley model may not be applicable.

Assumption of horizontal array The often reasonable assumption that the array is oriented in the horizontal plane, which is often used to simplify estimation, may not be appropriate and the array may need to be estimated in 3D space.

A new method may be required, aiming to tackle these extra challenges and building upon the techniques discussed here.

Chapter 4

Simulation Model

To aid the development of processing algorithms and assess the performance capabilities of system configurations, a modelling and simulation process was developed for application to an array deployed behind a wave-propelled USV. This is introduced here as it will be used throughout the thesis for illustrative purposed but a detailed validation exercise is included in Section 6.3.

4.1 Overview

The aim is to simulate the data received on hydrophones with an array of arbitrary, dynamic shape, receiving the acoustic emissions of single or multiple moving sources in the presence of additive noise.

The process, as described in Figure 4-1, involves cycling through each acoustic source and generating their signal using the specified frequency content and power. The displacement between the source and each hydrophone for each time step is used to compute the time delays and transmission losses, which can then generate the delayed and scaled time series for each hydrophone. The noiseless data is produced as a summation of each of these signals. The final step is to add noise to each hydrophone's data series.

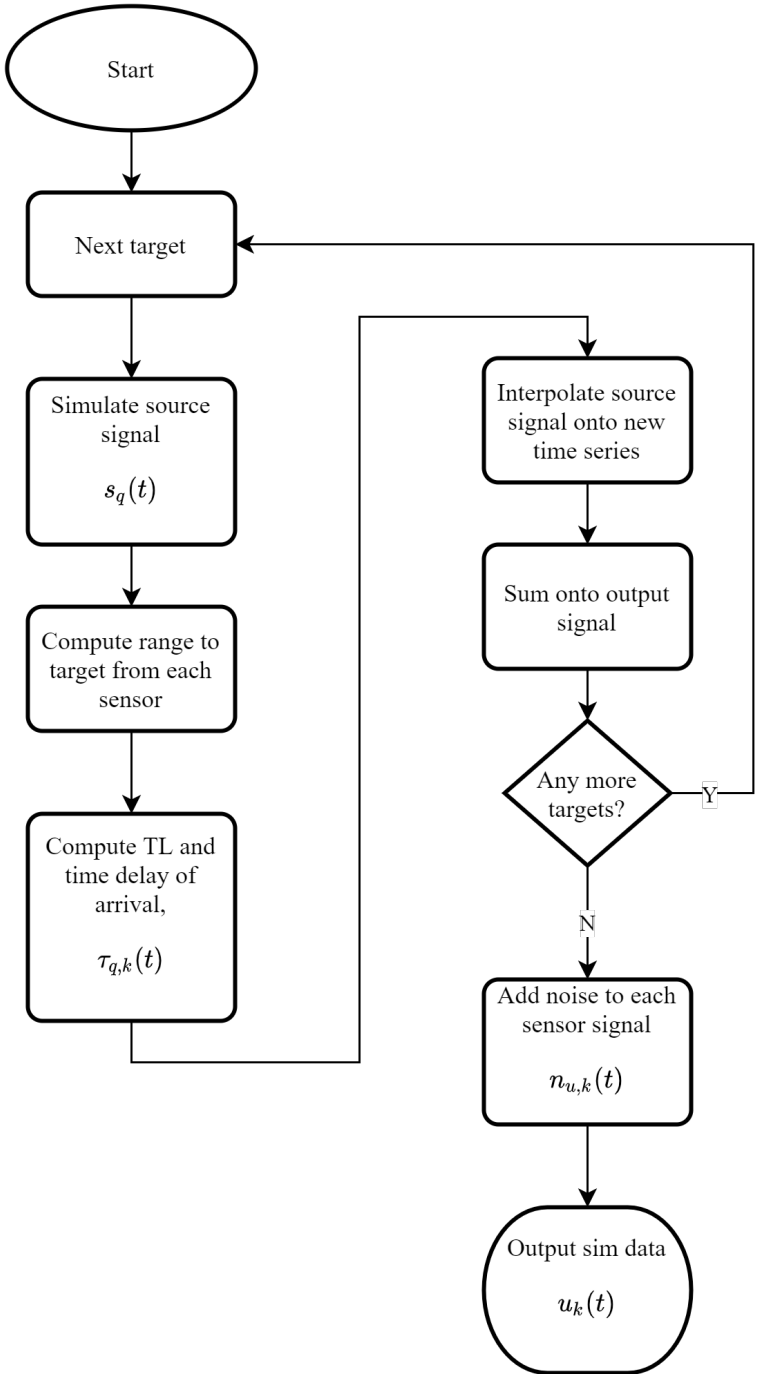

Figure 4-1: Flow diagram of the simulation process

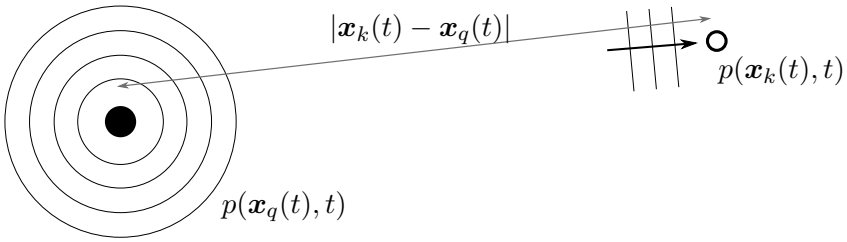

Figure 4-2: Illustration of a sensor and a source in 2D in the vertical plane

4.2 Acoustic Data Modelling

4.2.1 Source Signal

A source with index q is modelled as an omnidirectional point projector with position, $\boldsymbol{x}_q$, which can vary with time, t.

$$\boldsymbol{x}_q(t) = [x_q(t), y_q(t), z_q(t)]^{\mathrm{T}} \tag{4.1}$$

The wavefield at this position can be described as

$$p\left(\boldsymbol{x}_q(t), t\right) = A_q(t) s_q(t) \tag{4.2}$$

where s_q is the time varying function describing the source signal and A_q is the magnitude in Pa converted from the SL, i.e. $A_q = 10\exp(\mathrm{SL_q}/20)$. For example, a tonal source signal could be modelled as $s(t) = \sin(\omega t + \varphi)$, where ω is the angular frequency and φ is some arbitrary starting phase.

4.2.2 Propagation

4.2.2.1 Linear Ray Model

Considering a single arrival of a wave from a source at $\boldsymbol{x}_q$ to a single hydrophone positioned at $\boldsymbol{x}_k$, the wavefield at this hydrophone would then be described as

$$p_q\left(\boldsymbol{x}_k(t), t\right) = A_{q,k}(t) s_q\left(t - \tau_{q,k}(t)\right) \tag{4.3}$$

where $\tau_{q,k}(t)$ is the temporal delay and $A_{q,k}(t)$ is the reduced amplitude from propagation losses. For the simplest case of a straight direct path, the delay can be computed by calculating the 3D Euclidian distance between the source and the hydrophone, and dividing by the propagation speed,

$$\tau_{q,k}(t) = \frac{|\boldsymbol{x}_k(t) - \boldsymbol{x}_q(t)|}{c} \tag{4.4}$$

with c as the propagation speed in $\mathrm{m\,s^{-1}}$. The adjusted amplitude can be calculated using Equation 4.5, where TL is estimated using the range and the equation for transmission loss with spherical propagation from Section 2.3.1.

$$A_{q,k}(t) = 10^{((\mathrm{SL}_q(t) - \mathrm{TL}_{q,k}(t))/20)} \tag{4.5}$$

Extended to Q acoustic sources this results in a summation of temporally-varying delayed signals,

$$p(\boldsymbol{x}_k(t), t) = \sum_{q=0}^{Q-1} A_{q,k}(t) s_q\left(t - \tau_{q,k}(t)\right) \tag{4.6}$$

4.2.2.2 Bellhop

For a more physically accurate representation, the Bellhop raytracing algorithm, described in Section 2.3.4, can be used to compute the time delays and transmissions losses for each source. This uses knowledge of the water column depth, sound speed profile and seabed properties to model the path from source to receiver, including any reflected paths. These can then be considered as individual arrivals, including as many orders of propagation as necessary. The example in Figure 4-3 shows the paths computed using Bellhop considering 4 orders of multipath with a uniform sound speed profile. The implementation used comes from the Ocean Acoustics Library [122].

Including the extra arrivals estimated by the Bellhop model into Equation 4.6 results in

$$p(\boldsymbol{x}_k(t), t) = \sum_{q=0}^{Q-1} \sum_{m=0}^{M-1} A_{q,k,m}(t) s_q\left(t - \tau_{q,k,m}(t)\right) \tag{4.7}$$

where $A_{q,k,m}$ and $\tau_{q,k,m}$ are the adjusted magnitude in Pa and time delays in seconds respectively, for the m^{th} multipath between the sensor at $\boldsymbol{x}_k$ and the source at $\boldsymbol{x}_q$.

4.2.3 Surface Reflections

Reflections from an oscillating sea surface have been considered as an additional temporally varying time delay on surface reflected paths resulting in an adjusted time delay,

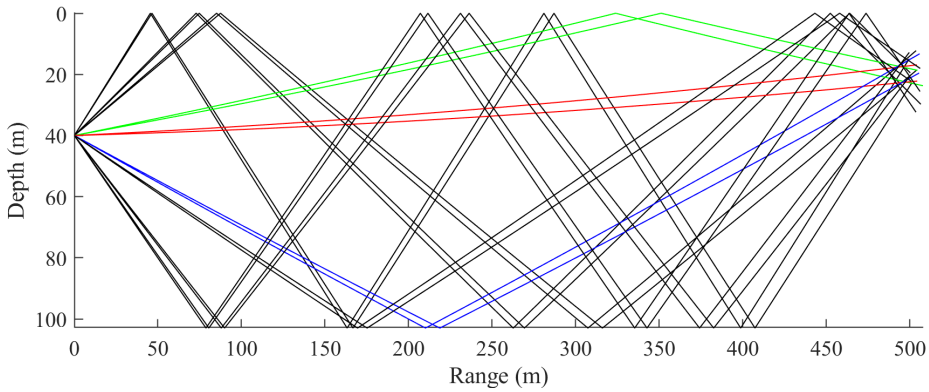

Figure 4-3: Example of the different paths that travel from a source at a depth of 40m to a receiver at a depth of 25m and a range of 500m, generated using the BELLHOP model

$$\tilde{\tau}_{q,k,m}(t) = \tau_{q,k,m}(t) + A_r \sin 2\pi f_r t \tag{4.8}$$

where A_r and f_r is the amplitude in metres and frequency in Hz of the time delay deviation caused by the surface motion. While not necessarily a physically accurate model of the sea surface, this can emulate the effect of a reflective but slowly varying sea surface, capturing the decrease in coherence between surface-reflected and non-surface-reflected arrivals. The parameters can be approximated using knowledge of the wave peak period and wave height.

4.2.4 Doppler Shift

The Doppler shift associated with moving sources is implicitly captured through the method of delaying signals in the time domain. The delay and scaling is applied to each step of the time series of the source's signal which is then interpolated back onto the regularly sampled time step, as illustrated in Figure 4-4.

4.2.5 Noise

The final step to go from the acoustic wavefield to the final simulated data is to add noise:

$$u_k(t) = p(\boldsymbol{x}_k(t), t) + n_{u,k}(t) \tag{4.9}$$

where

$$n_{u,k}(t) \sim \mathcal{N}\left(0, \sigma_u^2\right)$$

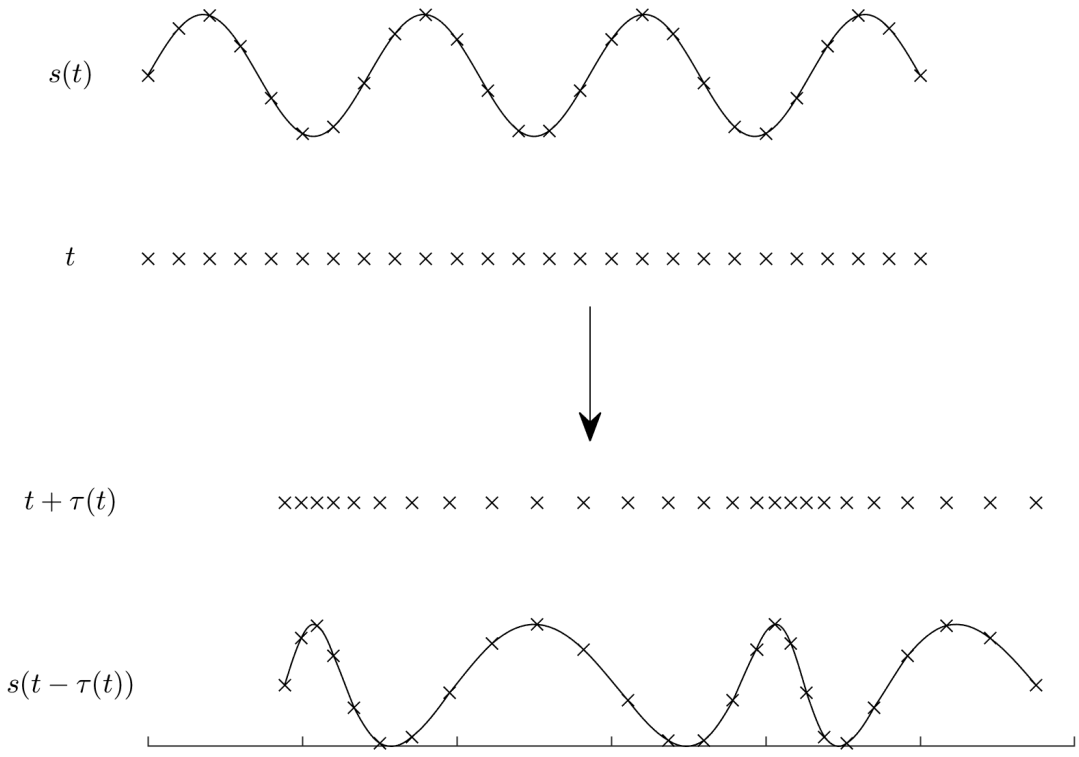

Figure 4-4: Illustration of the time varying delay interpolation for capturing Doppler shift

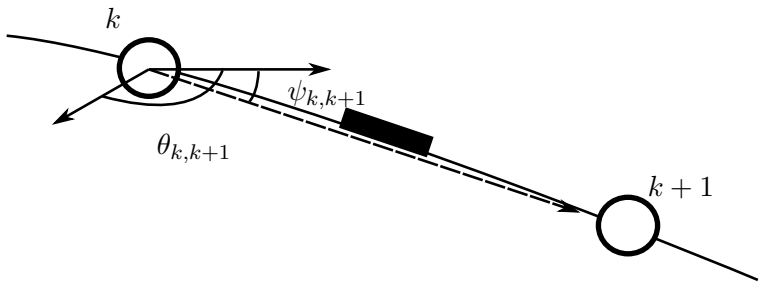

Figure 4-5: Compass simulation with compass between two hydrophones. Compass indicated by the black rectangle.

and σ_u^2 is the variance of the noise. Noise is typically modelled as spatially white additive Gaussian, defined by a noise level, NL, in dB. This is converted to variance as $\sigma_u^2 = 10^{\mathrm{NL}/10}$. The noise can also be spectrally filtered in the frequency domain prior to summation to provide coloured noise, to give a more accurate representation of the noise spectral profile. This can be given as a noise PSD in dB/Hz, NL(f). Spatial and temporal whiteness of noise is a common assumption that is not necessarily correct, as there is typically some directionality and temporal variability in experimental situations, but this was not chosen to be explored in this iteration of the simulator.

4.3 Non-Acoustic Sensor Modelling

The other outputs of the model are the physical sensor measurements which are modelled as the true orientation/depth of the array at the sensor position in the presence of additive Gaussian noise.

4.3.1 3-axis Compass Measurements

Consider the c^{th} compass positioned between the k^{th} and the $(k+1)^{\mathrm{th}}$ hydrophone. The simulated reading in degrees for heading, θ, and tilt, ψ, for a 3-axis compass positioned here is modelled as the direction from the k^{th} hydrophone to the next adjacent hydrophone in the presence of additive noise, $n_{\theta,k}$ and $n_{\psi,k}$,

$$\theta_c(t) = \tan^{-1}\left(\frac{y_{k+1}(t) - y_k(t)}{x_{k+1}(t) - x_k(t)}\right) + n_\theta(t) \tag{4.10}$$

$$\psi_c(t) = \tan^{-1}\left(\frac{\sqrt{(x_{k+1}(t) - x_k(t))^2 + (y_{k+1}(t) - y_k(t))^2}}{(z_{k+1}(t) - z_k(t))}\right) + n_\psi(t) \tag{4.11}$$

where

$$n_\theta(t) \sim \mathcal{N}\left(0, \sigma_\theta^2\right)$$

and

$$n_\psi(t) \sim \mathcal{N}\left(0, \sigma_\psi^2\right)$$

The noise is defined by the compass sensor variance in heading, σ_θ^2, and tilt, σ_ψ^2. For a compass co-located with the k^{th} hydrophone, the sensor output is modelled as the average of the directions to the adjacent hydrophones either side.

4.3.2 Pressure Measurements

Similarly to the compass reading, the reading from a pressure sensor positioned at the k^{th} hydrophone is simulated using the precise array z position at the sensor location converted to bar and in the presence of noise, $n_{h,k}$.

$$h_c(t) = 0.1 z_k(t) + n_{h,c}(t) \tag{4.12}$$

where

$$n_{h,c}(t) \sim \mathcal{N}\left(0, \sigma_h^2\right)$$

and σ_h^2 is the pressure sensor variance in bar.

4.4 Simulated Acoustic Results

Two simulated datasets were generated for use in the subsequent chapter for the development of the estimation algorithm and demonstration of the model. These were generated to have an idealised resemblance to the experimental data which is discussed in Chapter 6. To that end, the level of perturbation is roughly comparable, as well as the range to the source, the configuration of the array and the frequencies of the emitted signal. The first dataset utilises the linear ray propagation model and the second uses the Bellhop model with more complicated multipath propagation.

4.4.1 Simulation Parameters

4.4.1.1 Array

In the simulation an 8-hydrophone array with an inter-hydrophone spacing of 0.23m is used, which is dynamically perturbed, as shown in Figure 4-6 and Figure 4-7. These plots represent the variation with time of the array in the xy and xz planes as a surface. This motion is generated using a sinusoidally varying level of perturbation, between

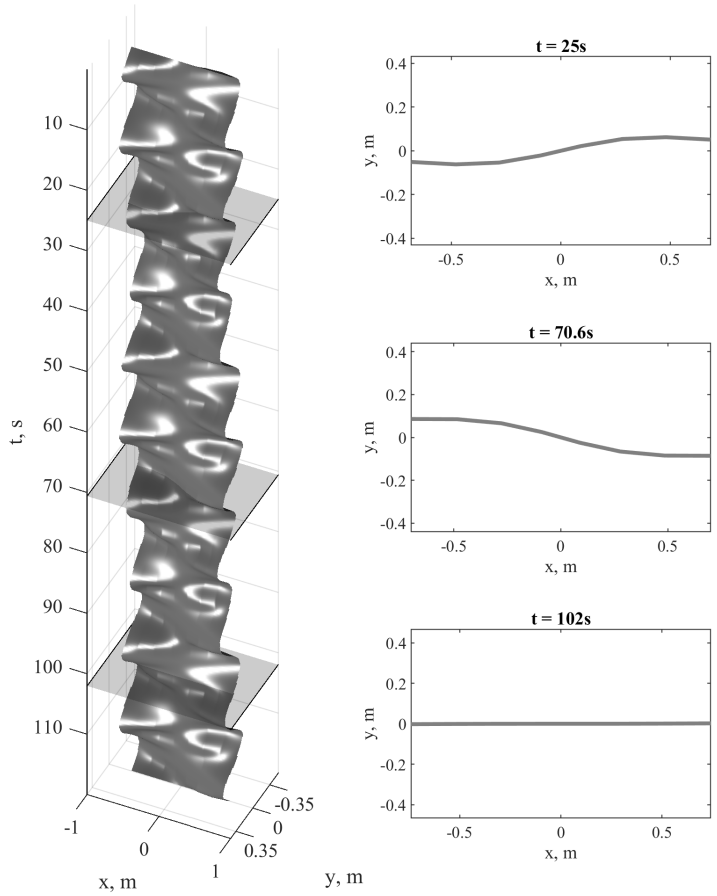

Figure 4-6: Variation in time of the x and y positions of the array for the simulation datasets

straight and a single cycle of a sinusoid with a peak-to-peak distance of 0.1m ("s" shaped). The heading, pitch and roll of the array are also varying sinusoidally with different frequencies to emulate a dynamically perturbed array. This array is placed at the origin in x and y, and with a tail depth of 10m.

4.4.1.2 Source

The simulation features a single moving source travelling from $\boldsymbol{x}_q = [-90, 40, -40]$m to $\boldsymbol{x}_q = [90, 40, -40]$m over the course of two minutes. The source is producing tonal signals at 370Hz, 790Hz, 1540Hz, 1640Hz and 1740Hz, each with a SL that increases from 110dB at $t = 0$s up to 139dB at $t = 120$s.

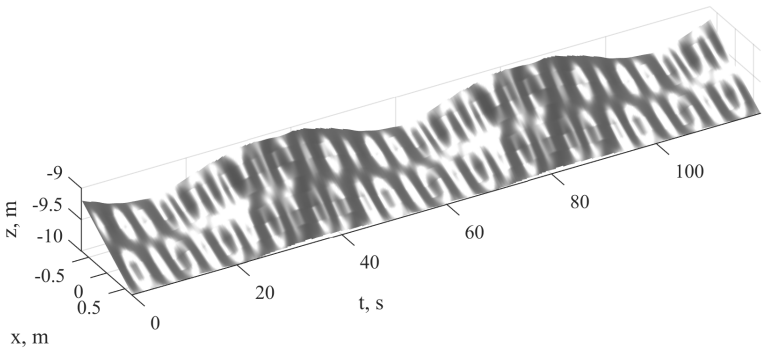

Figure 4-7: Variation in time of the x and z positions of the array for the simulation datasets

4.4.1.3 Noise

The noise is generated using filtered Gaussian noise with the spectral profile obtained from an averaged section of experimental data from the trial data set used in Section 6, shown in Figure 4-8.

4.4.2 Simulator Outputs

Figure 4-9 shows the simulated non-acoustic data for the heading, pitch and pressure for non-acoustic sensors positioned at the head end of the array, with $\sigma_c = 2^o$ and $\sigma_h = 0.05$m.

The spectrogram for the simulated acoustic data from each dataset can be seen in Figure 4-10, showing the increasing power of the source signals towards the end of the dataset. Also visible is the the interference pattern caused by the multipath propagation in the second dataset, Figure 4-10b, which is not present in the first, Figure 4-10a.

The beamformer output at a single frequency for the three beamforming algorithms introduced in Chapter 3 can be plotted as a waterfall plot as in Figure 4-11. This shows how the power estimate varies as a function of time and bearing. The difference in resolution is clearly visible between the methods, with a clear detection peak at all bearings in both Figure 4-11b and 4-11c but a much broader peak in Figure 4-11a. In Figures 4-11d, 4-11e and 4-11f there are two dominant peaks due to the multipath: one for the direct path and one for the surface reflected multipath. Again, these are more prominently visible with MVDR and MUSIC due to their increased bearing resolution.

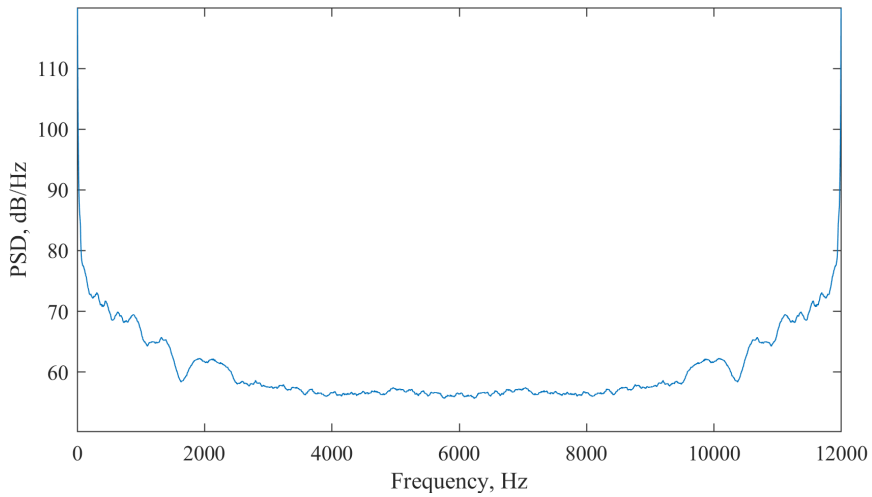

Figure 4-8: Noise PSD from experimental data

4.5 Summary

Presented in this chapter is a simulation process, capable of simulating the output of a hydrophone array in the presence of multiple moving sound sources. The array can be varied in shape, capturing the effects of Doppler shift and allowing investigation of perturbed arrays. The propagation model used can be selected as either a linear ray model, where only the direct path to the sensor is considered, or using the Bellhop propagation model, which can accurately capture more complicated paths between the sensors and the sound source. This takes into account the sound speed profile of the water column, as well as interaction with a reflective sea surface and sea floors, and the resulting multipath arrivals. The effect on these multipath arrivals of a non-stationary reflective sea surface is also modelled. Finally, the ambient noise is modelled as additive spatially white Gaussian which can be specified as a PSD to allow for spectrally varying noise power.

The simulated datasets used in the subsequent chapter for array shape estimation method validation are also introduced here, produced as an idealised dataset resembling the experimental dataset. Further results from this simulator will be presented in Chapter 6, with validation of its accuracy to experimental data.

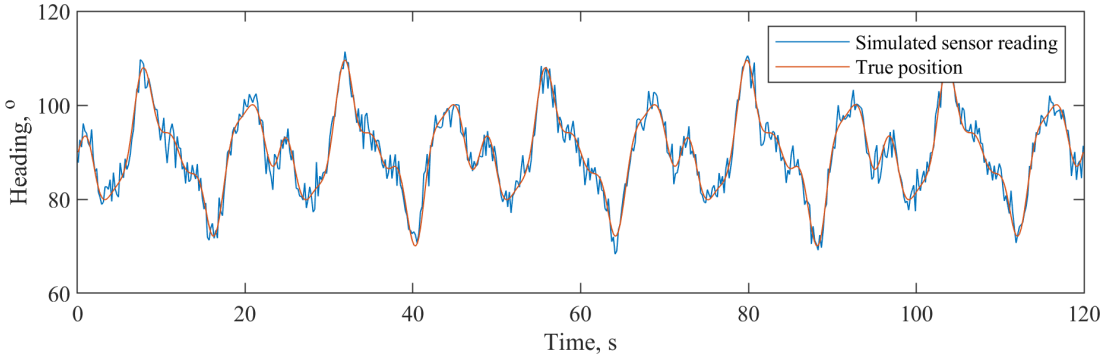

(a) Heading

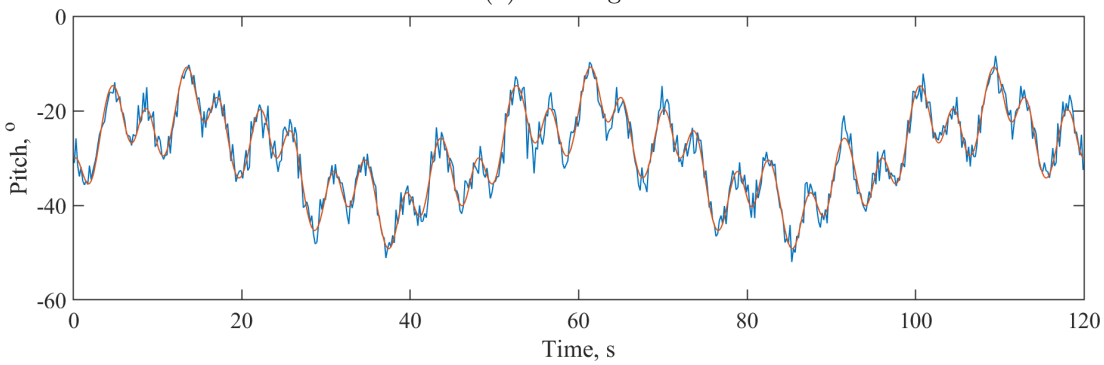

(b) Pitch

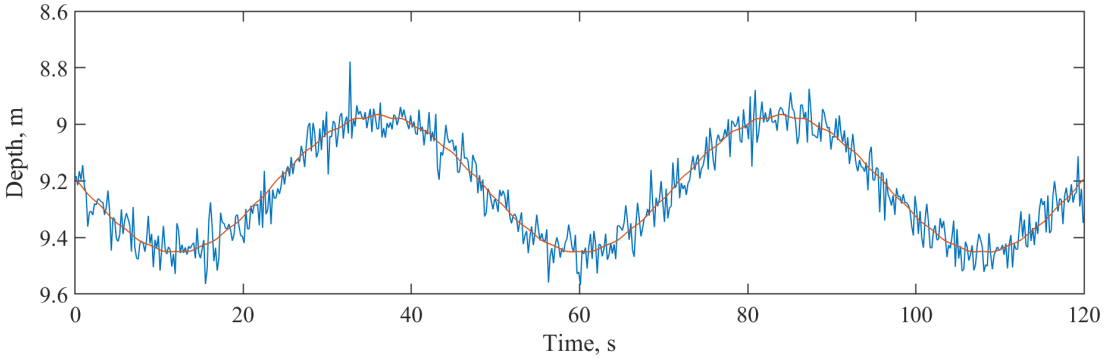

(c) Pressure

Figure 4-9: Simulated non-acoustic data for head-end compass and pressure sensors for simulation dataset

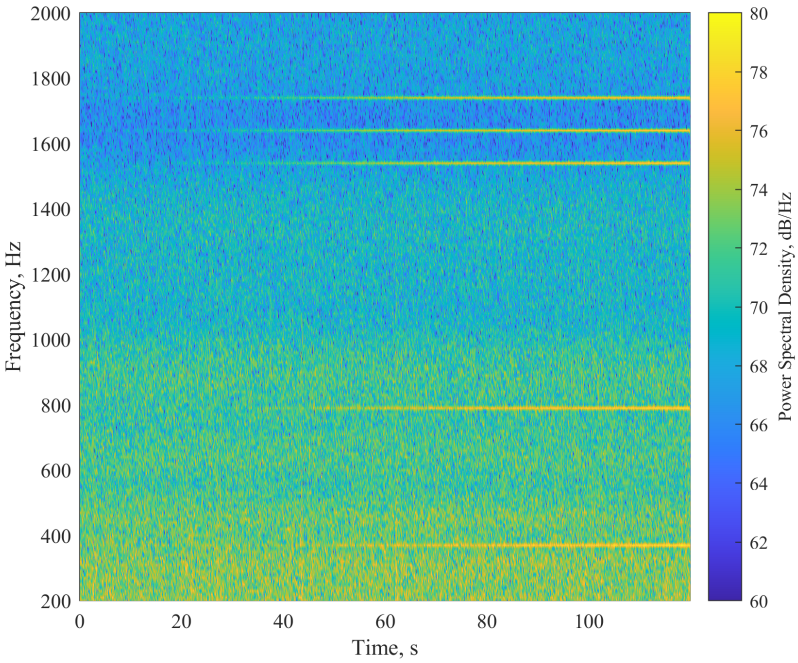

(a) Linear ray path model

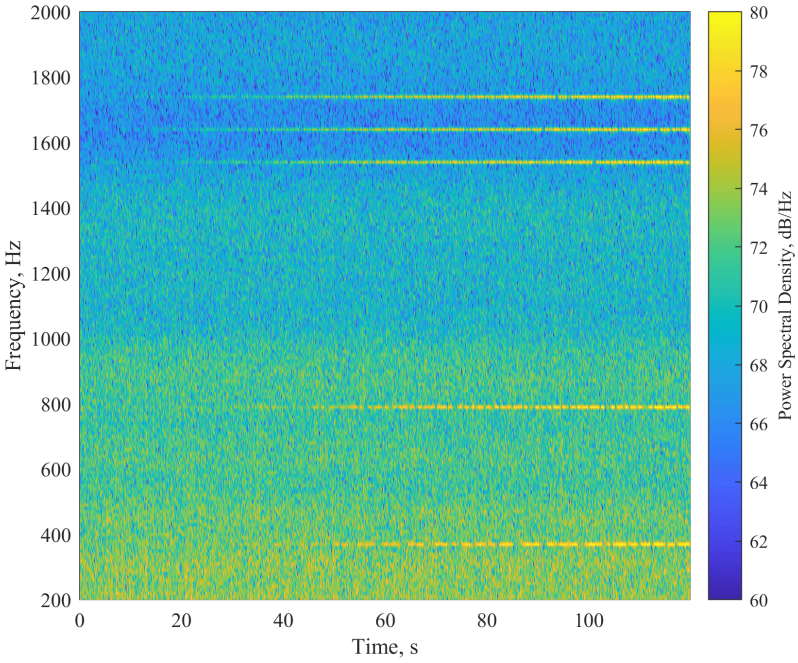

(b) Bellhop model

Figure 4-10: Spectrogram of simulated data

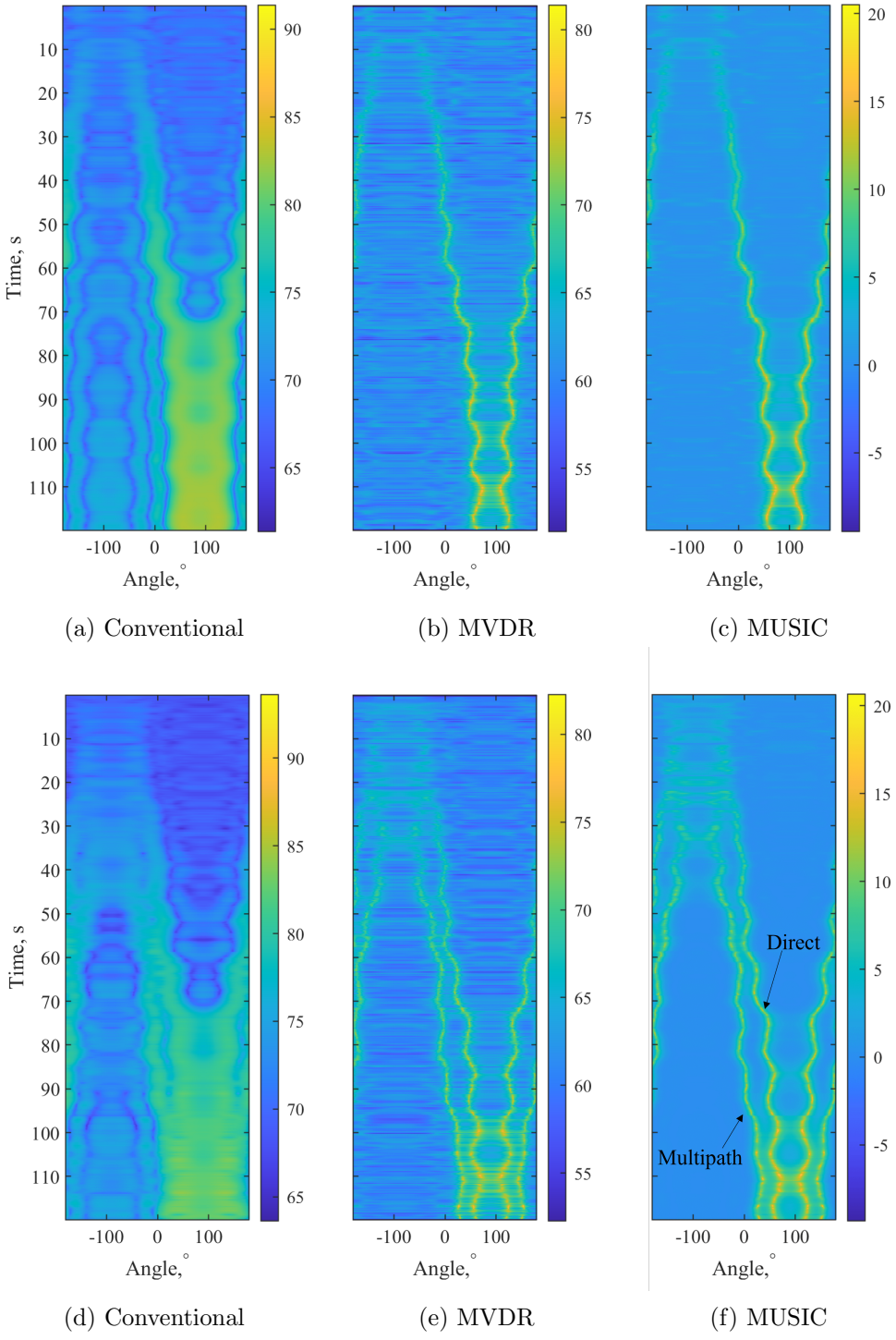

(a) Conventional (b) MVDR (c) MUSIC

(d) Conventional (e) MVDR (f) MUSIC

Figure 4-11: Beamformer results for the simulated data set at 1540Hz. (a-c) linear ray model, (d-f) Bellhop model with multipath. Each horizontal slice displays a time instance of beamformed data, with the color axis showing the estimated power in a different bearing from the array.

Chapter 5

Hierarchical Particle Filtering for Array Shape Estimation

Following on from the discussion of array shape estimation algorithms from Chapter 3, a method of estimating the shape of a towed array has been developed to address the challenges associated with deployment from a wave-propelled USV. The main points to address were to allow full freedom in the shape of the array, to estimate the array in 3 dimensions and to be able to operate with an unpredictable tow vessel.

5.1 Recursive Bayesian Estimation

A recursive Bayesian estimation technique was employed with a particle filtering representation, to combine all the available data sources. This allows incorporation of many different data types and provides an analysis tool for investigating the effectiveness of the configuration of the array's non-acoustic instrumentation for estimating its shape.

The algorithm assumes the state of the array can be modelled as a Markov process, i.e. that the state of the array at a given time instance depends only on the state at the previous time step [123]. The general principle of a particle filter is to approximate a multivariate probability density function (PDF) by maintaining a set of particles. Each of these particles represents a possible solution in a multi-dimensional space, where the state describes the position and velocity of certain points along the array. At each time step they are drawn from a proposal density, known as the prior distribution. Each particle has a corresponding importance weight which relates to its likelihood and is updated according to observations. These weights approximate the posterior probability distribution which is then used to provide the subsequent time step's proposal distribution and the process continues recursively for all subsequent

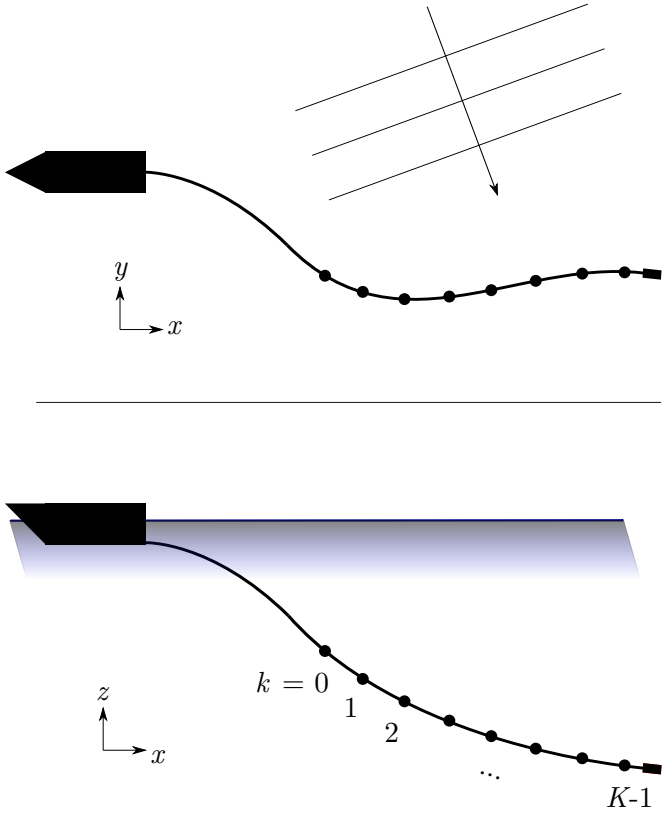

Figure 5-1: Array coordinate frame

time-steps. This process is known as sequential importance resampling. The benefit of such a method is that by discarding particles in positions with low likelihood you can efficiently approximate a non-linear probability distribution without having to densely sample the entire space.

The method detailed in this section was developed using [123][124] for reference and uses elements from each of the methods described in Section 3.2.

5.2 The Proposed Algorithm

5.2.1 Array State Model

The array has been represented as K nodes with the k^{th} node as in Figure 5-1. Acoustic data collected at hydrophones positioned on these nodes contains information on their relative positions and there are also L non-acoustic sensors which can provide measurements of depth, heading and tilt for that point in the array.

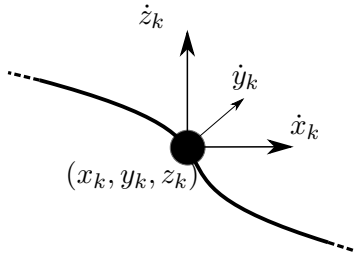

Figure 5-2: State vector for individual node

The state equation for an array with K nodes is:

$$\boldsymbol{z} = [\boldsymbol{x}_0, \boldsymbol{x}_1, \ldots, \boldsymbol{x}_{K-1}]^{\mathrm{T}} \tag{5.1}$$

where

$$\boldsymbol{x}_k = [x_k, y_k, z_k, \dot{x}_k, \dot{y}_k, \dot{z}_k]^{\mathrm{T}} \tag{5.2}$$

with $^{\mathrm{T}}$ denoting the transpose and $\dot{x}$ is the rate of change of x. This vector, $\boldsymbol{z}_k$, describes the positions and velocities at each node as in Figure 5-2.

5.2.1.1 Curse of Dimensionality

As a result of the proposed array state model, the dimensionality of the space to be searched increases as $K \times 6$. As the effectiveness of a particle filter is determined by the sampling density, this would result in a rapid decrease in efficiency with increasing array length [125]. The particles are distributed more sparsely, making it more likely that the importance weights will degenerate. Weight degeneracy is when only a few weights are significant and all others are close to zero, hence providing an inaccurate representation of the posterior distribution. This is commonly known as the "curse of dimensionality".

This effect has been investigated and there are various methods that have been used to attempt to alleviate the effects of it [125], one of which is the concept of partitioning the space into lower dimensional subspaces [126][127]. These subspaces are loosely coupled and can interact with each other but each of them has their own particle filter for approximating their distribution. In the context of array shape estimation this concept can be used to separate the various sources of data so that their likelihood functions are only considered at the point when they are most relevant. For example, a compass situated between two hydrophones does not explicitly constrain the array away from its location. This applies even more so to inter-hydrophone acoustic time delay measurements, which only give information of the relative positions between two

hydrophones. The state space can therefore be split into the array state space (herein referred to as the global space) and K inter-node relative spaces.

5.2.2 Procedure

The procedure will be described generally in this section, with extra detail on the likelihood functions and prior distributions provided in subsequent sections.

The algorithm maintains the set of particles which are defined in global space in Equation 5.3, where the subscript n denotes the time step and M the number of particles.

$$\boldsymbol{Z}_n = \left\{ \boldsymbol{z}_n^{(0)}, \boldsymbol{z}_n^{(1)}, \ldots, \boldsymbol{z}_n^{(M-1)} \right\} \tag{5.3}$$

with corresponding weights

$$\boldsymbol{W}_n = \left\{ W_n^{(0)}, W_n^{(1)}, \ldots, W_n^{(M-1)} \right\} \tag{5.4}$$

Each global space particle represents a possible state for the array, with its fit to the sensory data described by its weight.

The procedure, which is summarised in Figure 5-3, is as follows:

0. **Initialise the particle filter** The initial step is to populate the global space with M particles. The spatial coordinates of the state vector span an infinite space so it is necessary to draw from a more limited distribution in likely positions. For an array with a single compass, one such method of achieving this would be to draw the spatial coordinates from a limited space around points based on the initial pitch and heading measurements of the compass,

$$\begin{aligned} x_{k,0}^{(m)} &\sim \mathcal{U}\left(\hat{x}_k - \chi/2, \hat{x}_k + \chi/2\right) \\ y_{k,0}^{(m)} &\sim \mathcal{U}\left(\hat{y}_k - \chi/2, \hat{y}_k + \chi/2\right) \\ z_{k,0}^{(m)} &\sim \mathcal{U}\left(\hat{z}_k - \chi/2, \hat{z}_k + \chi/2\right) \\ \dot{x}_{k,0}^{(m)}, \dot{y}_{k,0}^{(m)}, \dot{z}_{k,0}^{(m)} &\sim \mathcal{U}(-v_{\max}, v_{\max}) \end{aligned} \tag{5.5}$$

where

$$\begin{aligned} \hat{x}_k &= r_k \cos(\psi)\cos(\theta) \\ \hat{y}_k &= r_k \cos(\psi)\sin(\theta) \\ \hat{z}_k &= r_k \sin(\psi) \end{aligned} \tag{5.6}$$

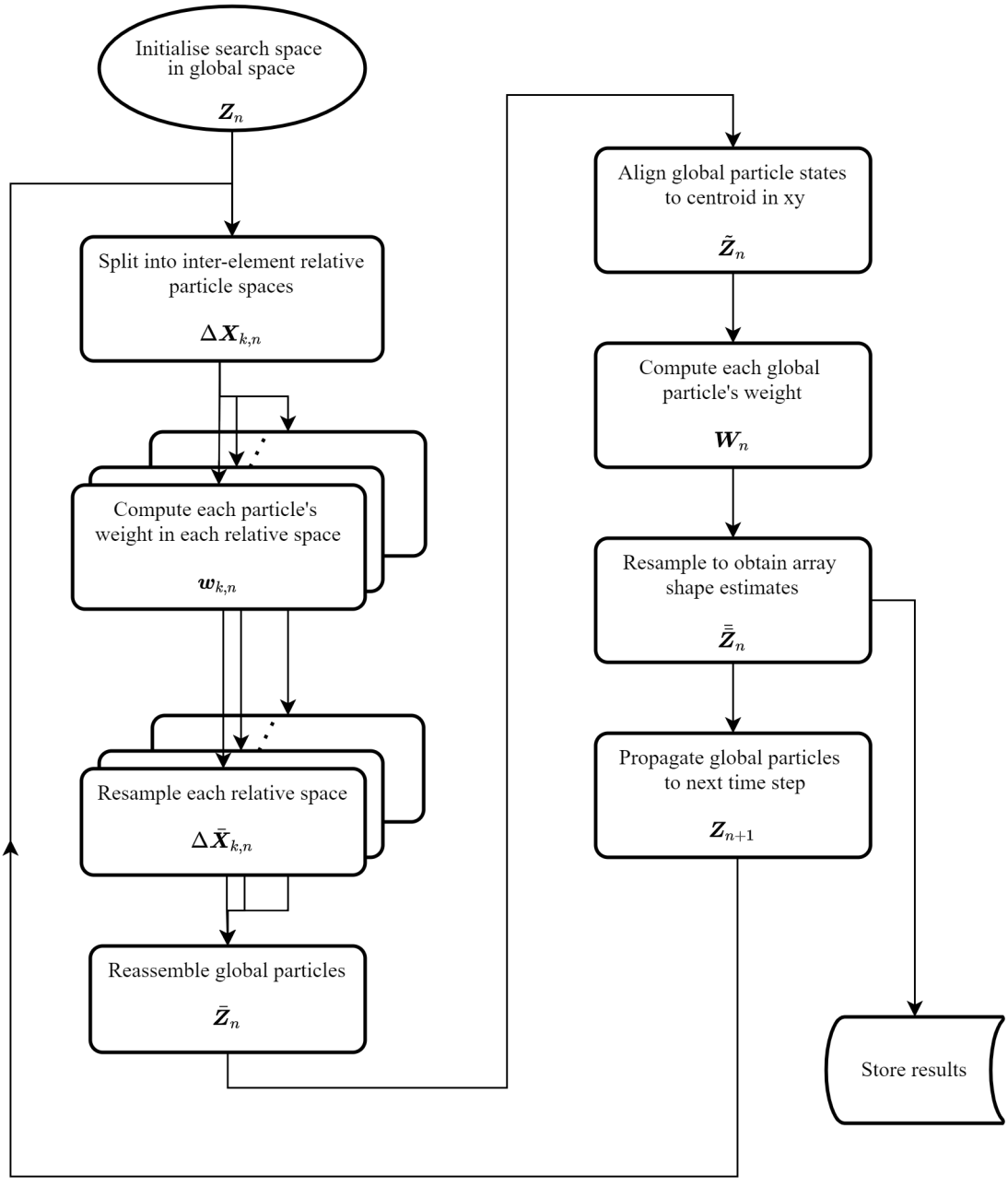

Figure 5-3: Flow diagram of the particle filtering procedure for array shape estimation

r_k is the length along the array of the kth node, ψ and θ are the compass pitch and heading respectively, and χ is the limit of the initial search space

1. **Split into relative spaces** The particles in global space are split into inter-node relative particle spaces, $\Delta \boldsymbol{X}_{k,n}$ by taking the difference between adjacent nodes as in Equation 5.7 for the kth node.

$$\Delta \boldsymbol{x}_{k,n}^{(m)} = \boldsymbol{x}_{k+1,n}^{(m)} - \boldsymbol{x}_{k,n}^{(m)} \tag{5.7}$$

$$\Delta \boldsymbol{x}_{k,n}^{(m)} = \begin{bmatrix} \Delta x_{k,n}^{(m)} \\ \Delta y_{k,n}^{(m)} \\ \Delta z_{k,n}^{(m)} \\ \Delta \dot{x}_{k,n}^{(m)} \\ \Delta \dot{y}_{k,n}^{(m)} \\ \Delta \dot{z}_{k,n}^{(m)} \end{bmatrix} \tag{5.8}$$

This results in $K-1$ sets of particles in inter-node relative space, where each particle represents a possible relative position. The set of particles for the kth adjacent pair of nodes is thus

$$\Delta \boldsymbol{X}_{k,n} = \left\{ \Delta \boldsymbol{x}_{k,n}^{(0)}, \Delta \boldsymbol{x}_{k,n}^{(1)}, \ldots, \Delta \boldsymbol{x}_{k,n}^{(M-1)} \right\} \tag{5.9}$$

with corresponding weights

$$\boldsymbol{w}_{k,n} = \left\{ w_{k,n}^{(0)}, w_{k,n}^{(1)}, \ldots, w_{k,n}^{(M-1)} \right\} \tag{5.10}$$

2. **Compute importance weights in relative spaces** For each particle compute the weight, $w_{k,n}^{(m)}$, in each relative space using the product of each likelihood function based on any sensor measurement with a relative inter-node measurement (acoustic phase delay measurements, ϕ_k, and the measurements from any co-located 3-axis compasses, $\theta_{k,n}$ and $\psi_{k,n}$) and the prior knowledge of the array spacing, d_k. If no compasses are present $\mathbb{P}\left(\theta_{k,n}, \psi_{k,n} \mid \Delta \boldsymbol{x}_{k,n}^{(m)}\right) = 1$.

$$\begin{aligned} w_{k,n}^{(m)} &= \mathbb{P}\left(\Delta \boldsymbol{x}_{k,n}^{(m)} \mid \boldsymbol{\phi}_{k,n}, \theta_{k,n}, \psi_{k,n}; d_k\right) \\ &= \mathbb{P}\left(\boldsymbol{\phi}_{k,n} \mid \Delta \boldsymbol{x}_{k,n}^{(m)}\right) \mathbb{P}\left(\theta_{k,n}, \psi_{k,n} \mid \Delta \boldsymbol{x}_{k,n}^{(m)}\right) \mathbb{P}\left(\Delta \boldsymbol{x}_{k,n}^{(m)}; d_k\right) \end{aligned} \tag{5.11}$$

3. **Relative space systematic resampling** Each relative space $\Delta \boldsymbol{X}_{k,n}$ is then

resampled with probabilities proportional to each of their weights, $\boldsymbol{w}_{k,n}$, to obtain equally weighted new particles, $\Delta\bar{\boldsymbol{X}}_{k,n}$ with corresponding weights $\bar{\boldsymbol{w}}_{k,n} = 1/M$. The resampling algorithm is described in Section 5.2.3.

4. **Reassemble into the global space** The relative space particles are sampled into global space by cumulatively summing each space to produce the elements of each new particle in global space, $\bar{\boldsymbol{z}}_n^{(m)}$.

$$\bar{\boldsymbol{z}}_n^{(m)} = \begin{bmatrix} \bar{\boldsymbol{z}}_{0,n}^{(m)} \\ \bar{\boldsymbol{z}}_{1,n}^{(m)} \\ \vdots \\ \bar{\boldsymbol{z}}_{K,n}^{(m)} \end{bmatrix} = \begin{bmatrix} \mathbf{0} + \Delta\bar{\boldsymbol{x}}_{0,n}^{(m)} \\ \sum_{k=0}^{1} \Delta\bar{\boldsymbol{x}}_{k,n}^{(m)} \\ \vdots \\ \sum_{k=0}^{K-1} \Delta\bar{\boldsymbol{x}}_{k,n}^{(m)} \end{bmatrix} \tag{5.12}$$

For convenience, the centroid of each global particle is then aligned to $[x, y] = [0, 0]$ as there is no tightly constraining information globally locating the array in horizontal space.

$$\widetilde{\boldsymbol{z}}_n^{(m)} = \bar{\boldsymbol{z}}_n^{(m)} - \frac{1}{K} \sum_{k=0}^{K-1} \bar{\boldsymbol{x}}_{k,n}^{(m)} \cdot \begin{bmatrix} 1 \\ 1 \\ 0 \\ 0 \\ 0 \\ 0 \end{bmatrix} \tag{5.13}$$

5. **Compute importance weights in global space** The weights for each global particle is computed based on the measurements of globally relevant sensor data (the fit of the covariance matrix $\boldsymbol{R}_n$ and each depth sensor's reading, $\boldsymbol{h}_n$) and the rigidity of the array through an allowable curvature, σ_κ.

$$W_n^{(m)} = \mathbb{P}\left(\boldsymbol{R}_n \mid \widetilde{\boldsymbol{z}}_n^{(m)}\right) \mathbb{P}\left(\boldsymbol{h}_n \mid \widetilde{\boldsymbol{z}}_n^{(m)}\right) \mathbb{P}\left(\widetilde{\boldsymbol{z}}_n^{(m)}; \sigma_\kappa\right) \tag{5.14}$$

6. **Global space resampling** Resample $\widetilde{\boldsymbol{Z}}_n$ with probabilities proportional to their weights, $\boldsymbol{W}_n$, to obtain equally weighted new particles, $\bar{\widetilde{\boldsymbol{Z}}}_n$ with corresponding weights $\bar{\boldsymbol{W}}_n = 1/M$.

7. **Propagate particles** Propagate each global particle to the next time step, $n+1$,

by applying normally distributed random acceleration to each node.

$$\begin{aligned}
x_{k,n+1}^{(m)} &= \bar{\bar{x}}_{k,n}^{(m)} + \bar{\bar{\dot{x}}}_{k,n}^{(m)} \Delta t \\
y_{k,n+1}^{(m)} &= \bar{\bar{y}}_{k,n}^{(m)} + \bar{\bar{\dot{y}}}_{k,n}^{(m)} \Delta t \\
z_{k,n+1}^{(m)} &= \bar{\bar{z}}_{k,n}^{(m)} + \bar{\bar{\dot{z}}}_{k,n}^{(m)} \Delta t \\
\dot{x}_{k,n+1}^{(m)} &= \bar{\bar{\dot{x}}}_{k,n}^{(m)} + a\Delta t, \quad a \sim \mathcal{N}(0, \sigma_a^2) \\
\dot{y}_{k,n+1}^{(m)} &= \bar{\bar{\dot{y}}}_{k,n}^{(m)} + a\Delta t, \quad a \sim \mathcal{N}(0, \sigma_a^2) \\
\dot{z}_{k,n+1}^{(m)} &= \bar{\bar{\dot{z}}}_{k,n}^{(m)} + a\Delta t, \quad a \sim \mathcal{N}(0, \sigma_a^2)
\end{aligned} \tag{5.15}$$

8. **Repeat** Repeat from step 1 for all subsequent time steps

5.2.3 Resampling Methods

There are a number of methods for the importance resampling steps in the method described above. The three most popular algorithms for this purpose are systematic resampling, residual/stratified resampling and multinomial resampling [124]. They all provide comparable performance [128] and systematic resampling is the most straightforward to implement and so is the method that has been implemented here[129].

5.2.4 Priors

The array physical properties are included in the method as probability distributions in each of the weight calculation steps.

5.2.4.1 Inter-node displacement

The inter-node distance is modelled as a one-sided Gaussian distribution about the nominal inter-node distance, d. This gives a maximum probability at the inter-node distance but allows for the rigidity of the array to be encoded into the model, as nodes are allowed to bend closer than the nominal distance between each other. The result is a sphere of equal probability centred on the reference node, shown in Figure 5-4. It is computed as in Equation 5.16 and included at the relative space weight computation step.

$$\mathbb{P}\left(\boldsymbol{z}_{k,n}^{(m)}; d_k\right) = \begin{cases} \exp\left(\frac{-\left(d_k - d_{k,n}^{(m)}\right)^2}{2\sigma_d^2}\right), & d_k^{(m)} \leq d_k \\ 0, & \text{elsewhere,} \end{cases} \tag{5.16}$$

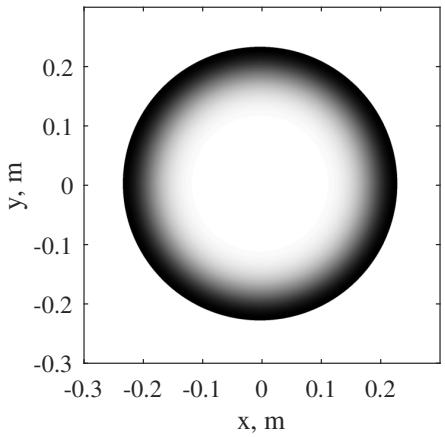

Figure 5-4: Inter-node distance probability distribution. In 3D, it would resemble a sphere of equal probability around the central node.

where

$$d_{k,n}^{(m)} = \left\| \left[\Delta x_{k,n}^{(m)}, \Delta y_{k,n}^{(m)}, \Delta z_{k,n}^{(m)} \right] \right\|. \tag{5.17}$$

Selection of the σ_d parameter is ad hoc but allows slightly more flexibility in shape than a piecewise linear model.

5.2.4.2 Array Rigidity

The rigidity of the array is included in the method as a Gaussian prior computed using the curvature, $\kappa_{k,n}$, at each point along the array, under the assumption that a straight array is the most likely state.

$$\mathbb{P}\left(\widetilde{\boldsymbol{z}}_n^{(m)}; \sigma_\kappa\right) = \prod_{k=1}^{K-2} \exp\left(\frac{-{\kappa_{k,n}^{(m)}}^2}{2\sigma_\kappa^2}\right) \tag{5.18}$$

This is computed using three adjacent nodes and the equation for a circumscribed circle, which is defined as

$$\kappa_{k,n}^{(m)} = \frac{2\left\|\boldsymbol{a}_{k,n}^{(m)} \times \boldsymbol{b}_{k,n}^{(m)}\right\|}{\left\|\boldsymbol{a}_{k,n}^{(m)}\right\| \left\|\boldsymbol{b}_{k,n}^{(m)}\right\| \left\|\boldsymbol{a}_{k,n}^{(m)} - \boldsymbol{b}_{k,n}^{(m)}\right\|} \tag{5.19}$$

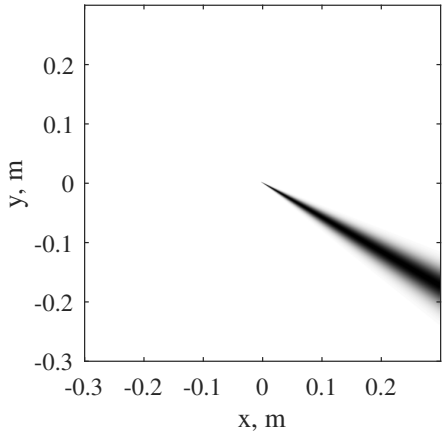

Figure 5-5: A compass measurement PDF. In 3D space, this resembles a cone.

where

$$\boldsymbol{a}_{k,n}^{(m)} = \begin{bmatrix} x_{k-1,n}^{(m)} \\ y_{k-1,n}^{(m)} \\ z_{k-1,n}^{(m)} \end{bmatrix} - \begin{bmatrix} x_{k+1,n}^{(m)} \\ y_{k+1,n}^{(m)} \\ z_{k+1,n}^{(m)} \end{bmatrix}$$

$$\boldsymbol{b}_{k,n}^{(m)} = \begin{bmatrix} x_{k,n}^{(m)} \\ y_{k,n}^{(m)} \\ z_{k,n}^{(m)} \end{bmatrix} - \begin{bmatrix} x_{k+1,n}^{(m)} \\ y_{k+1,n}^{(m)} \\ z_{k+1,n}^{(m)} \end{bmatrix}$$

σ_κ can be selected as one third the maximum allowable bend radius in metres. This property is generally more loosely constraining than the information from the acoustic data or the orientation sensors, so it is less critical to have an extremely accurate estimate. It has been found that it is better to over-estimate the σ_κ as under-estimating will cause the weights to degenerate and the method to fail, whereas over-estimating slightly does not necessarily degrade the performance as much.

5.2.5 Relative Space Likelihood Functions

5.2.5.1 Compass Measurements

A 3-axis compass likelihood function is a Gaussian distribution centred on the compass sensor's reading of heading, θ, and tilt, ψ, with the standard deviation calculated using the sensor measurement variance, σ_θ^2 and σ_ψ^2.

$$\mathbb{P}\left(\theta_{k,n}, \psi_{k,n} \mid \boldsymbol{z}_{k,n}^{(m)}\right) = \exp\left(\frac{-\left(\theta_{k,n} - \theta_{k,n}^{(m)}\right)^2}{2\sigma_{\theta,k}^2}\right) \exp\left(\frac{-\left(\psi_{k,n} - \psi_{k,n}^{(m)}\right)^2}{2\sigma_{\psi,k}^2}\right) \tag{5.20}$$

where

$$\theta_{k,n}(t) = \tan^{-1}\left(\frac{y_{k+1,n}(t) - y_{k,n}(t)}{x_{k+1,n}(t) - x_{k,n}(t)}\right) \tag{5.21}$$

$$\psi_{k,n}(t) = \tan^{-1}\left(\frac{\sqrt{(x_{k+1,n}(t) - x_{k,n}(t))^2 + (y_{k+1,n}(t) - y_{k,n}(t))^2}}{(z_{k+1,n}(t) - z_{k,n}(t))}\right) \tag{5.22}$$

In 3D space, this is a cone shaped distribution with its point on the reference node extending in the direction of the sensor's reading, as shown in Figure 5-5.

5.2.5.2 Inter-Hydrophone Acoustic Phase Difference Estimate

The phase difference between subsequent hydrophones can be estimated and used to provide information in the relative space. Under the assumption that a single arrival in a given frequency band is received from a source, the eigenvector method can be used as an estimate of the phase offset, ϕ, between two hydrophones, as described in Section 3.2.3.2.

The likelihood of a given particle is then given by equation 5.23. This results in a plane of equal probability determined by the angle of arrival of the wavefront, as shown in Figure 5-6.

$$\mathbb{P}\left(\boldsymbol{\phi}_{k,n} \mid \Delta\boldsymbol{z}_{k,n}^{(m)}\right) = \prod_{q=0}^{Q-1} \exp\left(\frac{-\left(\phi_{k,n,q} - \phi_{k,n,q}^{(m)}\right)^2}{2\sigma_{\phi,k,n,q}^2}\right) \tag{5.23}$$

where $\phi_{k,n,q}^{(m)}$ is the expected inter-hydrophone phase difference for the mth particle and $\{f_0, f_1, \ldots, f_{Q-1}\}$ is the set of known sound source frequencies.

The expected inter-node distance is computed using the vector projection of the incident wave vector, $\boldsymbol{\nu}_{n,q}$, onto the vector joining the two adjacent hydrophones,

$$\nu_{n,q} = \begin{bmatrix} \Delta x_{k,n}^{(m)} \\ \Delta y_{k,n}^{(m)} \\ \Delta z_{k,n}^{(m)} \end{bmatrix} \cdot \frac{\boldsymbol{\nu}_{n,q}}{\|\boldsymbol{\nu}_{n,q}\|} \tag{5.24}$$

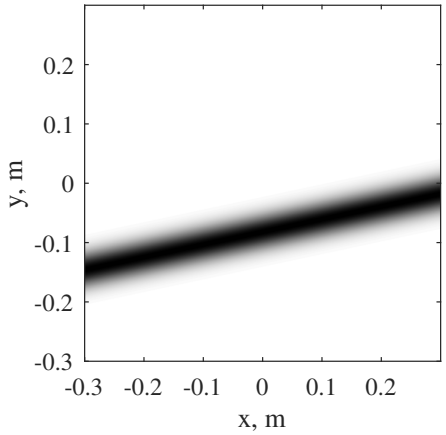

Figure 5-6: Inter-node phase difference probability density in x and y. Extends vertically up and down into the z plane, resulting in a plane of equal probability.

where $\boldsymbol{\nu}_{n,q} = \begin{bmatrix} x_{q,n} \\ y_{q,n} \\ z_{q,n} \end{bmatrix}$. This can then be converted to the expected phase delay as

$$\phi_{k,n,q}^{(m)} = \frac{2\pi f \nu_{n,q}}{c} \tag{5.25}$$

The relation between the standard deviation, $\sigma_{\phi,k,n,q}$, and the SNR in dB can be estimated using Monte Carlo simulations, and found to follow a negative exponential of the form,

$$\sigma_{\phi,k,n,q} = 0.707 \times 10^{-0.05\mathrm{SNR}_{k,n,q}} \tag{5.26}$$

This was computed using 1000 Monte-Carlo (MC) runs with varying bearing to the source and SNRs. Figure 5-7a shows the raw data points and Figure 5-7b shows the standard deviation of the measurement error at each SNR with the corresponding curve fit.

5.2.6 Global Space Likelihood Functions

5.2.6.1 Depth Sensor Measurements

The depth likelihood is computed using a Gaussian distribution about the sensor reading. For a depth sensor co-located with the k^{th} node and with a sensor variance of $\sigma_{h,k}^2$,

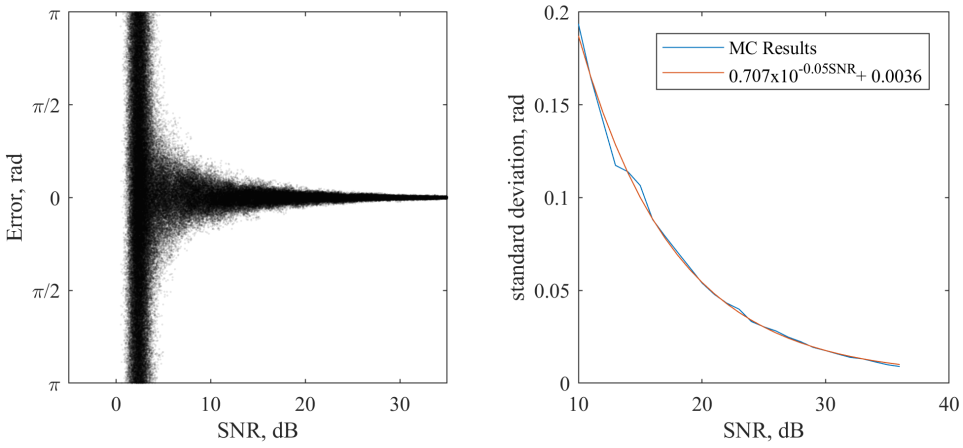

Figure 5-7: Monte Carlo simulations with corresponding curve fit

this is given by

$$\mathbb{P}\left(\boldsymbol{h}_n \mid \boldsymbol{z}_n^{(m)}\right) = \prod_{k=0}^{K-1} \exp\left(\frac{-\left(h_{k,n} - z_{k,n}^{(m)}\right)^2}{2\sigma_{h,k}^2}\right) \tag{5.27}$$

where $h_{k,n}$ is the depth sensor reading. Note, nodes without depth sensors present are set to unity.

5.2.6.2 Beamformer Likelihood

Another way of incorporating the information from the acoustic data is to use the output from a beamforming algorithm, similar to the use of the sharpness in some of the shape estimation methods described in Section 3.

Using the position of the source relative to the array, the expected angle of arrival of the direct path and the surface reflected path can be used to generate two steering vectors for the array. This can be done for each global particle and can then be used to estimate the output power using a beamforming algorithm. This will result in a maximum for the true array shape and will act as a measure of the fit of the covariance matrix to the particle.

Similarly to Equation 5.24, the steering vector can be computed for each global particle using the vector projection of the incident wave vector onto the hydrophone

positions, but this time for the whole array:

$$\boldsymbol{\xi}_{n,q}^{(m)} = \exp\left(i2\pi\frac{f}{c}\left(\boldsymbol{\zeta}_n^{(m)} \cdot \frac{\boldsymbol{\nu}_{n,q}}{\|\boldsymbol{\nu}_{n,q}\|}\right)\right) \tag{5.28}$$

where the spatial coordinate matrix of the particle is defined as

$$\boldsymbol{\zeta}_n^{(m)} = \begin{bmatrix} x_{1,n}^{(m)}, & x_{2,n}^{(m)}, & \ldots, & x_{K,n}^{(m)} \\ y_{1,n}^{(m)}, & y_{2,n}^{(m)}, & \ldots, & y_{K,n}^{(m)} \\ z_{1,n}^{(m)}, & z_{2,n}^{(m)}, & \ldots, & z_{K,n}^{(m)} \end{bmatrix} \tag{5.29}$$

This can then be used to estimate the beamformer power output, for example, using the MUSIC algorithm, $P_{\text{MUSIC},n}^{(m)}$, which can be converted to a likelihood as

$$\mathbb{P}\left(P_n^{(m)} \mid \boldsymbol{z}_n^{(m)}\right) = \exp(\alpha(P_n^{(m)} - \beta)) \tag{5.30}$$

where α and β are tuning parameters which are empirically set. Although more ad hoc than using the inter-hydrophone acoustic phase differences, this method can perform equally well and has the advantage of being able to utilise information from both direct path and multipath of a source.

5.3 Simulation Results

5.3.1 Example

As an example case to illustrate the output of the method, it has been applied to some long-range, linear ray path simulated data, with an acoustic source increasing in SNR as time goes on. Figure 5-8 shows the estimates in x and y with the corresponding ground truth and slices through the estimates at certain points. The colour of the estimate surface corresponds to the spread of the distribution at each node, which is the 1st to the 99th percentile of the estimate. This is shown in the slices in the right hand figures which shows the $[1, 10, 30, 50, 70, 90, 99]$ percentiles, as well as the ground truth. As the SNR increases, the estimate gets more tight around the ground truth, until at a certain point the estimate has completely converged and no further performance increase is possible. The corresponding results for x and z is shown in Figure 5-9. Due to the reduced information from the acoustic data and the increased variance introduced by the depth sensor locating it in vertical space, the spread is consistently fairly broad.

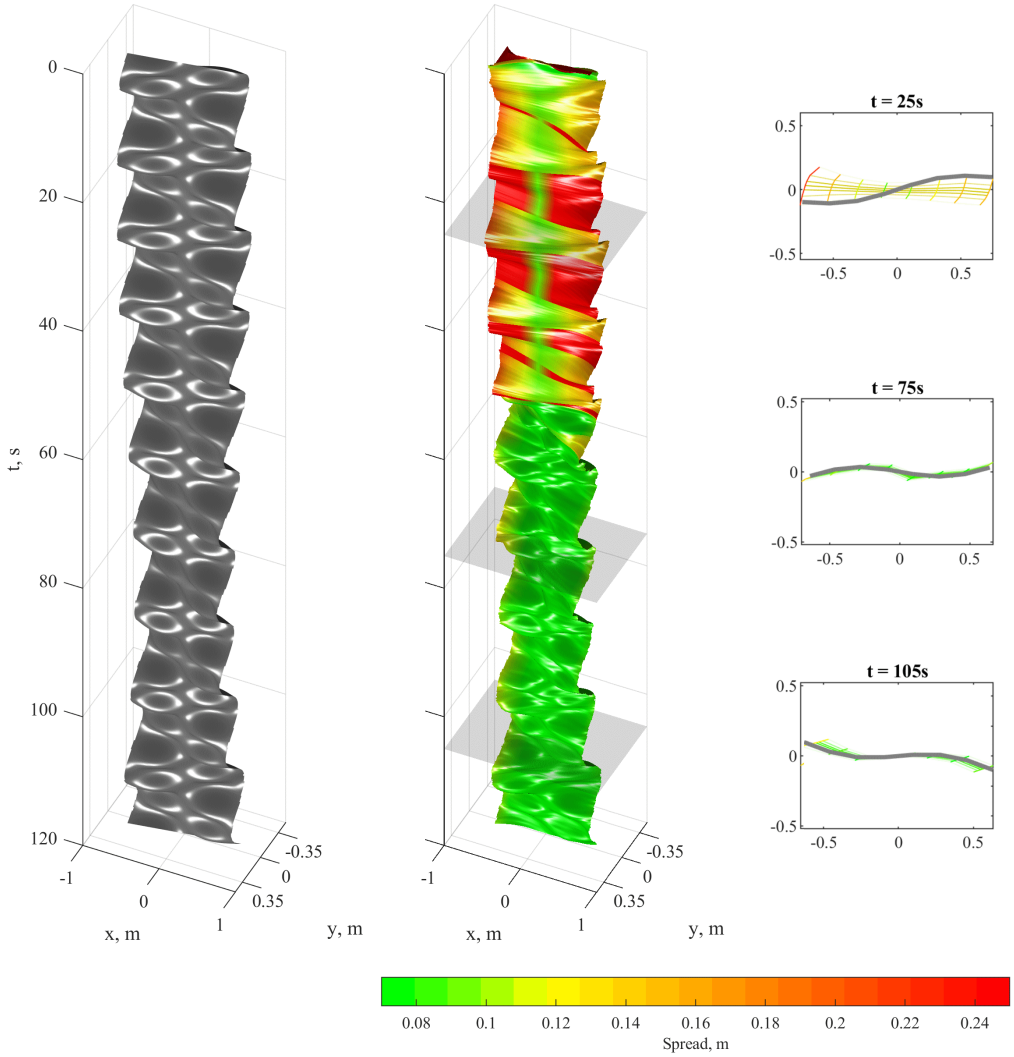

Figure 5-8: (x, y) estimates for an example case. Left is ground truth and central is the corresponding estimate. On the right are slices of the estimate showing the distribution around the ground truth.

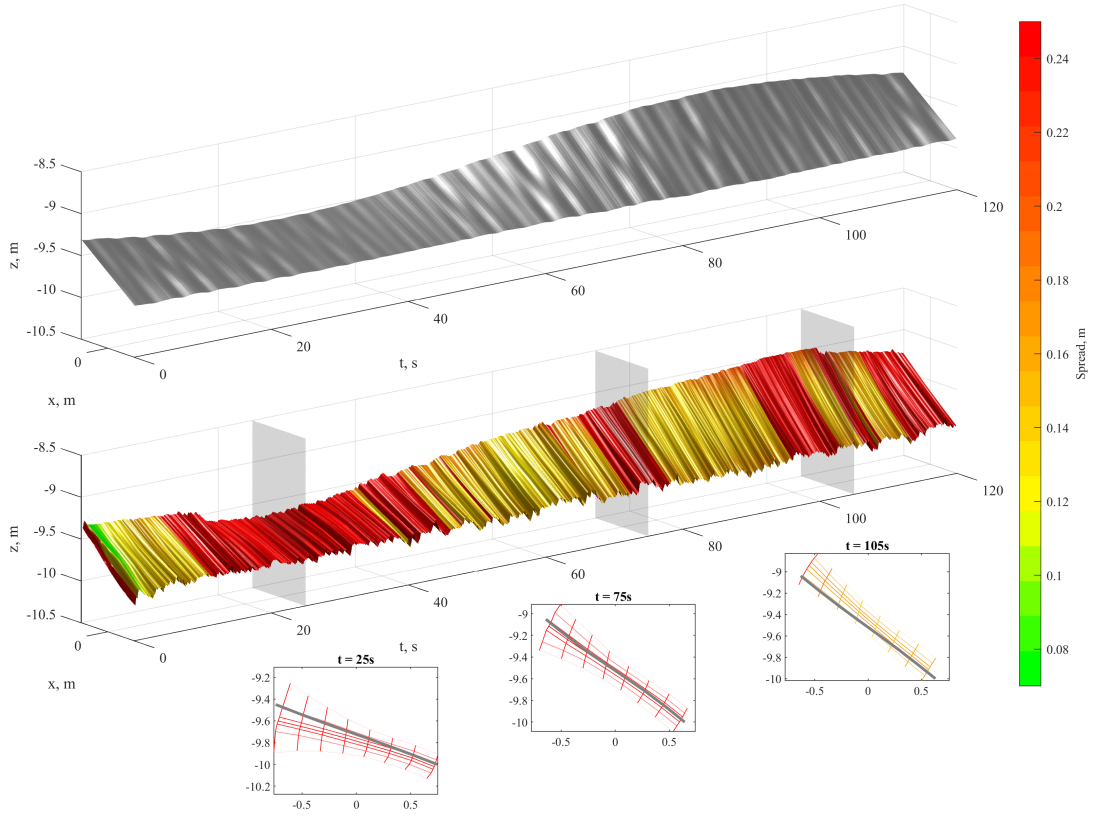

Figure 5-9: (x, z) estimates for long range source test case. Left is ground truth and central is the corresponding estimate. Below are slices of the estimate showing the distribution around the ground truth.

5.3.2 Close Range Source

The simulation test cases introduced in the previous chapter have been used to verify and assess the performance of the algorithm in different scenarios using different types of data for estimation. These resemble the experimental trial being investigated in Chapter 6, each with a different propagation model.

5.3.2.1 Linear Ray Model Dataset

Using the simple, direct path simulation the information from the acoustic data can be included using either the inter-hydrophone phase delay, Figures 5-11 and 5-12, or using the beamformer likelihood, Figures 5-13 and 5-13. As can be seen comparing the two results in Figure 5-11 and Figure 5-13, including multiple frequencies into the estimation slightly increases the accuracy of the result and also enables an accurate estimate at a lower SNR (earlier time). Using the beamformer likelihood instead of the phase offset yields comparable results, although slightly less accurate, similarly with an improved performance when utilising multiple frequencies. As shown in Figures 5-12 and 5-14, the spread in the xz plane is mostly broad for each of the scenarios, due to the lack of constraining information in the z axis.

5.3.2.2 Multipath Dataset

As shown in Figure 5-15b, due to the tilt of the array, the multipath simulation dataset has two distinct arrivals; one due to the direct path and the other due to the surface-reflected multipath. The presence of this multipath arrival renders the phase measurements inaccurate so the beamformer output has to be used to include the acoustic data into the estimation.

Using just the direct path beamformer output with this data set yields similar results to those of the previous dataset, as shown in Figures 5-16 and 5-17. However, incorporating both the direct path and the multipath drastically improves the estimation in both xy and xz, offering better results than any other scenario or configuration.

5.4 Summary

Presented in this chapter is a novel method for shape estimation of a perturbed hydrophone array in operation. A particle filtering technique is used to probabilistically combine all the available sensor data and scenario information to produce an estimate of the array's motion with bounds on the confidence of the estimate. The methods are

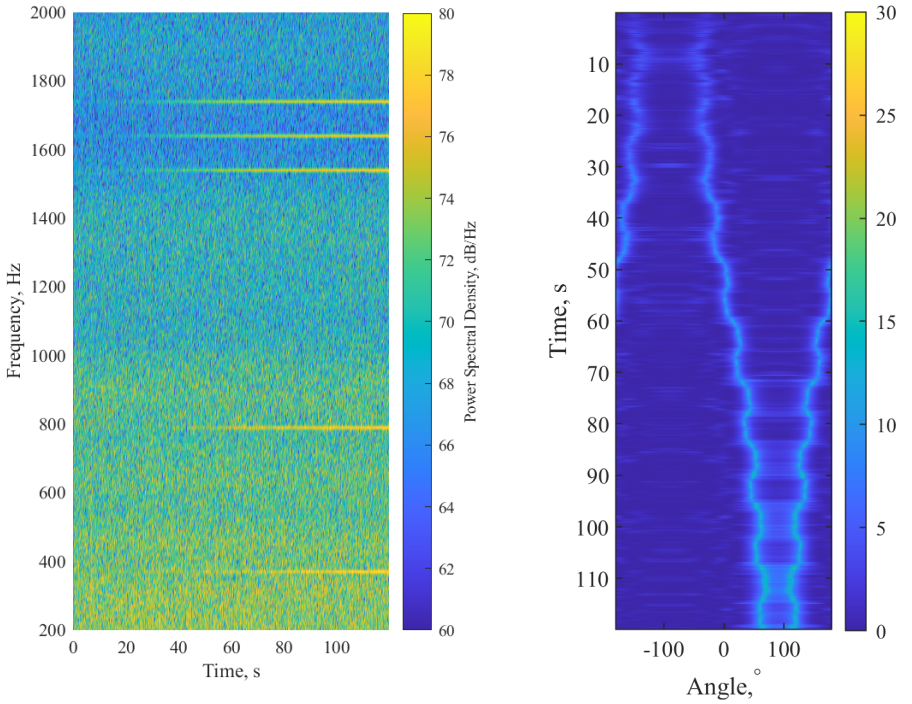

(a) (b)

Figure 5-10: (a)Spectrogram and (b)MUSIC beamformer output for 1540hz for the close-range, direct-path-only simulation dataset

detailed for incorporating the sensor data from 3-axis compasses and pressure sensors as well as two methods of including acoustic data depending on the propagation type.

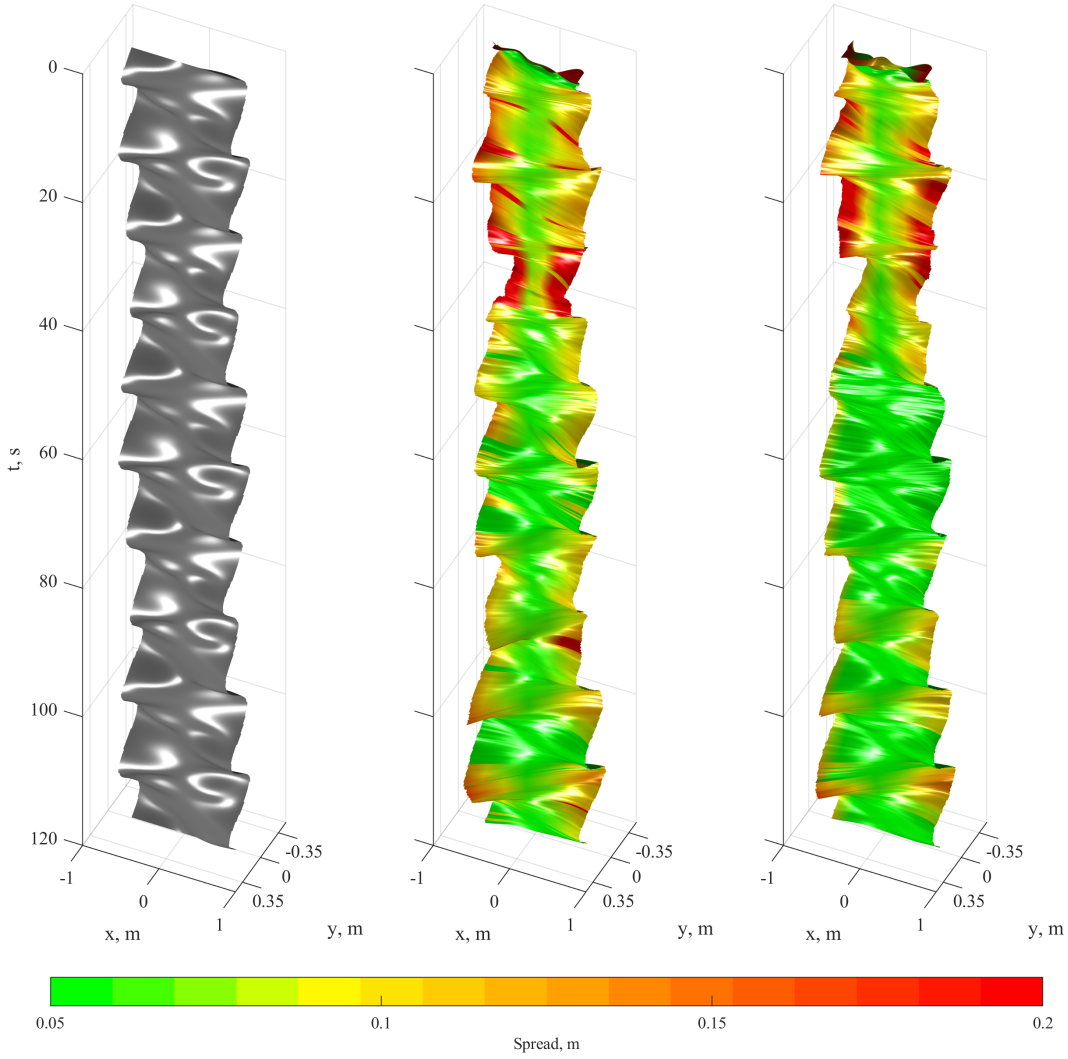

Figure 5-11: Close-range, direct-path-only dataset array (x, y) positions for ground truth(left) and array shape estimates using inter-hydrophone phase offsets for one frequency(middle) and for all frequencies(right)

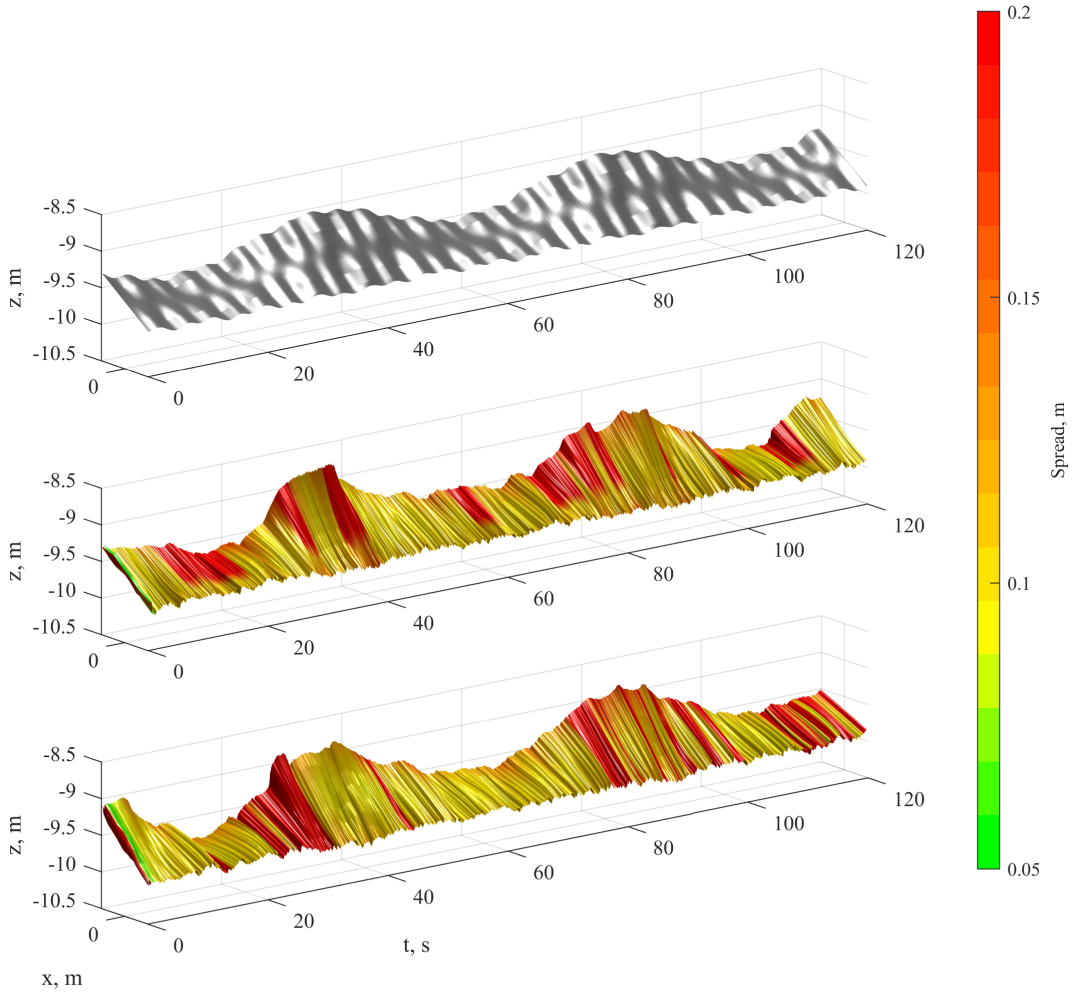

Figure 5-12: Close-range, direct-path-only dataset array (x, z) positions for ground truth(left) and array shape estimates using inter-hydrophone phase offsets for one frequency(middle) and for all frequencies(right)

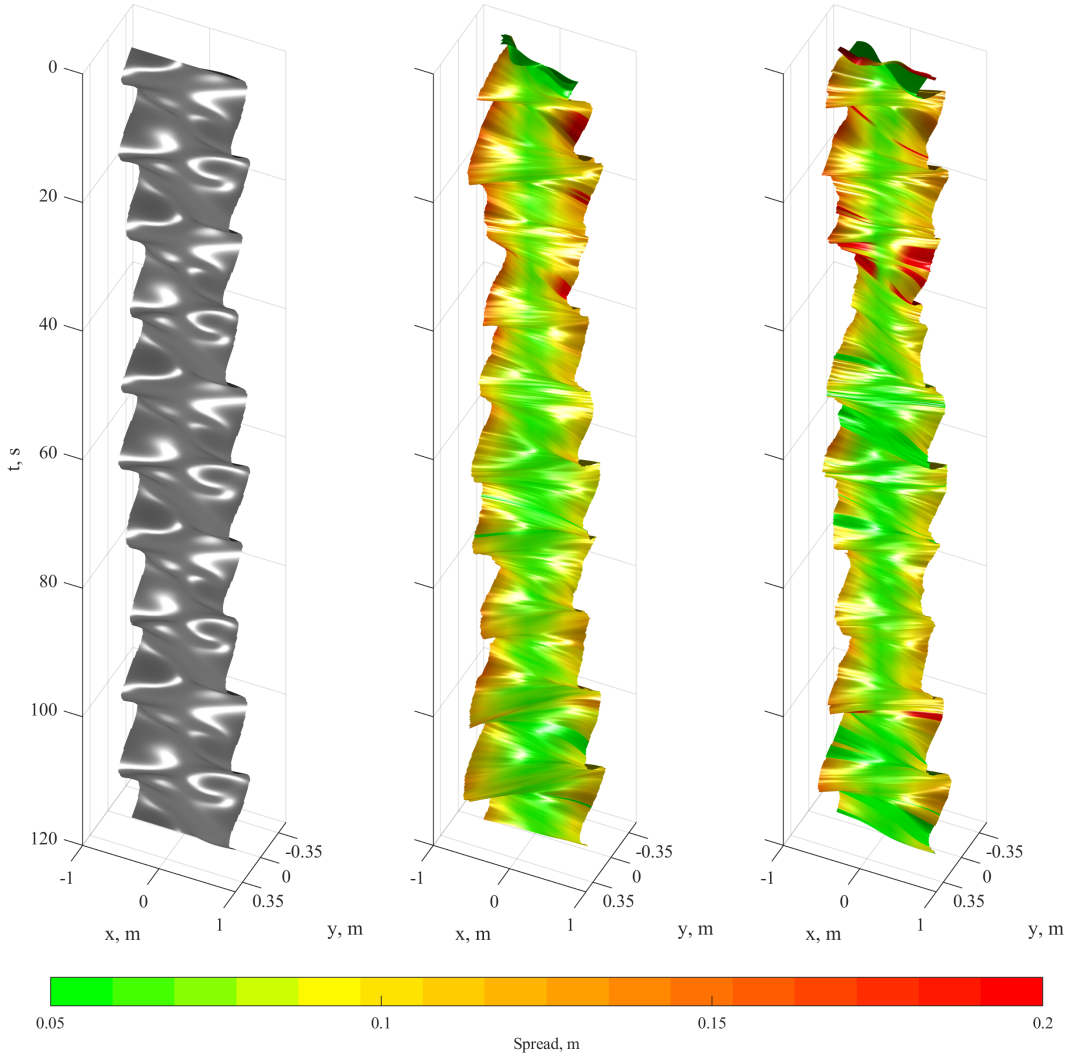

Figure 5-13: Close-range, direct-path-only dataset array (x, y) positions for ground truth(left) and array shape estimates using beamformer likelihood for one frequency(middle) and for all frequencies(right)

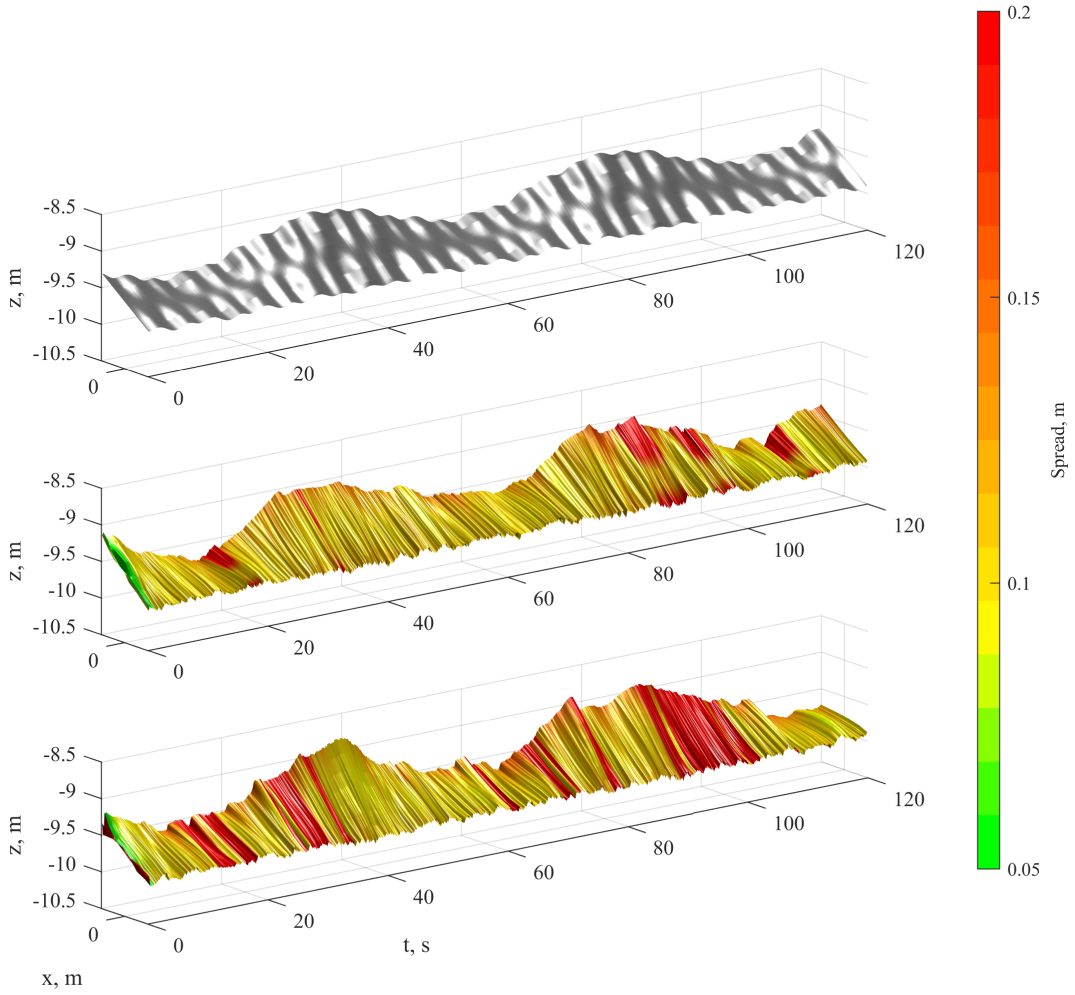

Figure 5-14: Close-range, direct-path-only dataset array (x, z) positions for ground truth(left) and array shape estimates using beamformer likelihood for one frequency(middle) and for all frequencies(right)

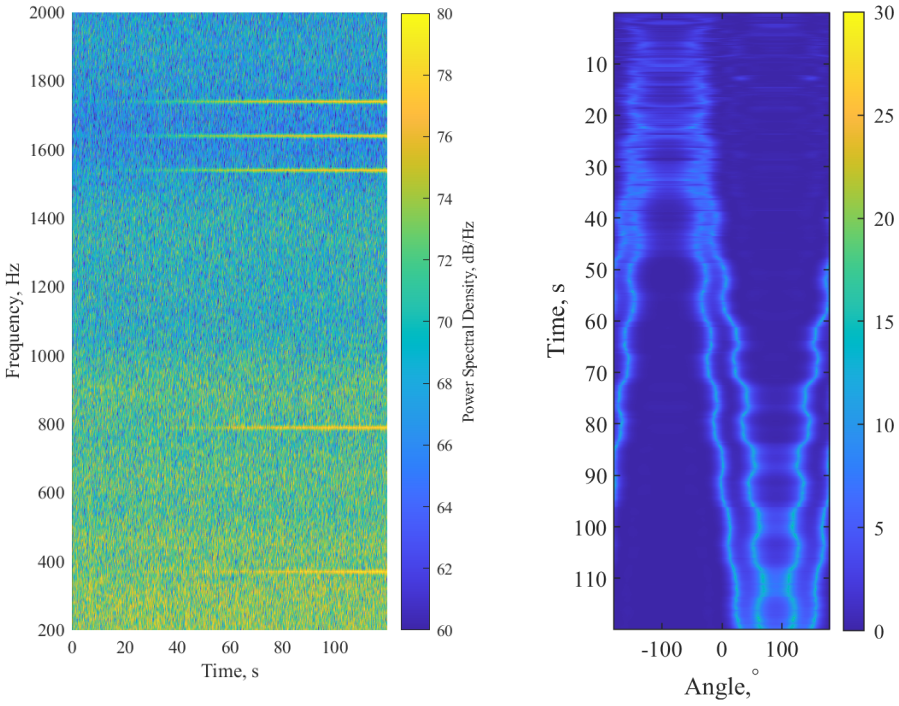

(a) (b)

Figure 5-15: (a)Spectrogram and (b)MUSIC beamformer output for 1540hz for the multipath, undulating-surface simulation dataset

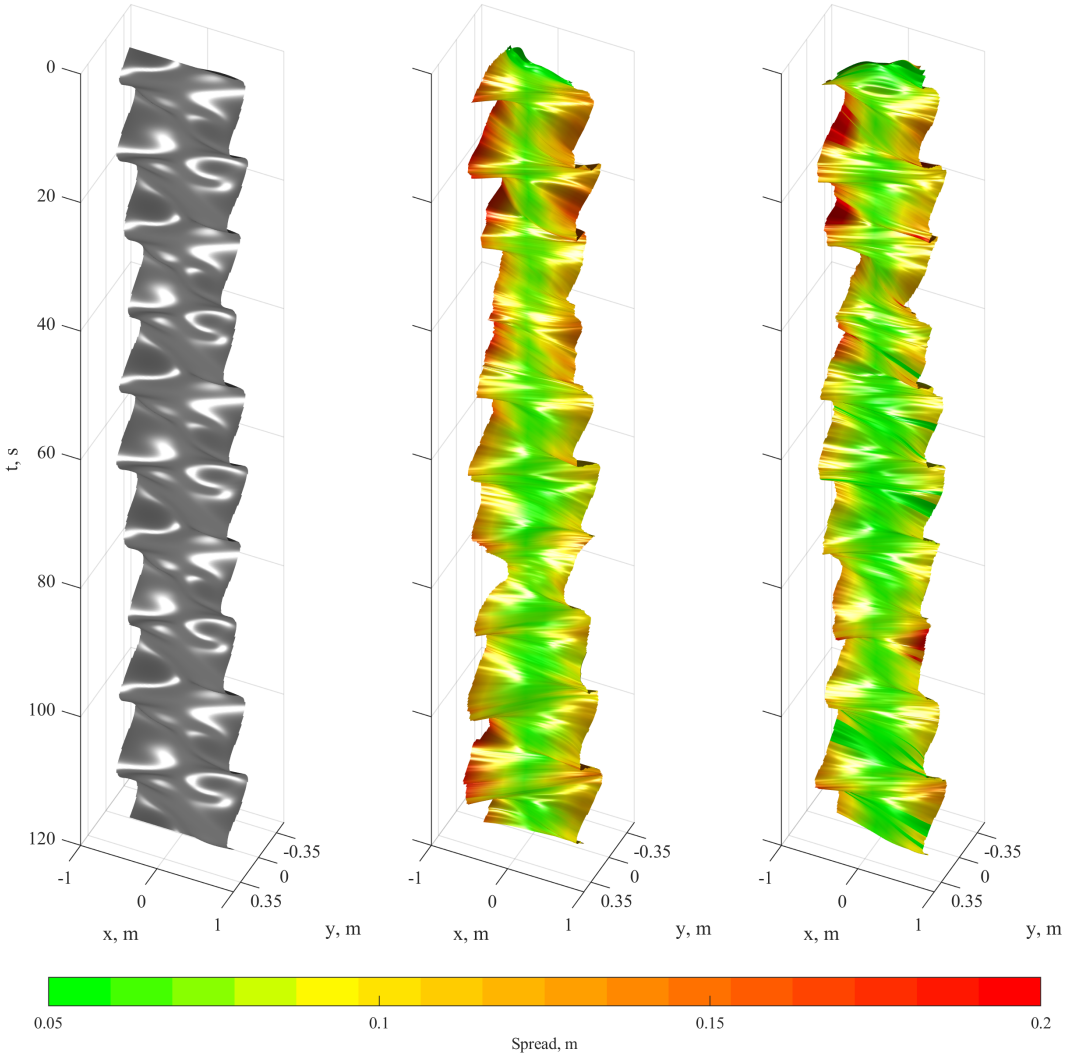

Figure 5-16: Multipath, undulating-surface dataset array (x, y) positions for ground truth(left) and array shape estimates using beamformer likelihood on just the direct arrival for one frequency(middle) and for all frequencies(right)

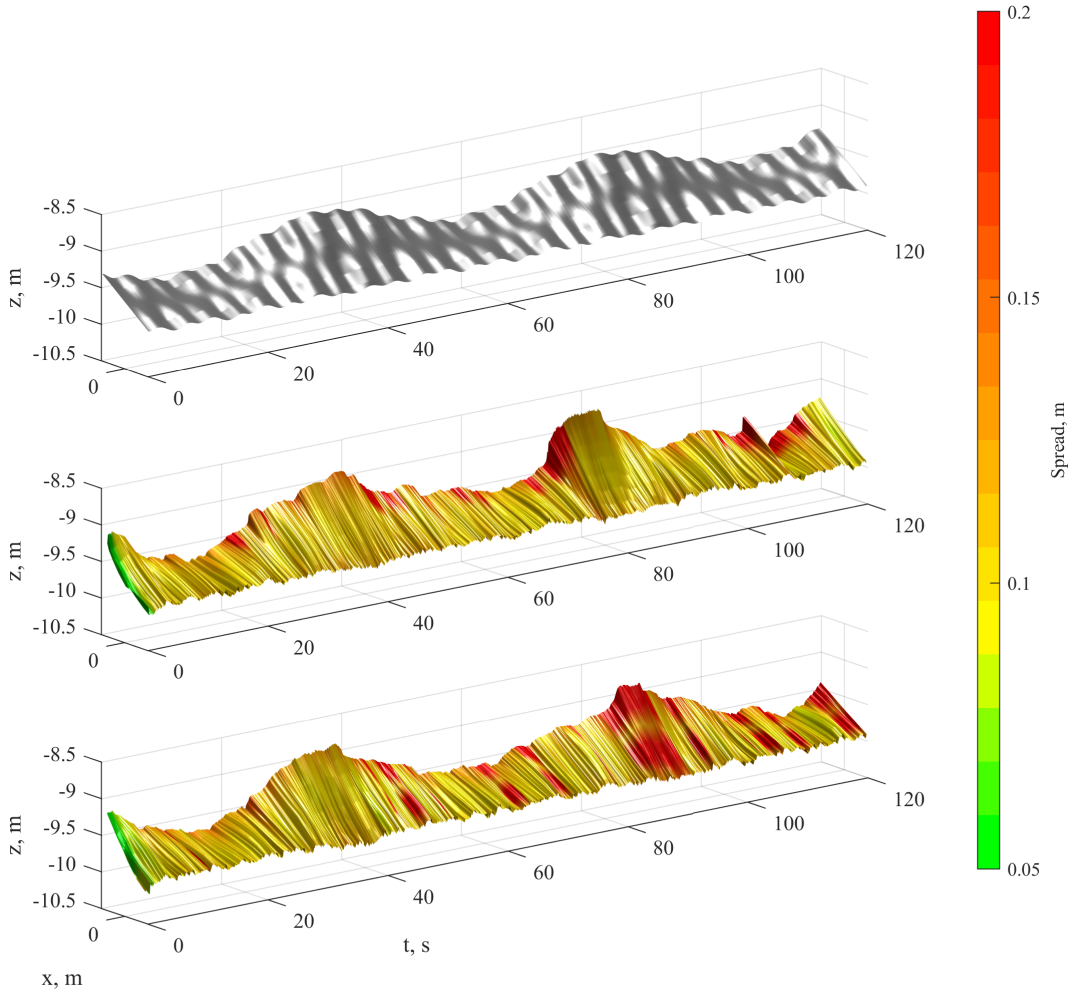

Figure 5-17: Multipath, undulating-surface dataset array (x, z) positions for ground truth(top) and array shape estimates using beamformer likelihood on just the direct arrival for one frequency(middle) and for all frequencies(bottom)

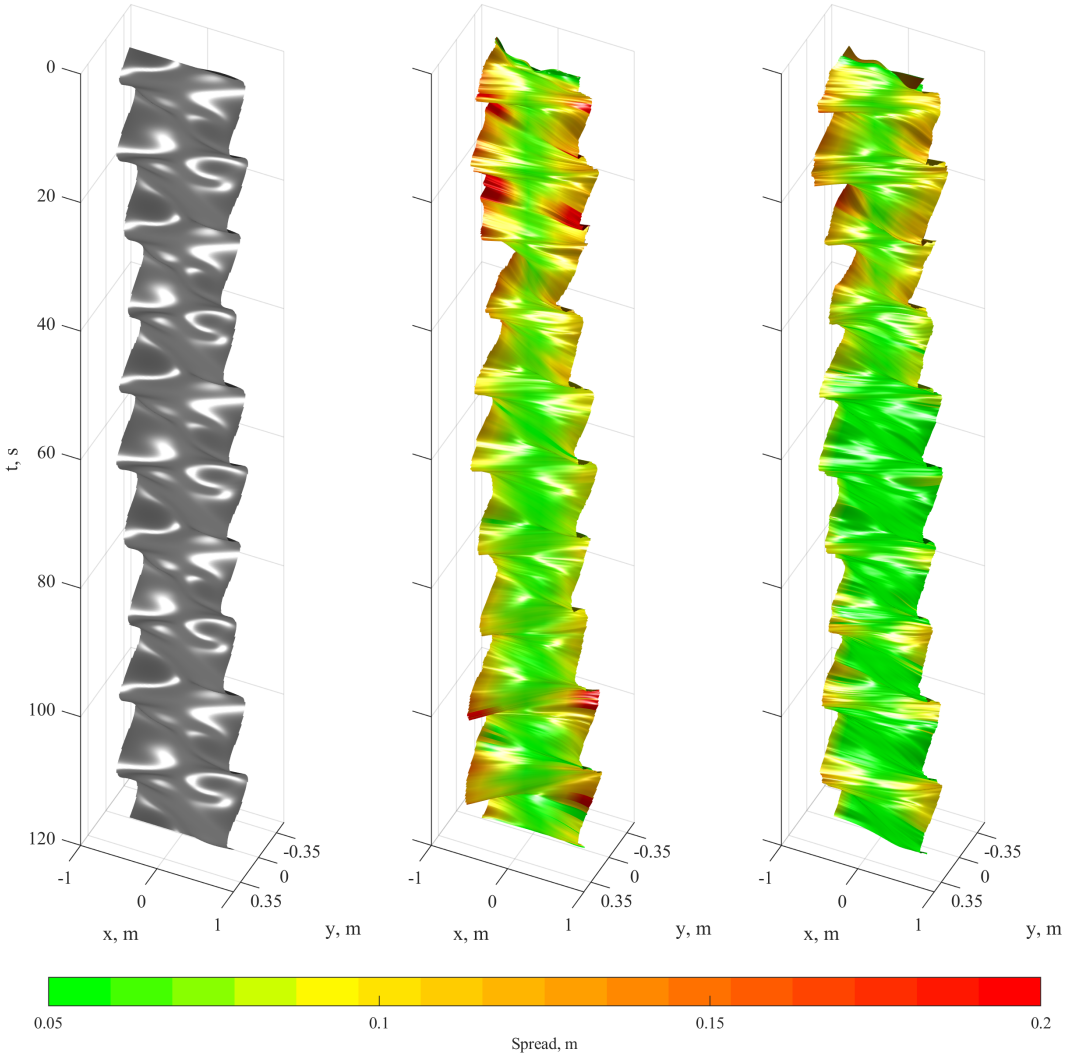

Figure 5-18: Multipath, undulating-surface dataset array (x, y) positions for ground truth(left) and array shape estimates using beamformer likelihood on both the direct arrival and the surface multipath for one frequency(middle) and for all frequencies(right)

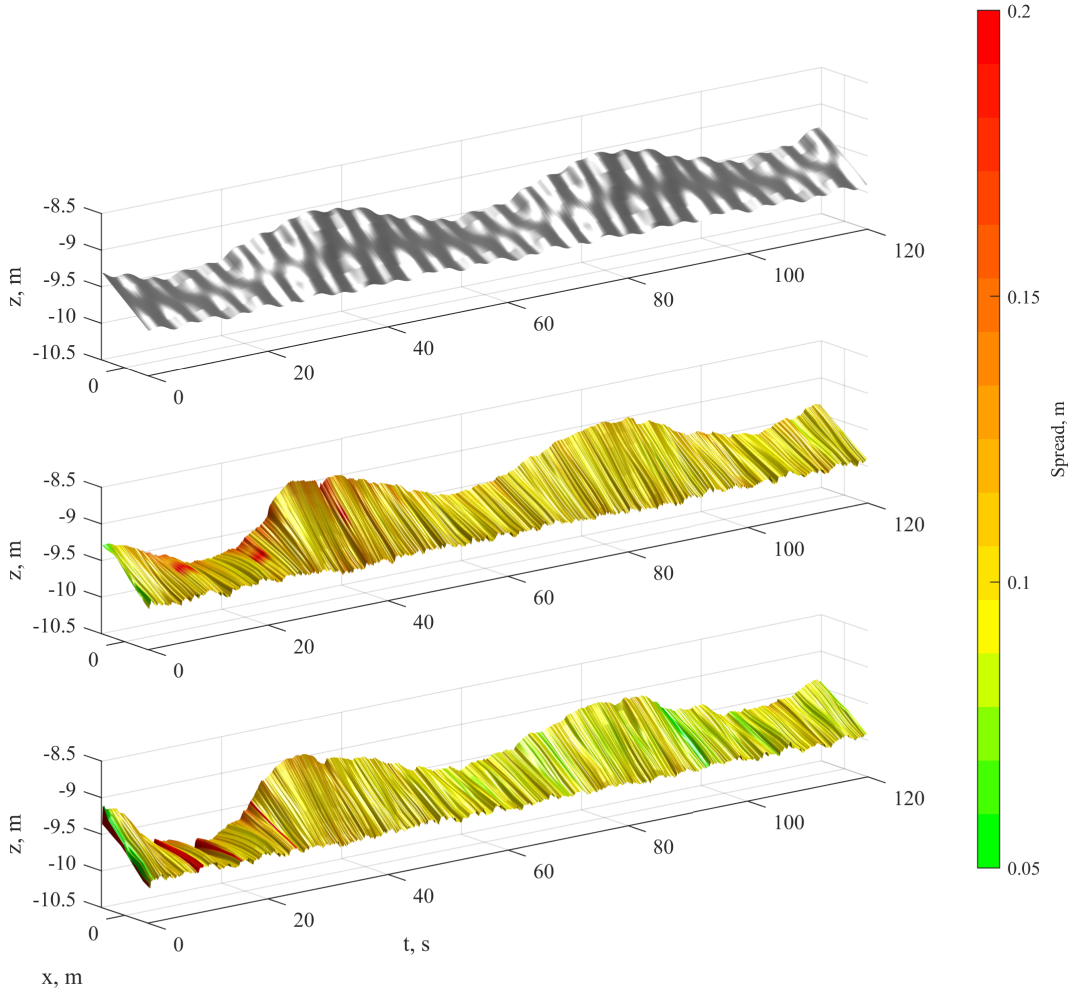

Figure 5-19: Multipath, undulating-surface dataset array (x, z) positions for ground truth(top) and array shape estimates using beamformer likelihood on both the direct arrival and the surface multipath for one frequency(middle) and for all frequencies(bottom)

Chapter 6

Experimental Analysis of Unmanned Warrior '16 Trial

This chapter describes the experimental data used to investigate the use of a passive acoustic array deployed from a wave-propelled USV. The data from a sea trial is used for validation of the simulator described in Chapter 4 and to provide estimates of the array shape in operation using the method described in Chapter 5.

6.1 Overview

The Unmanned Warrior 2016 trial was a large scale demonstration that took place in the Minch sea channel off the coast of Scotland, shown in Figure 6-1. Its aim was to showcase the capabilities of the current state-of-the-art in uncrewed and autonomous maritime technology. Over 50 aerial, surface and underwater systems took part, one of which was an Autonaut USV, pictured in Figure 6-2a. This vessel was deployed equipped with an 8 hydrophone Seiche DTLA, which was instrumented with a compass, attitude, pressure and temperature (CAPT) module at the tail end. In the water nearby was a SAAB AUV with sound projectors emitting acoustic signals throughout the test.

The entire dataset spans over two hours but a two minute section at the closest point between the two vessels is used for subsequent processing, where the acoustic emissions are most prominently detected.

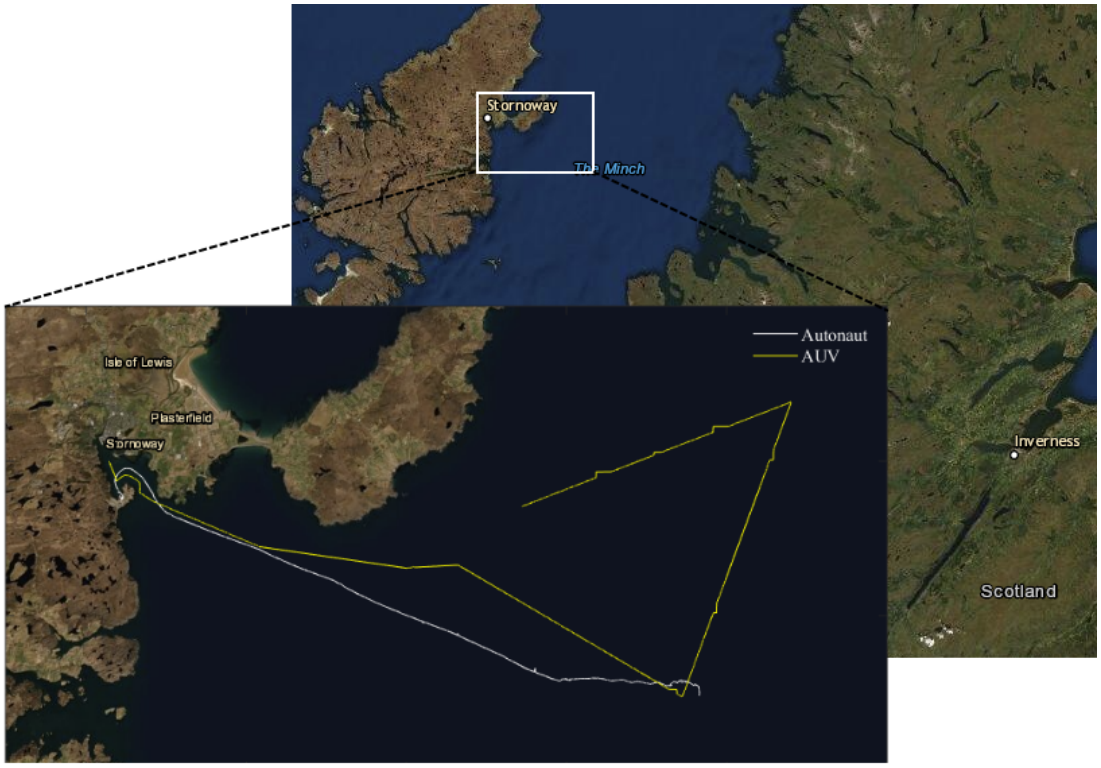

Figure 6-1: Map of trial location showing the GPS tracks of the two vessels

(a) (b)

Figure 6-2: (a) Autonaut and (b) Digital Thin Line Array

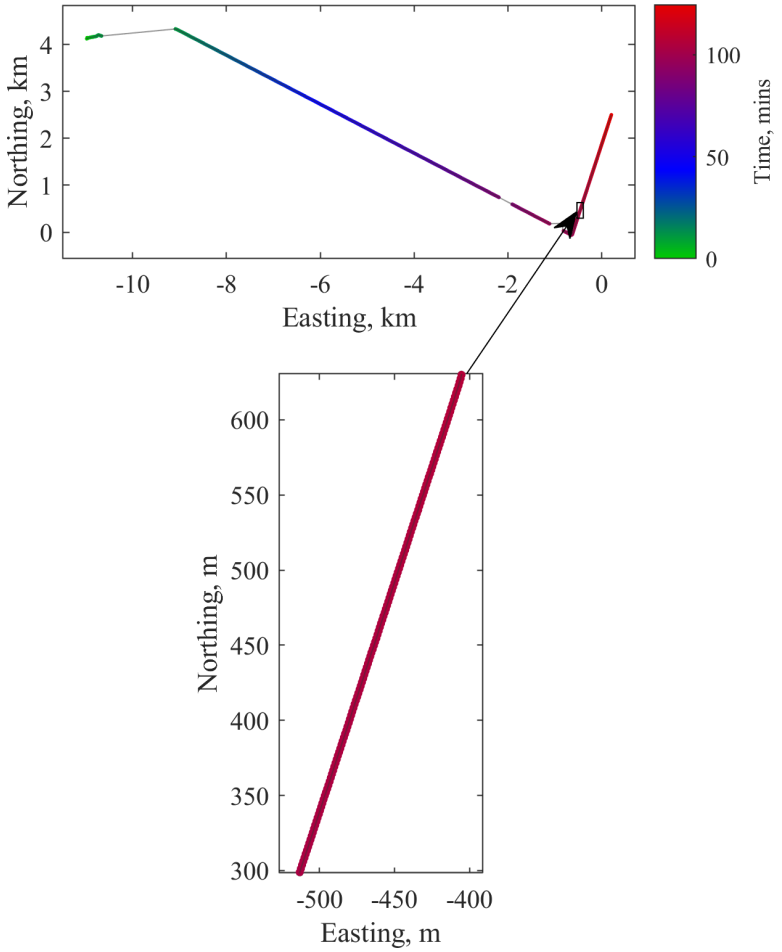

Figure 6-3: (top) AUV GPS track in UTM coordinates with the start of the Autonaut track set at the origin. (bottom) The track for the 2 minute section of data used for the analysis.

6.2 Hardware

6.2.1 AUV

The AUV followed a consistent straight track travelling at between 2-2.5m/s, as shown in Figure 6-3. It surfaced a number of times during the trial for a GPS lock and then used a Doppler velocity logger to accurately estimate its position when submerged. During the two minute section of data it was travelling as in the bottom panel in Figure 6-3, at a depth of 40m. Throughout the trial projectors on the AUV were emitting a series of continuous tonal signals and a frequency modulated signal, as described in Table 6.1.

Table 6.1: AUV emission frequencies and source levels

Centre frequency, Hz	Source level, dB re. 1μPa	Modulation
190	129	-
370	124	-
790	127	-
1640	132	FM so energy is spread over 100Hz spaced frequencies

6.2.2 Autonaut

The Autonaut vessel used was a 5m vessel with a stated design speed of 1-3 knots (0.5-1.5m/s) depending on conditions. During the trial, it travelled at an average speed of roughly 0.25m/s, along the track shown in Figure 6-4. Being wave-propelled, the track is slightly more erratic than that of the AUV.

6.2.3 DTLA

The towed Seiche DTLA is designed specifically for deployment from smaller low-powered vessels and so is just 20mm in diameter to reduce drag. It features 8 hydrophones spaced 0.23m from each other and each hydrophone was sampled at a rate of 12kHz. This gives the array a maximum operating frequency of 6000Hz and a maximum beamforming operating frequency of 3261Hz.

6.2.3.1 CAPT Module Data

The non-acoustic instrumentation on the array consisted of a single CAPT module, located at the tail-end of the array 90mm from the end hydrophone. This module consists of a pressure sensor for depth and a 3-axis compass sensor capable of measuring the heading and tilt of the array. The error on each of the sensors has been assumed Gaussian and the standard deviation set to a third of the full-scale error. As such, the compass has an error standard deviation of 3^o and the pressure sensor error standard deviation is 0.05bar.

As can be seen by comparing Figure 6-5a to Figure 6-5b, the general trends in the heading of the array and the heading of the vessel match up but the magnitudes are largely different. Figures 6-5c and 6-5d also match up consistently, with a greater tilt on the array resulting in an increase in depth.

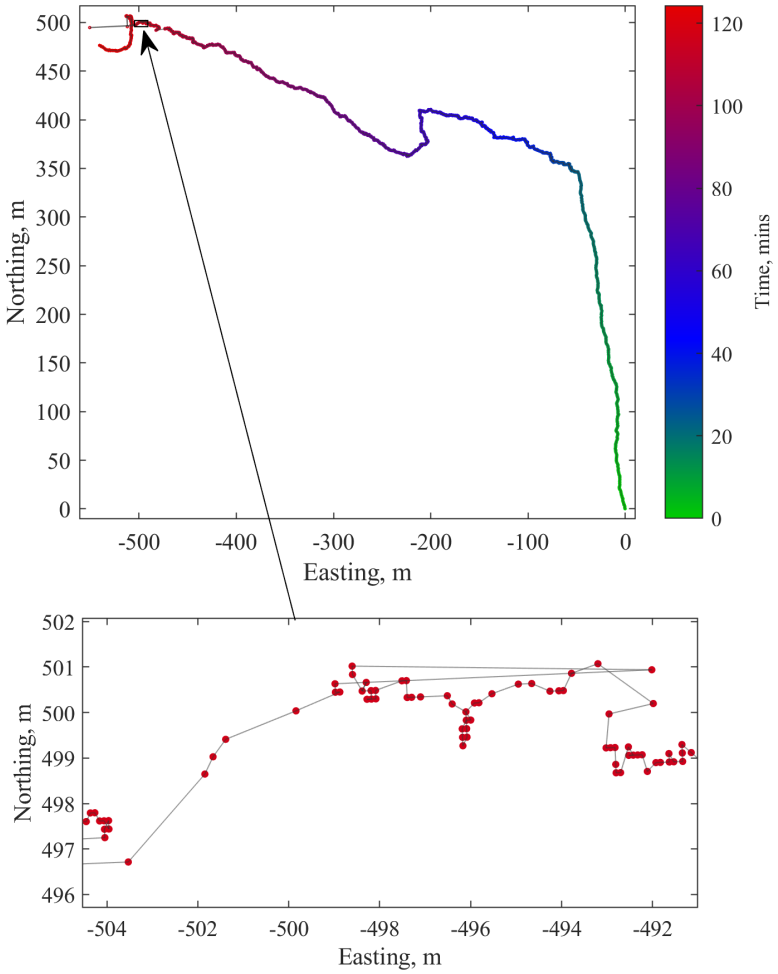

Figure 6-4: (top) Autonaut GPS track in UTM coordinates with the start of the track set at the origin. (bottom) The track for the 2 minute segment of data used for further analysis.

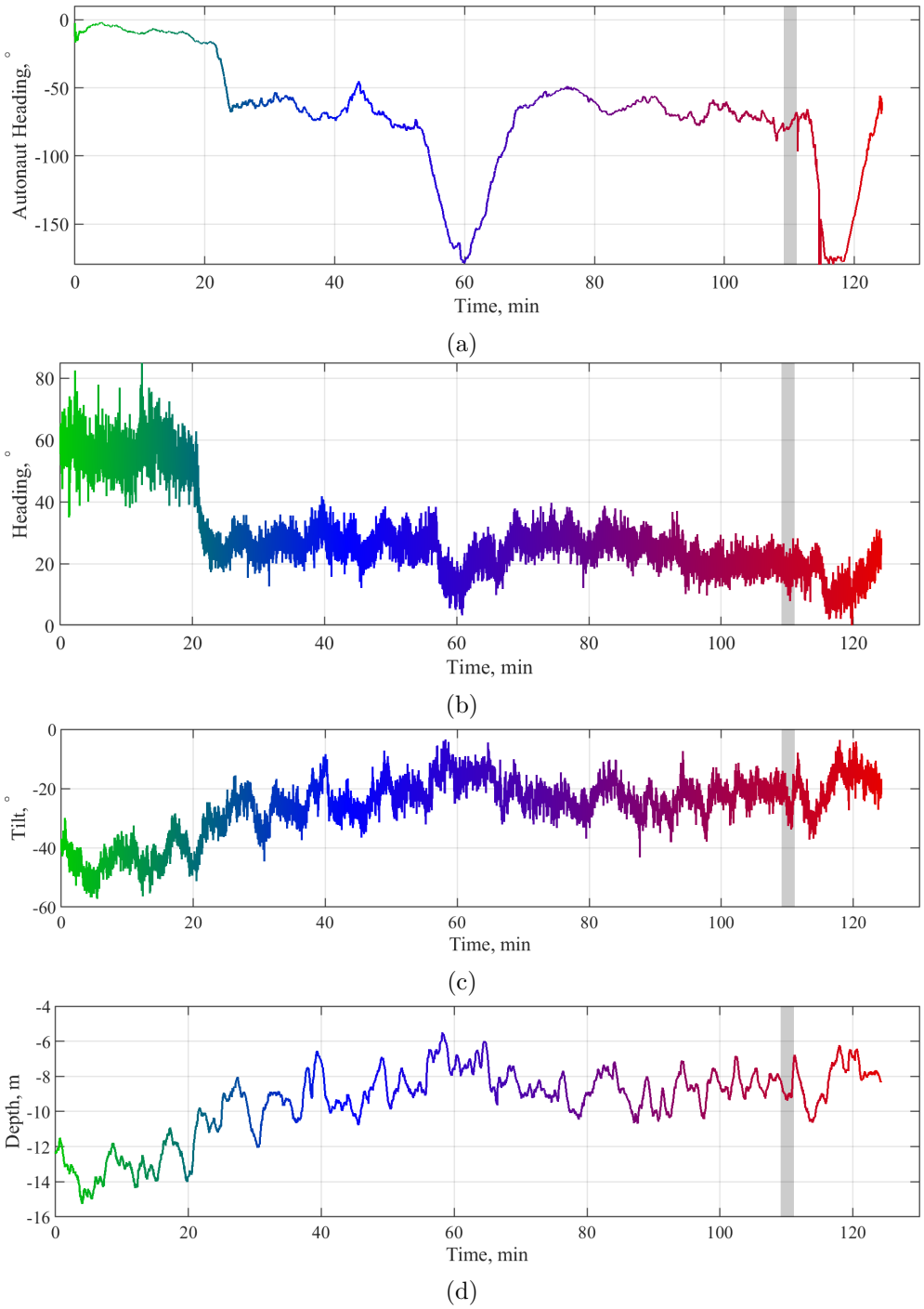

Figure 6-5: (a) AutoNaut heading and sensor readings for the tail (b) heading, (c) tilt and (d) depth. Line colour corresponds to the GPS track of figure 6-4. The shaded section shows the 2 minute segment of data used in the analysis.

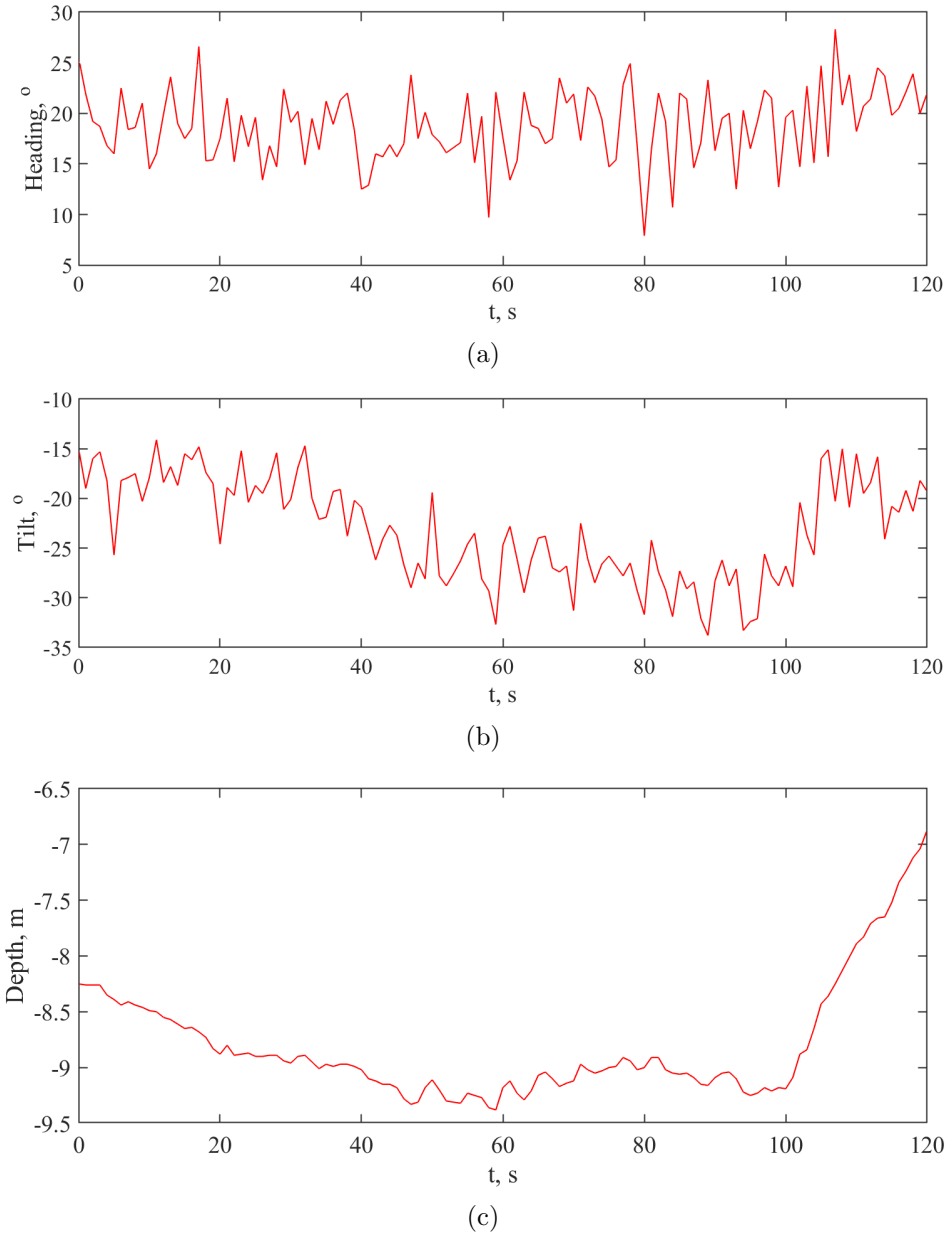

Figure 6-6: Sensor readings for the tail (a) heading, (b) tilt and (c) depth, corresponding to the grey area on Figure 6-5

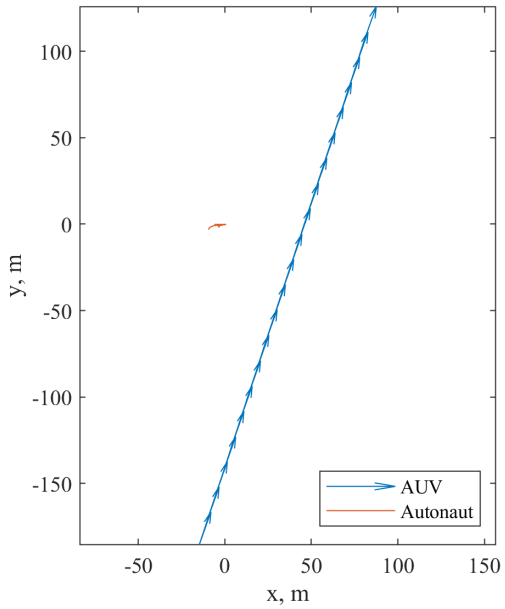

Figure 6-7: AUV and Autonaut GPS track for the two minute segment used in the analysis

6.3 Simulated Data Validation

The dataset from the trial was used as validation for the simulator described in Section 4. Two simulation datasets were produced with slightly different parameters.

6.3.1 Parameters

The array position was set to a straight array positioned at the origin and oriented according to the CAPT sensor data, shown in Figure 6-6. The sound source was set according to Table 6.1 with a position at the relative displacement between the Autonaut and AUV, as in Figure 6-7. The noise spectral profile was set according to the average level of a 20 second portion of data with no signals present, the same as that in Figure 4-8. The Bellhop model parameters used were a water column depth of 103m, with a linearly increasing SSP from 1500 m/s at the surface to 1502 m/s at the seafloor.

The first simulation dataset was produced with a stationary reflective sea surface and the second dataset had a sea surface oscillating with a period of 8s and amplitude of 1m, as would be consistent with the location and time of year [130].

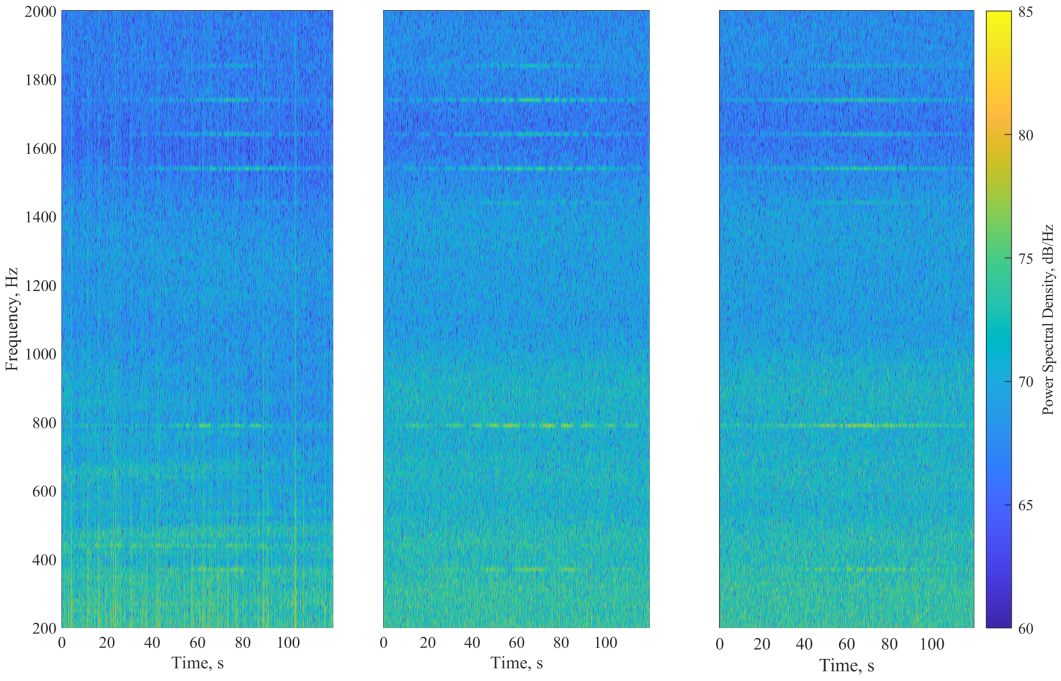

(a) (b) (c)

Figure 6-8: Spectrograms for (a)the experimental data, (b) simulated data with reflective stationary sea surface and (c) simulated data with reflective slowly oscillating sea surface

6.3.2 Results

6.3.2.1 Spectrograms

Figure 6-8 shows a comparison of the spectrograms from the experimental data and the two simulation datasets with a bin width of 10Hz. The interference pattern resulting from the interaction of the direct path and the multipath can be seen in each plot and fairly closely matches.

Figure 6-9 shows the result of computing the spectrogram with a much finer 1Hz bin width and zooming in on one of the frequencies of interest. The detection is doppler shifted from 1540Hz up to roughly 1542Hz before 60s and down to 1538Hz after, which is accurately captured in both simulation sets. The bleeding of the signal into adjacent bins which occurs in the experimental data can also be seen to occur in the oscillating sea surface dataset, albeit to a slightly higher degree.

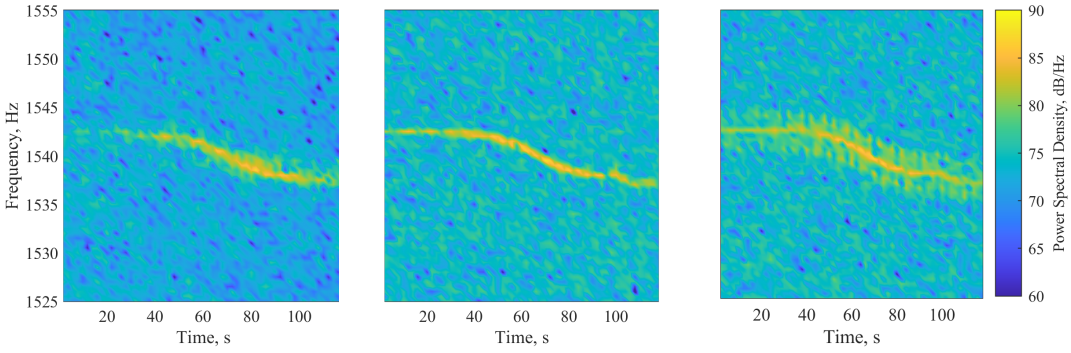

(a) (b) (c)

Figure 6-9: Close up spectrograms for (a)the experimental data, (b) simulated data with reflective stationary sea surface and (c) simulated data with reflective slowly oscillating sea surface

Table 6.2: Beamformer parameters

Bin width	10Hz
Time window	0.2s
Overlap	0.1s
Moving average N	10
Expected number of sources (MUSIC parameter)	2

6.3.2.2 Beamforming

Applying the MUSIC beamformer to each dataset with the parameters in Table 6.2 yields the results in Figure 6-10. The output from the simulator bears a strong resemblance to the experimental data, falling somewhere in between the two datasets when examining the features of the result. This is to be expected as the oscillating sea surface simulation dataset follows a sinusoidal pattern whereas in reality the surface perturbations would be more random, with periods of stationarity.

The two detections are clearly visible in each dataset, caused by the direct path and the surface reflected multipath. The effect of an oscillating sea surface is a decrease in the coherence between the direct path and the surface-reflected multipath, causing the two detections to be far more distinct. The Doppler shift on the signals along with the different path lengths also reduces the coherence between the direct and the multipath, although to a lesser extent. This is also the cause of the reduced magnitude spot at around 70s, which corresponds to the closest point of approach. At this point the interference between the two coherent arrivals causes a drop in the beamformer estimate magnitude, visible in the experimental data and the first simulation dataset but not in the second.

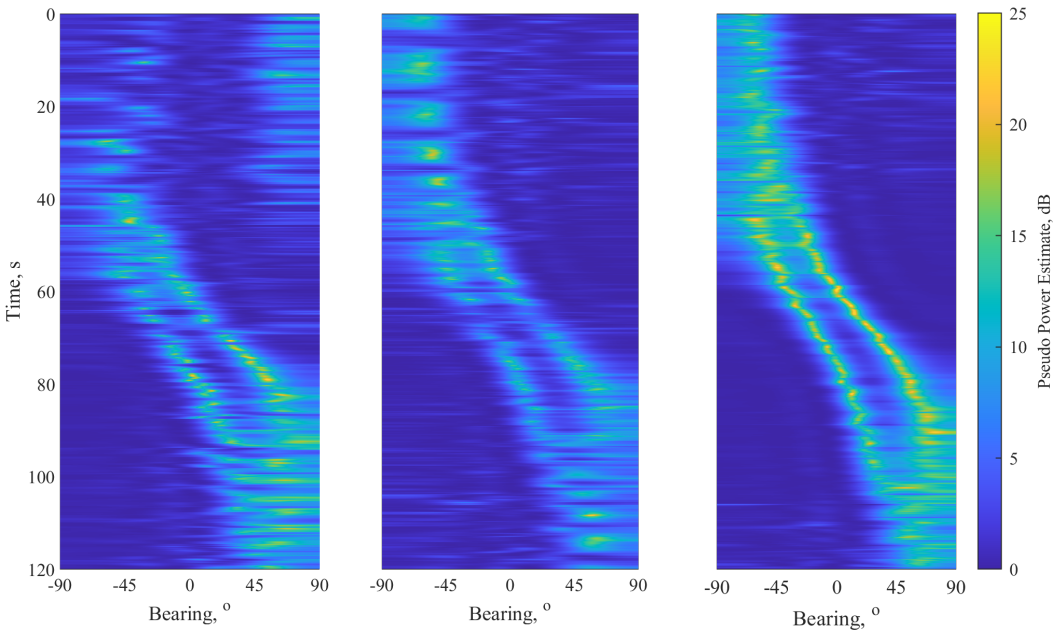

(a) (b) (c)

Figure 6-10: MUSIC beamformer power estimate at 1540Hz with a 10Hz for (a)the experimental data, (b) simulated data with perfectly reflective stationary sea surface and (c) simulated data with slowly oscillating sea surface

Some points of difference between the experimental results and the simulation are the increased magnitude between 0s and 40s at a bearing of around 45^o. This is caused by sea surface noise, occuring at that bearing because of the tilt on the array. Also, in the simulation datasets the detections occur at a greater magnitude earlier than those of the experiment. This is probably because of the reduced omnidirectionality of the real sensors and projector used in the trial.

6.4 Array Shape Estimation

In order to investigate the motion of the array in operation, the method described in Section 5 has been applied to the data from this trial. The four configurations for the available data described in Table 6.3 were used to examine the effect of incorporating more data into the method. Taking the rule of thumb of $< \lambda/10$ sensor position uncertainty (as described in Chapter 3) results in a target of 0.046m for the array design frequency of 3250Hz.

Table 6.3: Shape estimation configurations

Configuration	1	2	3	4
Frequency(s)	1540Hz	1540Hz, 1640Hz, 1740Hz	1540Hz	1540Hz, 1640Hz, 1740Hz
Beamformer output	Direct path only	Direct path only	Direct path and multi-path	Direct path and multi-path

6.4.1 Method Parameters

The parameters in Table 6.4 were used for the shape estimation algorithm. They were decided based on the trial data in the following ways:

- The acceleration and velocity standard deviations were selected using the motion of the boat, which was travelling with a mean speed of 0.22m/s and an acceleration standard deviation of 0.07m/s^2 during the 2 minute section of data.
- The inter-element standard deviation was selected as a low value to keep the inter-element distance fairly close to nominal.
- The curvature standard deviation is based on the bend radius of the array when stored on a storage drum which is roughly 0.25m. This translates to a curvature of 4m^{-1} so setting that to the 3σ results in $\sigma = 1.3\text{m}^{-1}$.

- The beamformer likelihood parameters were found through empirical testing of different parameters in simulation with a dataset representative of the dataset.

Table 6.4: Array shape estimation parameters

Acceleration standard deviation	0.07m/s^2
Velocity standard deviation	0.07m/s
Inter-element d standard deviation	0.05m
Curvature standard deviation	1.3m^{-1}
Beamformer likelihood α	0.07
Beamformer likelihood β	20
N	200000

6.4.2 Results

6.4.2.1 Array Shape Comparison

Figure 6-11 shows the comparison of the array shape estimates in (x, y). In terms of the spread of the estimate the result is consistent with that of the simulated results presented in Chapter 5, with the best quality estimate generated from the result incorporating all the high frequencies with both the direct and the multipath. Figure 6-12 show a reduced ability to resolve in the (x, z) plane, again consistent with simulation, but also show an improvement with the increased amount of incorporated data. Looking at the deviation from a nominally straight array for Configuration 4, shown in Figure 6-13, shows that the array generally seems to be mostly straight, with periodic sections of larger perturbation.

6.4.2.2 Beamformer Output Comparison

The MUSIC spectrum was computed for the array assuming a straight array oriented according to the heading sensor (herein referred to as the uncompensated result), as in Figure 6-10a. The steering vector was then compensated with the array shape estimate and then the MUSIC spectrum was computed again using this new steering vector. Figure 6-14 shows the difference in the maximum spectrum values between uncompensated and compensated for each configuration. The increase in MUSIC spectrum output suggests that the compensated shape is closer to the true shape than a straight array assumption. Configuration 4 has the highest average increase and the most consistent increase, displayed in the bottom graphs that show the histograms of the difference. Again, this also suggests that configuration 4 is the best estimate of the array shape in operation especially in that section of the dataset. These results are

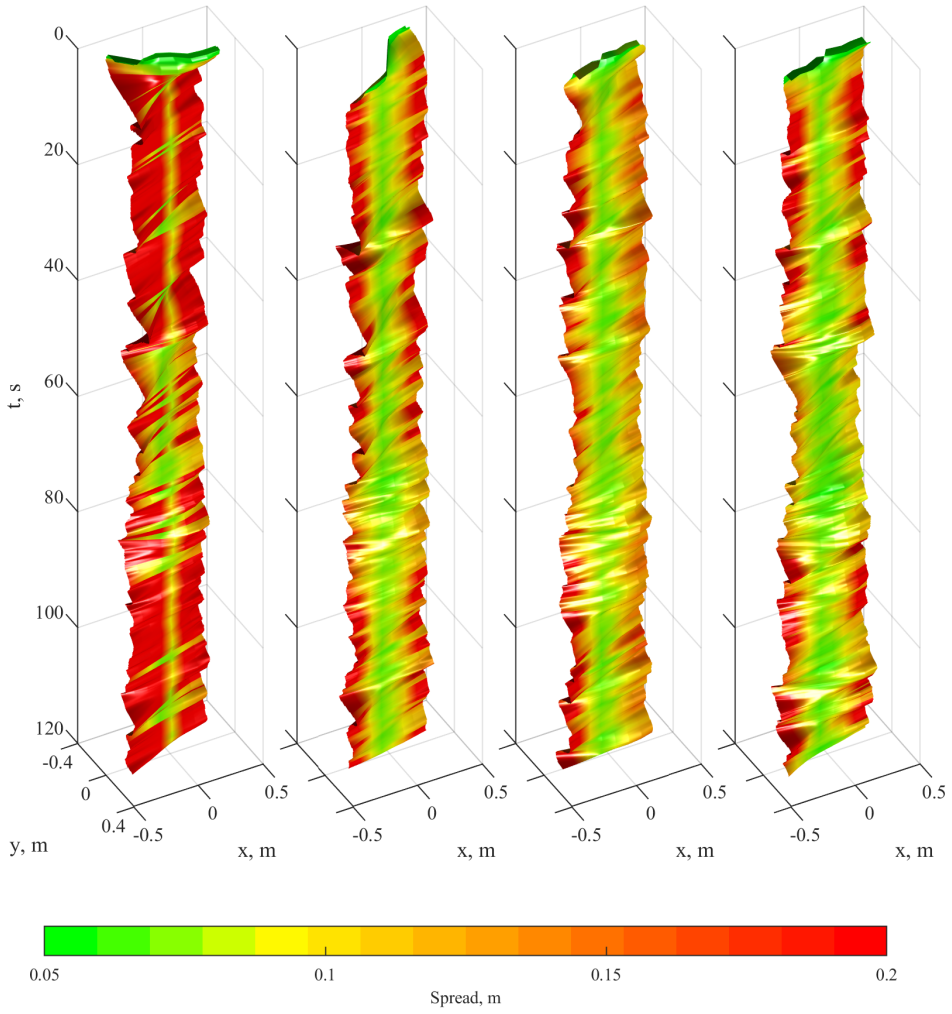

Figure 6-11: Array shape estimates for experimental data in x and y. (Far left) 1540Hz with direct path only, (middle left) all high frequencies with direct path only, (middle right) 1540Hz with direct and multipath and (far right) all high frequencies with direct and multipath

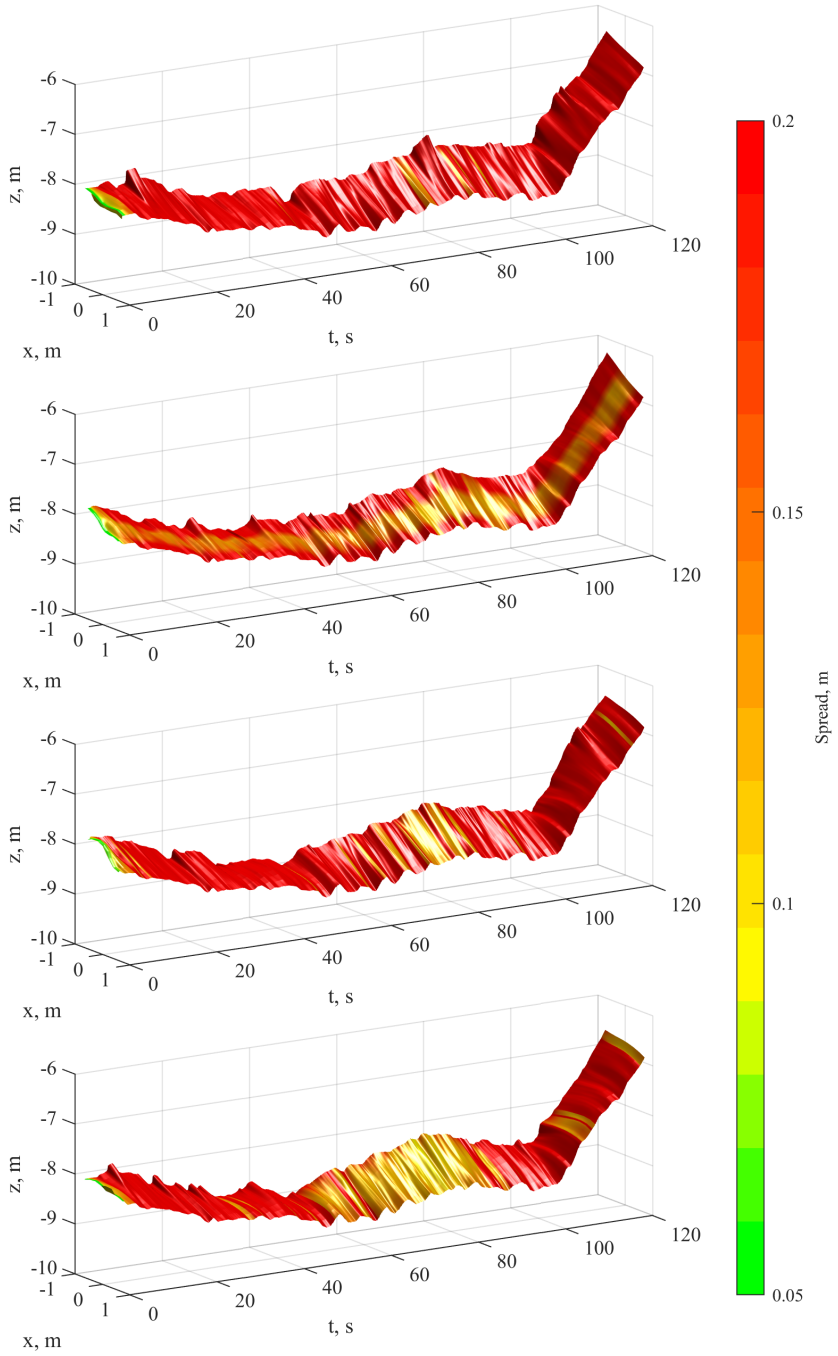

Figure 6-12: Array shape estimates for experimental data in x and y. (Top) 1540Hz with direct path only, (upper middle) all high frequencies with direct path only, (lower middle) 1540Hz with direct and multipath and (bottom) all high frequencies with direct and multipath

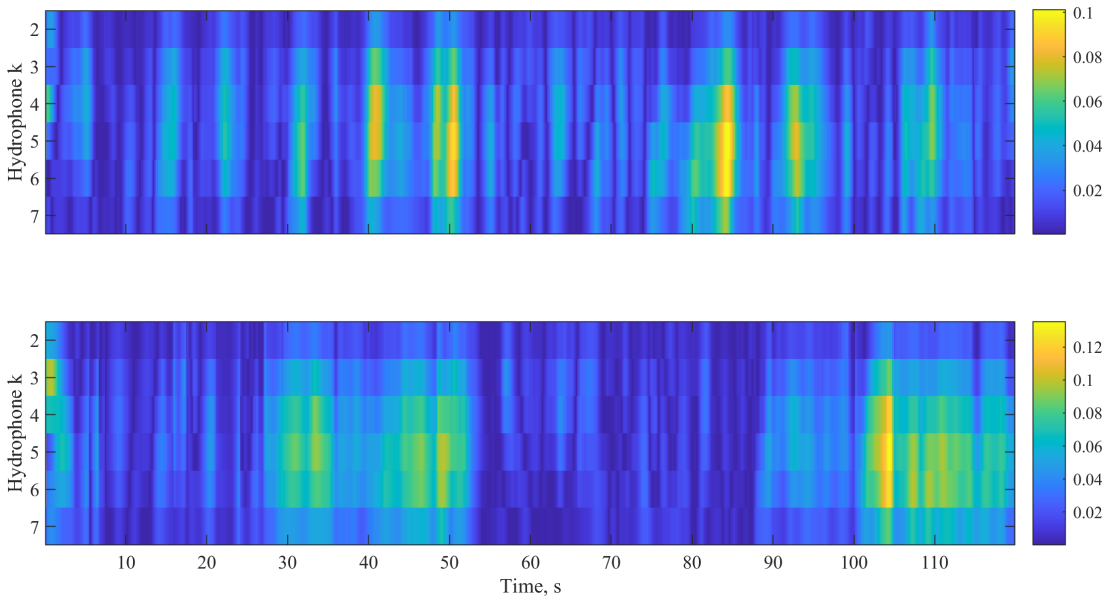

Figure 6-13: Array deviation in m from a straight line in (x, y) (top) and (x, z) (bottom) for Configuration 4

Table 6.5: Beamforming result mean increase, dB

Frequency, Hz	Configuration			
	1	2	3	4
790	0.139	0.142	0.169	0.162
1540	0.140	0.161	0.120	0.163
1640	0.117	0.150	0.104	0.150
1740	0.084	0.130	0.068	0.157

also summarised in Table 6.5, which shows the mean increase in beamformer output across the dataset, and Table 6.6, which shows the maximum increase achieved.

6.4.2.3 Configuration 4 Examination

Figures 6-15 show a closer observation of the the configuration 4 estimate, with slices showing more detail for some of the more perturbed instances where the MUSIC spectrum increase is greatest. In the (x, y) plane, the results suggest that the array oscillates with a period of $2 - 3$ s, which could correspond to the waves that are propelling the boat. The perturbation of the array appears predominantly to bow with an amplitude of < 0.1m.

Flickbook The array shape estimation result for Configuration 4 is also shown as a flickbook in the bottom right-hand corner of the even numbered pages of this thesis.

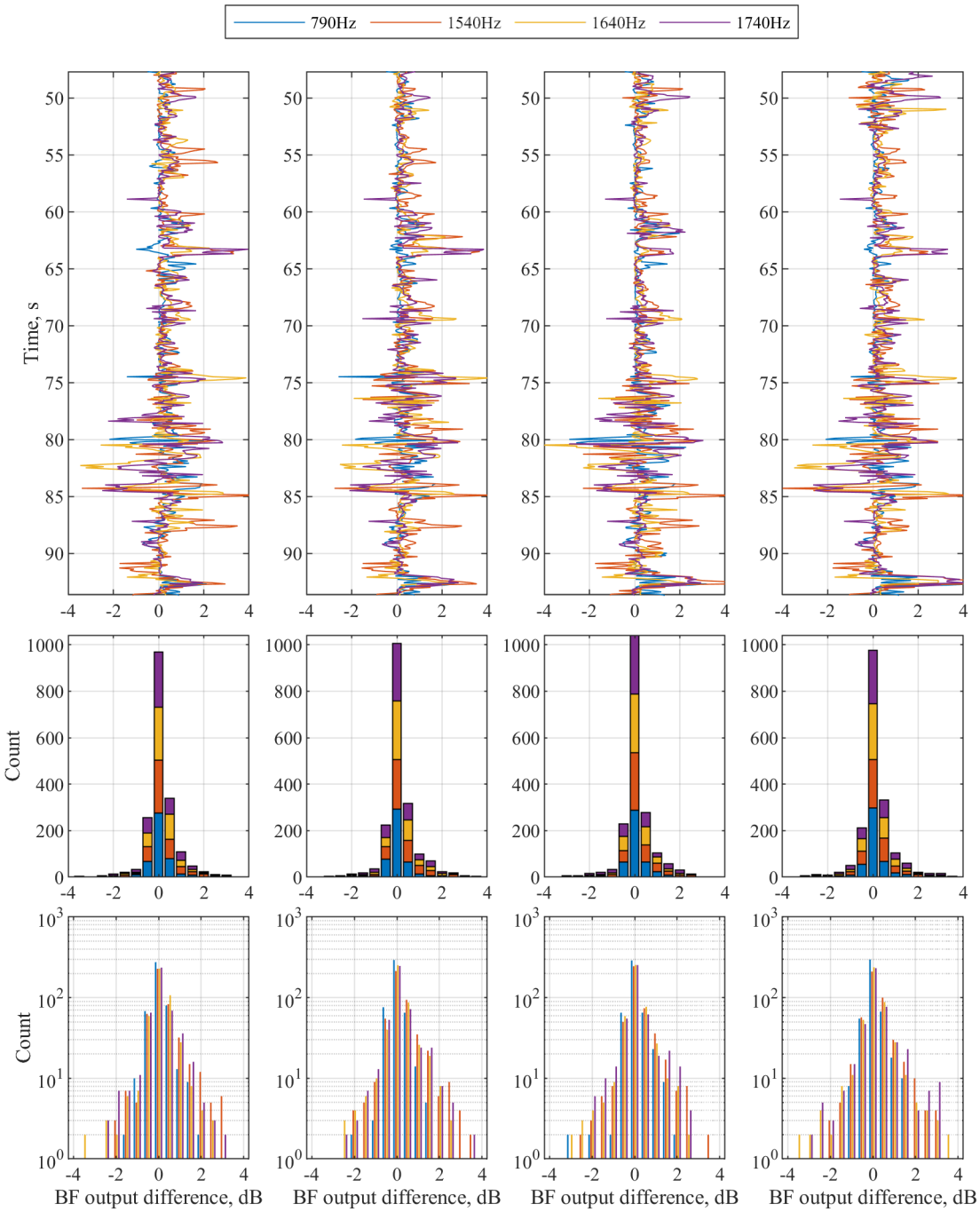

Figure 6-14: Difference between the maximum pre-compensation and post-compensation MUSIC spectrum value for (Far left) 1540Hz with direct path only, (middle left) all high frequencies with direct path only, (middle right) 1540Hz with direct and multipath and (far right) all high frequencies with direct and multipath. Middle and bottom figures are histograms of the number of time samples each beamformer output difference is observed.

Table 6.6: Beamforming result maximum increase, dB

Frequency, Hz	Configuration			
	1	2	3	4
790	3.11	2.56	3.47	4.48
1540	4.85	4.33	4.40	5.80
1640	3.88	4.14	2.80	3.71
1740	4.00	3.86	3.04	4.13

This has been downsampled by a factor of 4 to roughly match the true velocity of motion when used as a flickbook. There are randomly distributed fixed points included, moving at approximately the array's velocity to give some frame of reference to the motion of the array.

6.4.2.4 Beamformer Performance

Looking at the performance of each of the implemented beamforming techniques on experimental data, the improvement of both MVDR and MUSIC over the conventional beamformer is very evident, shown in Figure 6-16. The conventional beamforming resolution is too low to discern between the direct path and the multipath whereas the other beamformers have clearly distinct detections. The performance between MVDR and MUSIC is much closer, although the result from MUSIC is slightly clearer.

6.5 Summary

This chapter presents the validation of the simulation process described in Section 4 using experimental data. It was found to match consistently and accurately captures the effects of Doppler shift, complicated propagation patterns and realistic surface reflections.

Application of the array shape estimation method results in an increase of up to 5.8dB in the output of the MUSIC beamformer output spectrum. The results presented here suggest that in operation the array deployed from the Autonaut is perturbed into a mostly low order "bowing" shape with an amplitude of < 0.1m, which oscillates with a period of 2-3s. The deviation from a nominally straight array is found to be below the 0.046m target for sensor positional accuracy for roughly 80% of the period of high confidence, suggesting that a straight array assumption is mostly acceptable at this length of array. The tilt of the array, however, is found to introduce a multipath arrival which would not be present when operating with a horizontal array, which will complicate interpretation of the bearing estimation results.

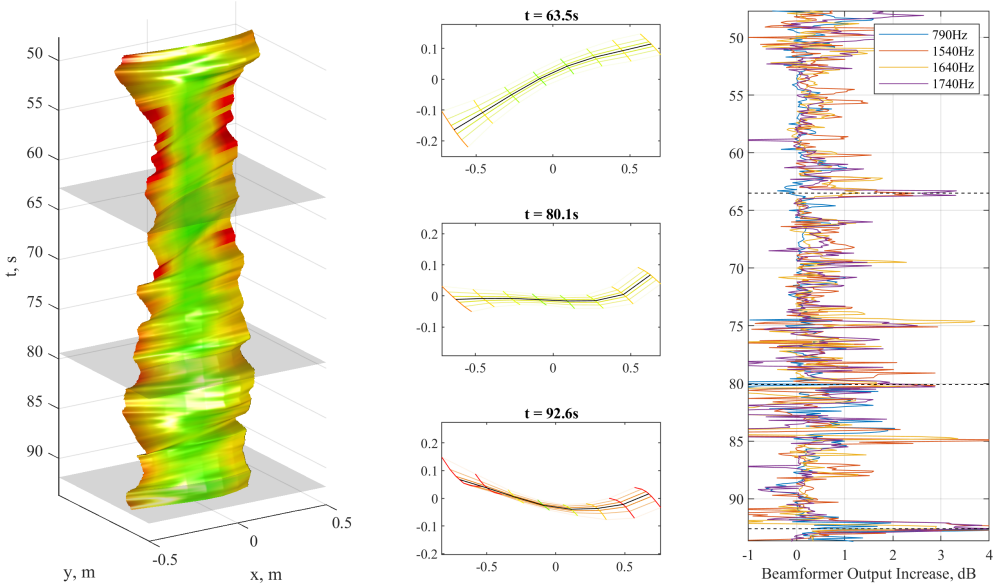

(a) xy

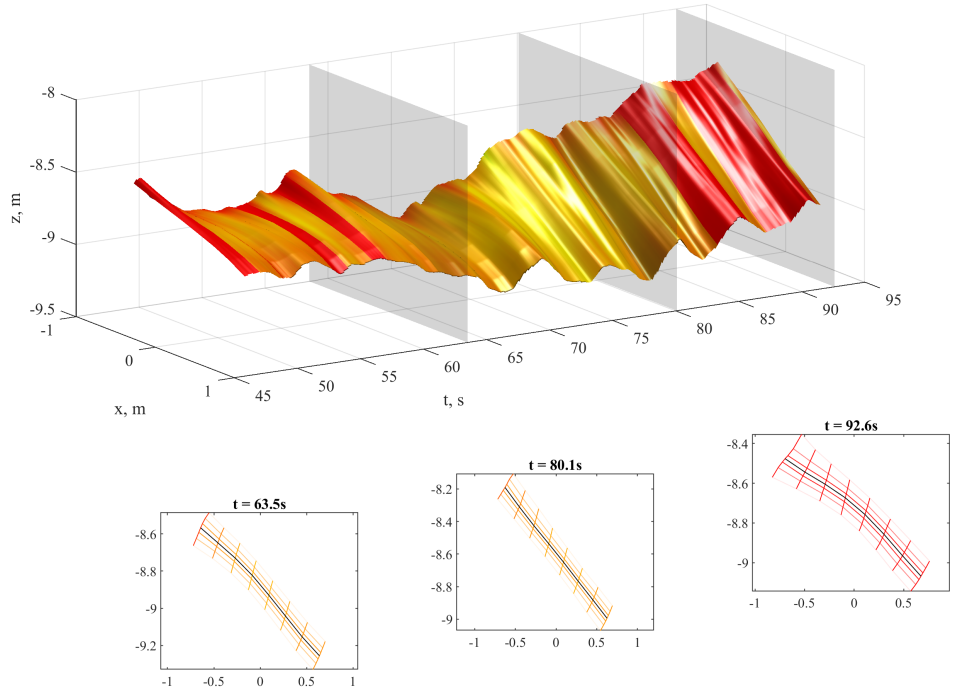

(b) xz

Figure 6-15: Zoomed in portion of array shape estimate in x and y for experimental data using all high frequencies with direct and multipath, with slices of certain sections that show some of the largest levels of perturbation

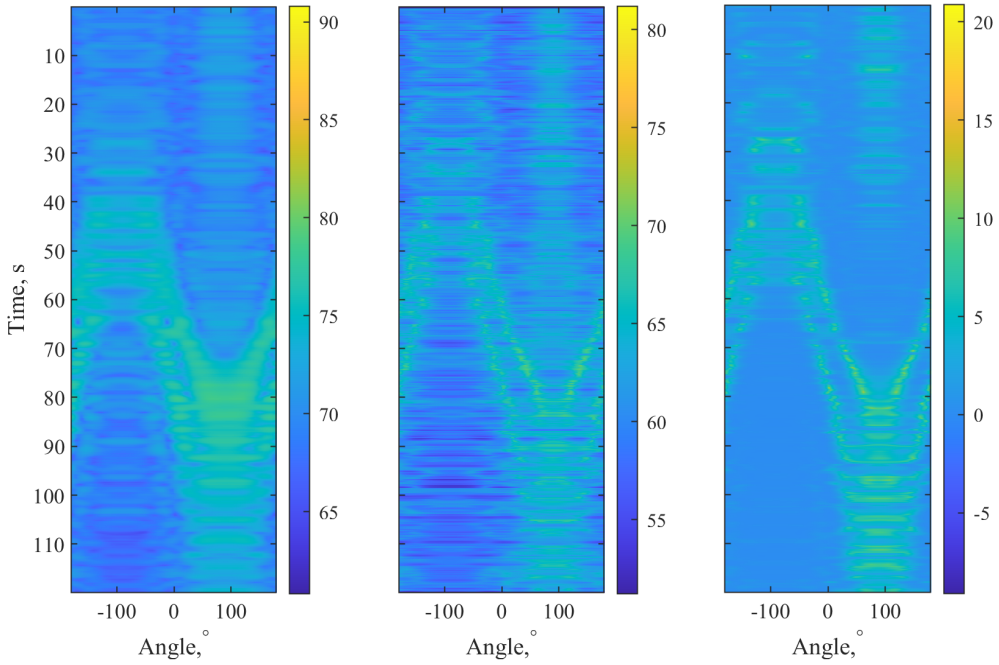

(a) Conventional (b) MVDR (c) MUSIC

Figure 6-16: Beamformer method comparison for the experimental data for 1540Hz. Colourbar limits are -10dB and +20dB of the median.

Chapter 7

Simulated Array Configuration Study

Acoustic data suitable for array calibration will not always be available in operation or in an experimental trial. There may be a lack of information regarding a sound source's location or perhaps the computational power available will not be adequate for accurate estimation. In the case of a highly perturbed array this could result in a significant decrease in the beamforming performance and inaccurate bearing detections. In these circumstances, the efficient use of non-acoustic sensors to measure the heading and tilt at key points of the array can alleviate this.

This chapter considers the configuration of non-acoustic sensors for an array deployed from a wave-propelled vehicle. This is carried out using simulated datasets with varying orders of perturbation and then estimating the certainty with which one could estimate the shape of the array using the method described in Section 5. The case presented here is limited to the array used in the experimental trial discussed in the previous chapter but acts as a demonstration of the capabilities of the method as a design analysis tool.

7.1 Simulated Datasets

Three datasets were simulated with 3 varied levels of perturbation:

- 1^{st} order (bow-shape), Figure 7-1a
- 2^{nd} order (S-shape), Figure 7-1b
- 3^{rd} order (M-shape), Figure 7-1c

These were selected based on the experimental array shape estimate results, which suggested mostly 1st and 2nd order perturbations for those conditions. These were simulated for an 8-hydrophone array with 0.23m spacing, the same as used in the experimental trial, and were varied sinusoidally from no deformation to a maximum perturbation amplitude of 0.1m, shown in Figure 7-1. As with previous analysis nodes are present on each of the hydrophones.

7.1.1 Array Configurations

The configuration of the non-acoustic instrumentation on the array was varied from a sparse distribution (tail sensor only), to a densely populated array (a CAPT module at each node). Each of these sensors had a error variance equal to that of the sensors on the physical array.

7.1.2 Results

The analysis is carried out using the array shape estimation particle filtering technique without incorporating any acoustic data, i.e. using only the readings from the 3-axis compasses and the depth sensors positioned at select nodes.

As in previous sections, results are displayed as coloured surface plots with green indicating ≤ 0.05m certainty in the estimate, i.e. $\lambda/10$ for the operating frequency of the array, which results in a $<$ 1dB reduction in conventional beamforming performance. Each of the results figures features a single time instance of the array at its most perturbed with the spread about the true position in the top row, and then surface plots for (x, y) and (x, z) in the next two rows.

7.2 Single Tail Non-Acoustic Sensor

Using just a single tail CAPT module, the performance of shape estimation is effectively limited by the rigidity of the array. Only the overall orientation of the array can be inferred which would cause a slight performance drop for a low order perturbation, as shown in Figure 7-2d, but has significantly reduced the performance in the 2nd and 3rd order perturbation cases. This is the configuration of the array

7.3 Head and Tail Non-Acoustic Sensors

A sensor at the head and the tail of the array offers improved performance in the case of 1st order perturbation, where the angle of the array between the two sensors varies

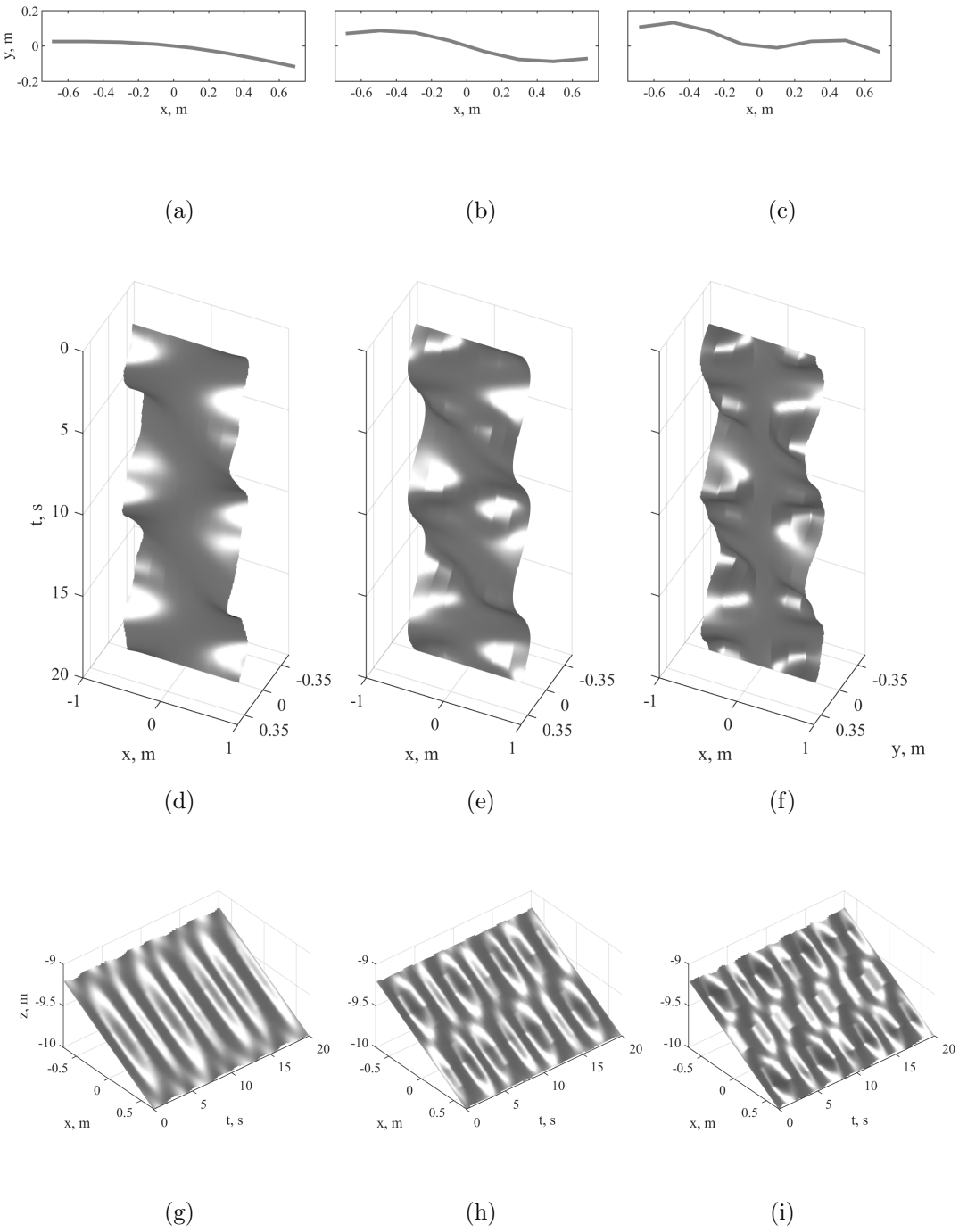

Figure 7-1: Ground truth of simulated data for each level of perturbation. (Left column) 1st order perturbation, (middle column) 2nd order perturbation and (right column) 3rd order perturbation. (a-c) a single time instance at the array's most perturbed, (d-f) xy data for each point in time and (g-i) xz data for each point in time.

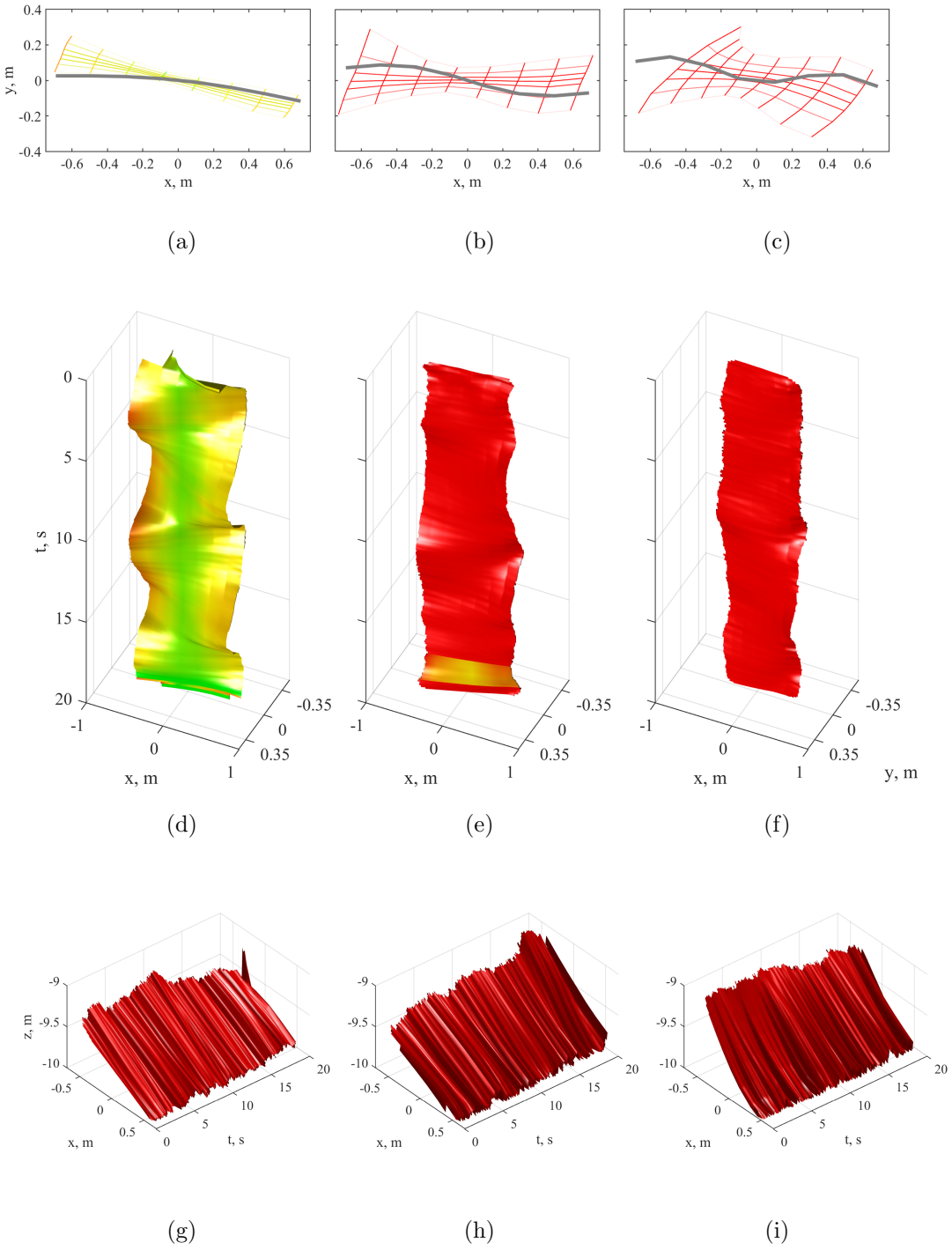

Figure 7-2: Array shape estimates using only tail sensor for datasets with each level of perturbation. (Left column) 1st order perturbation, (middle column) 2nd order perturbation and (right column) 3rd order perturbation. (a-c) a single time instance at the array's most perturbed state, (d-f) xy data for each point in time and (g-i) xz data for each point in time.

smoothly. Again, higher orders suffer in performance. This configuration would be sufficient for the majority of the experimental trial data used in the previous chapter.

7.4 Head, Middle and Tail Non-Acoustic Sensors

With an extra sensor placed in the midpoint of the array it is possible to accurately capture the shape of both 1^{st} and 2^{nd} order perturbations. While the spread of the estimate in the second order case is less than optimal, the shape and motion of the array can be seen to be fairly accurately captured by the mean estimate of the array shown in Figure 7-4e, suggesting that it would provide suitable performance for that case. For the experimental dataset, this configuration would ensure an accurate estimate throughout.

7.5 Densely Instrumented

As would be expected, fully instrumenting the array with CAPT modules at all nodes allows accurate estimation of the array for all cases and even provides decent performance in the xz plane. The accuracy of the estimate in the xz plane is limited by the depth sensor variance, hence it is not as accurate as in the xy plane. From a practical stand-point this configuration would be inefficient and expensive both financially and in terms of resources, as it would use more energy to run the sensors and more computer power to process them.

7.6 Discussion

Non-acoustic sensors use up resources and energy, and complicate the fabrication of an acoustic array so finding the minimum number required is an important step for designing an array. Arrays being towed by powered vessels can often operate with just a single heading sensor to give orientation information and then assume a straight array or interpolate between the vessel heading and the array heading. For a wave-propelled vessel, the chaotic nature of propulsion complicates this procedure. The experimental array estimate results from Section 6 suggest that the array is predominantly 1^{st} order perturbations with occasional 2^{nd} order, so for this 1.61m long array a head-middle-tail configuration would be optimal. It is likely that rougher sea conditions would increase the order of perturbations, so that would allow for an increased envelope of operating conditions.

The case considered here is a single instance of operation of an array of a certain

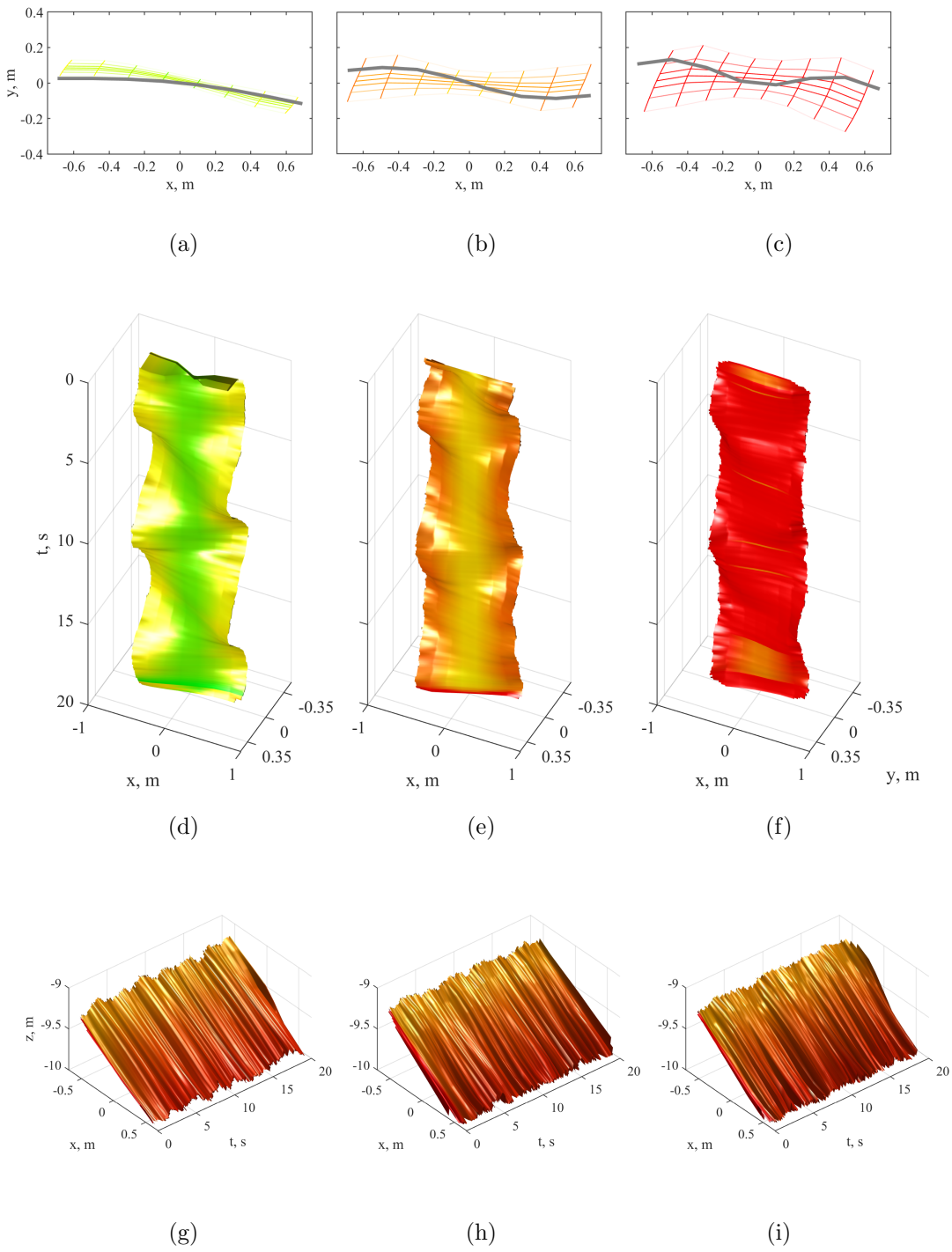

Figure 7-3: Array shape estimates using sensors at both the head and tail of the array for datasets with each level of perturbation. (Left column) 1st order perturbation, (middle column) 2nd order perturbation and (right column) 3rd order perturbation. (a-c) a single time instance at the array's most perturbed state, (d-f) xy data for each point in time and (g-i) xz data for each point in time.

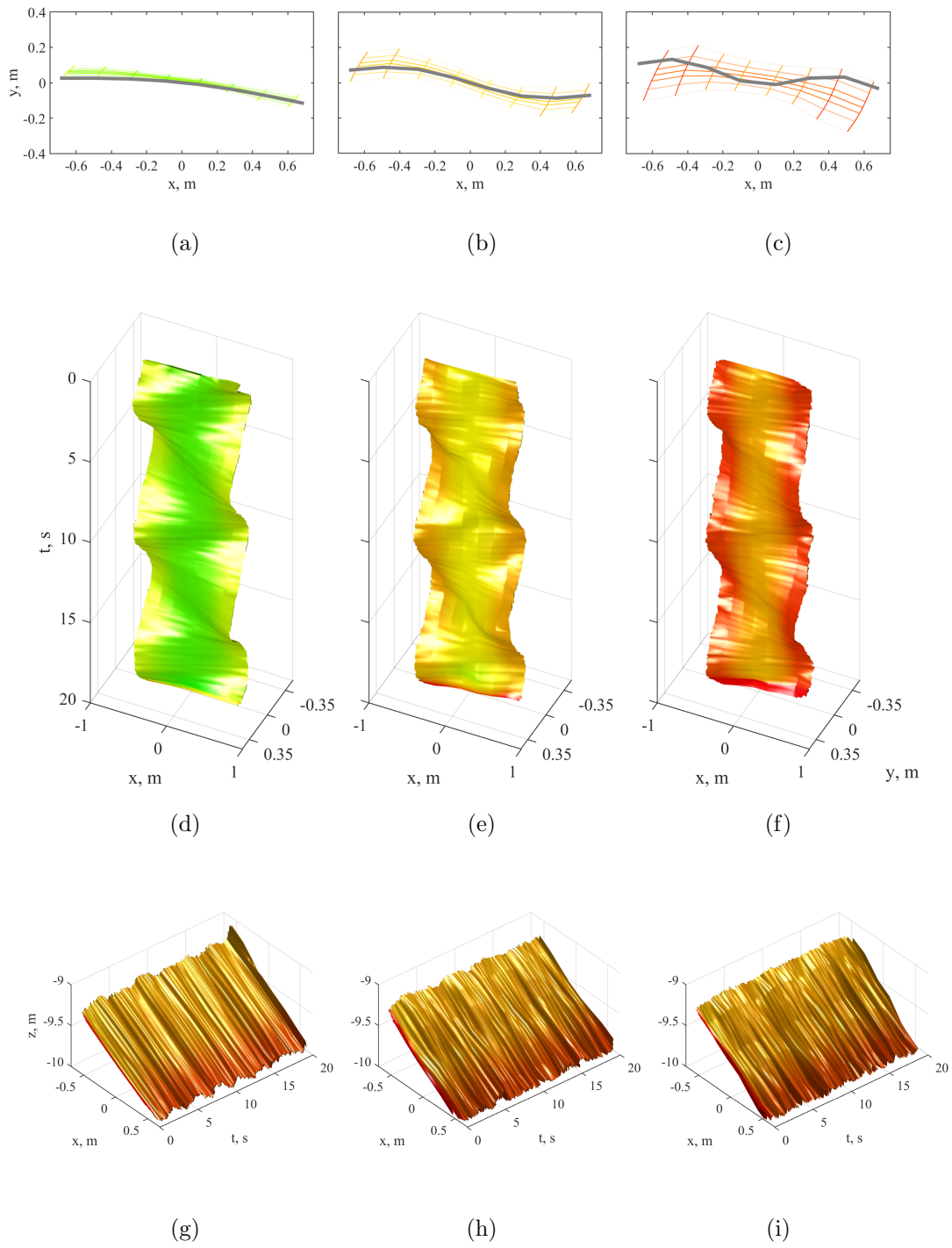

Figure 7-4: Array shape estimates using sensors at the head, middle and tail of the array for datasets with each level of perturbation. (Left column) 1st order perturbation, (middle column) 2nd order perturbation and (right column) 3rd order perturbation. (a-c) a single time instance at the array's most perturbed state, (d-f) xy data for each point in time and (g-i) xz data for each point in time.

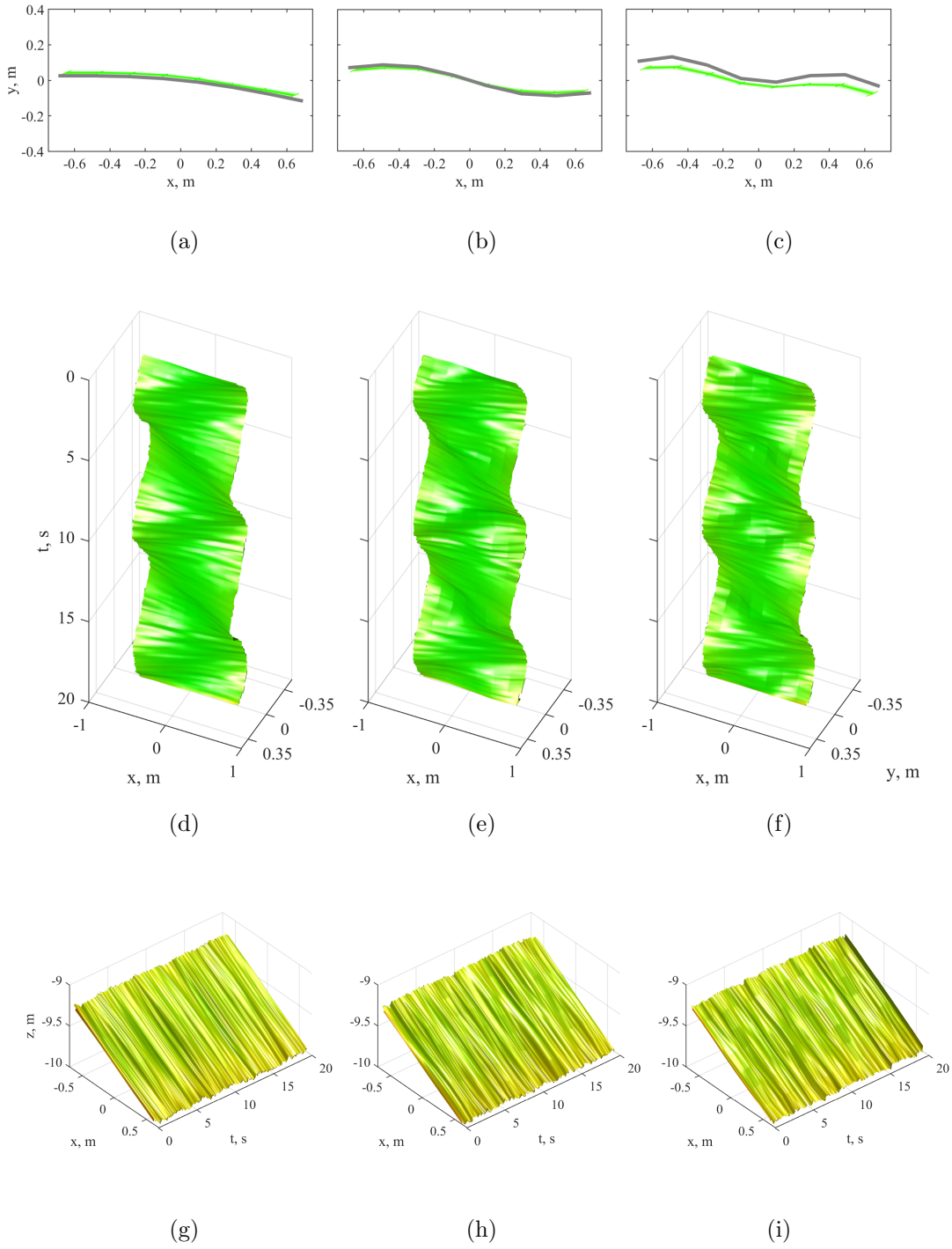

Figure 7-5: Array shape estimates using sensors at every node along the array for datasets with each level of perturbation. (Left column) 1st order perturbation, (middle column) 2nd order perturbation and (right column) 3rd order perturbation. (a-c) a single time instance at the array's most perturbed state, (d-f) xy data for each point in time and (g-i) xz data for each point in time.

length. Conceivably, in a more rough sea state the order of perturbation could be higher than that of the UW '16 trial. Furthermore, a longer array would theoretically present further challenges to shape estimation, as the level of perturbation increases with length. This methodology can be used as a tool to aid the design of such an array, allowing it to operate as efficiently and effectively as possible.

Chapter 8

Conclusions

This research presents the first investigation into the use of passive acoustic bearing estimation techniques from a towed hydrophone array deployed from an AutoNaut USV. It has been demonstrated that beamforming techniques can successfully be applied to acoustic data gathered from such a vessel, allowing bearing estimation to a sound source of interest.

A simulation process was developed for generating the received acoustic data from multiple moving sound sources on an array with a temporally varying shape. This utilised a selection of propagation models and included undulating surface reflections and a spectrally varying noise profile. The output data was validated with experimental data, showing that it accurately captured the effects of Doppler shift, the interference patterns from multiple arrivals and the propagation path of surface-reflected multipath rays.

In order to investigate the performance of a towed array in operation from the AutoNaut, an array shape estimation algorithm was developed, specifically aiming to address the associated challenges. This was based on partitioned recursive Bayesian estimation and fused all the available data from the non-acoustic and acoustic sensors into a 3D estimate of the array shape with bounds on the confidence of the estimate. This was validated using simulated data with varying configurations.

The experimental data from the Unmanned Warrior '16 trial was used as a case study to investigate the performance of the towed array in operation. Various beamforming algorithms were demonstrated successfully on the acoustic data, with the detection results matching the expected bearings. Further investigation into the motion of the array using the shape estimation algorithm suggested that the array was oscillating at a and periodically deforming into a bowed shape with a typical amplitude of less than 0.1m. When compensated for this resulted in an increase of up to 5.8dB in

the output spectrum of the MUSIC bearing estimation algorithm. The results suggest that for an array of this length in these operating conditions the assumption of straight array is sufficient for bearing estimation, without a significant drop in performance. However, the tilt on the array was found to introduce a surface-reflected multipath detection in the beamformer output spectrum which would not have been present in horizontal operation. This could pose a challenge to interpretation of the detection results.

Finally, the use of the array shape estimation algorithm as a tool for array design was demonstrated using simulated data to decide the optimal configuration of non-acoustic sensors for shape estimation. Based on the results of the experimental data, the optimal configuration for an array of that length would be non-acoustic sensors at the head, middle and tail of the array. This could be necessary in rougher wave conditions as the array shape is likely to be perturbed into a higher order shape with a higher amplitude.

8.1 Recommendations and Future Work

The following are suggestions of future work that are either in the process of being investigated or would be of interest following on from this work:

Further experimental investigation Although a conclusion of this work is that the straight array assumption is sufficient in the studied experimental case, the work presented here has implications for operation in a rougher sea state or with the use of a longer array. Further research is needed into the array shape over a broader range of operating conditions and array lengths.

Real-time in-situ operation One of the advantages of an autonomous surface vessel is the connectivity with operators on a support vessel or on shore, so a follow-on to this work would be to develop real-time in-situ operation of beamforming, detection and shape estimation.

Ambient-noise array shape estimation The versatile nature of the array shape estimation algorithm allows inclusion of any available information in the operating scenario. An interesting untapped source could be the use of ambient noise in the estimator to allow for shape estimation in circumstances where there are no sources of opportunity present.

The work presented in this thesis together with these recommendations represent a significant step towards fully realising the potential of the passive acoustic monitoring capabilities of the AutoNaut USV.

Bibliography

[1] D. Bacon and D. Jarvis, "The speed and attenuation of sound 2.4.1 - National Physical Laboratory." http://www.kayelaby.npl.co.uk/general_physics/2_4/2_4_1.html, 2017.

[2] A. Frantzis, "Does acoustic testing strand whales?," *Nature*, vol. 392, p. 29, mar 1998.

[3] E. C. M. Parsons, "Impacts of Navy Sonar on Whales and Dolphins: Now beyond a Smoking Gun?," *Frontiers in Marine Science*, vol. 4, p. 295, sep 2017.

[4] D. L. Evans and G. R. England, "Joint Interim Report Bahamas Marine Mammal Stranding Event of 15-16 March 2000," *Environment*, no. March 2000, p. 66, 2001.

[5] R. Filadelfo, J. Mintz, E. Michlovich, A. D'Amico, P. L. Tyack, and D. R. Ketten, "Correlating Military Sonar Use with Beaked Whale Mass Strandings: What Do the Historical Data Show?," *Aquatic Mammals*, vol. 35, pp. 435–444, dec 2009.

[6] A. Fernández, M. Arbelo, and V. Martín, "Whales: No mass strandings since sonar ban," *Nature*, vol. 497, p. 317, may 2013.

[7] V. Morell, "U.S. Navy to limit sonar testing to protect whales," *Science*, sep 2015.

[8] L. Fillinger, A. J. Hunter, M. Zampolli, and M. C. Clarijs, "Passive acoustic detection of closed-circuit underwater breathing apparatus in an operational port environment.," *The Journal of the Acoustical Society of America*, vol. 132, oct 2012.

[9] I. R. Urazghildiiev and C. W. Clark, "Comparative analysis of localization algorithms with application to passive acoustic monitoring," *The Journal of the Acoustical Society of America*, vol. 134, p. 4418, dec 2013.

[10] J. Gebbie, M. Siderius, and J. S. Allen, "A two-hydrophone range and bearing localization algorithm with performance analysis," *The Journal of the Acoustical Society of America*, vol. 137, no. 3, pp. 1586–1597, 2015.

[11] C. R. Greene, M. W. McLennan, R. G. Norman, T. L. McDonald, R. S. Jakubczak, and W. J. Richardson, "Directional frequency and recording (DIFAR) sensors in seafloor recorders to locate calling bowhead whales during their fall migration," *The Journal of the Acoustical Society of America*, vol. 116, no. 2, pp. 799–813, 2004.

[12] "Products — Sonobuoy TechSystems." https://www.sonobuoytechsystems.com/products/.

[13] S. G. Lemon, "Towed-array history, 1917-2003," *IEEE Journal of Oceanic Engineering*, vol. 29, no. 2, pp. 365–373, 2004.

[14] J. D. Holmes, W. M. Carey, J. F. Lynch, A. E. Newhall, and A. Kukulya, "An autonomous underwater vehicle towed array for ocean acoustic measurements and inversions," in *Oceans 2005 - Europe*, vol. 2, pp. 1058–1061, 2005.

[15] V. Pallayil, M. A. Chitre, and P. D. Deshpande, "A digital thin line towed array for small autonomous underwater platforms," in *Oceans Conference Record (IEEE)*, 2007.

[16] T. R. Stottlemyer, R. C. Mewer, and M. A. Maugle, "Towed array deployment system for unmanned surface vehicles." https://www.google.com/patents/US20100275831, 2010.

[17] P. Johnston, "Passive Acoustic Monitoring By USV: Wave-propelled AutoNaut Comes of Age," *Ocean News & Technology EDITORIAL*, 2017.

[18] P. Ridden, "Autonomous boat gets around under wave power." https://newatlas.com/autonaut-autonomous-unmanned-surface-vessel/53949/.

[19] "University Defence Research Collaboration in Signal Processing , Phase 3 Application Theme : " Acoustic Signal and Information Processing in the Underwater Environment " Call for proposals Overview," 2019.

[20] S. W. Rienstra and A. Hirschberg, *An Introduction to Acoustics*. Eindhoven University of Technology, 2004.

[21] C. E. Shannon, "Communication in the Presence of Noise," *Proceedings of the IRE*, vol. 37, no. 1, pp. 10–21, 1949.

[22] "Watkins Marine Mammal Sound Database, Woods Hole Oceanographic Institution.." https://cis.whoi.edu/science/B/whalesounds/index.cfm, 2017.

[23] P. J. Loughlin and L. Cohen, "The uncertainty principle: Global, local, or both?," *IEEE Transactions on Signal Processing*, vol. 52, no. 5, pp. 1218–1227, 2004.

[24] M. A. Ainslie, "The Sonar Equations," in *Principles of Sonar Performance Modelling*, pp. 1–4, Springer Berlin Heidelberg, 2010.

[25] C. A. M. Van Moll, M. A. Ainslie, and R. Van Vossen, "A Simple and accurate formula for the absorption of sound in seawater," *IEEE Journal of Oceanic Engineering*, vol. 34, no. 4, pp. 610–616, 2009.

[26] A. C. Duxbury, F. T. Mackenzie, and R. H. Byrne, "Seawater - Acoustic properties." https://www.britannica.com/science/seawater/Acoustic-properties, 2017.

[27] M. A. Ainslie, "Essential background," in *Principles of Sonar Performance Modelling*, pp. 27–52, Berlin, Heidelberg: Springer Berlin Heidelberg, 2010.

[28] M. A. Ainslie, "Sonar oceanography," in *Principles of Sonar Performance Modelling*, ch. 4, p. 145, Springer Berlin Heidelberg, 2010.

[29] M. Ainslie and M. A. Ainslie, "Propagation of underwater sound," in *Principles of Sonar Performance Modelling*, pp. 439–512, 2009.

[30] W. M. Carey, "Lloyd's Mirror—Image Interference Effects," *Acoustics Today*, vol. 5, no. 2, pp. 14–20, 2009.

[31] V. Meyer and C. Audoly, "A comparison between experiments and simulation for shallow water short range acoustic propagation," in *24th International Congress on Sound and Vibration, ICSV 2017*, 2017.

[32] L. Wang, K. Heaney, T. Pangerc, P. Theobald, S. Robinson, and M. Ainslie, "Review of Underwater Acoustic Propagation Models," *NPL Report*, no. October 2014, 2014.

[33] L. Dong and H. Dong, "Bellhop – A modeling approach to Sound propagation in the ocean," *Proceedings of the 36th Scandinavian Symposium on Physical Acoustics*, pp. 1–4, 2014.

[34] J. M. Hovem and H. Dong, "Understanding ocean acoustics by eigenray analysis," *Journal of Marine Science and Engineering*, vol. 7, p. 118, apr 2019.

[35] M. B. Porter, "The BELLHOP Manual and User's Guide (Preliminary Draft)," pp. 1–57, 2011.

[36] E. T. Kusel and M. Siderius, "Comparison of Propagation Models for the Characterization of Sound Pressure Fields," *IEEE Journal of Oceanic Engineering*, vol. 44, pp. 598–610, jul 2019.

[37] C. L. Pekeris, "Theory of propagation of explosive sound in shallow water," *Memoir of the Geological Society of America*, vol. 27, pp. 1–116, 1948.

[38] G. V. Frisk, "Noiseonomics: The relationship between ambient noise levels in the sea and global economic trends," *Scientific Reports*, vol. 2, pp. 1–4, jun 2012.

[39] J. A. Hildebrand, "Anthropogenic and natural sources of ambient noise in the ocean," *Marine Ecology Progress Series*, vol. 395, pp. 5–20, 2009.

[40] J. A. Scrimger, "Underwater noise caused by precipitation," *Nature*, vol. 318, no. 6047, pp. 647–649, 1985.

[41] W. W. L. Au and K. Banks, "The acoustics of snapping shrimps," *The Journal of the Acoustical Society of America*, vol. 101, no. 5, pp. 3032–3032, 1997.

[42] D. H. Thomson and J. W. Richardson, "Marine Mammal Sounds," in *Marine Mammals and Noise*, ch. 7, pp. 159–204, Academic Press, 1995.

[43] "What are common underwater sounds? – Discovery of Sound in the Sea." https://dosits.org/science/sounds-in-the-sea/what-are-common-underwater-sounds/.

[44] G. M. Wenz, "Acoustic Ambient Noise in the Ocean: Spectra and Sources," *The Journal of the Acoustical Society of America*, vol. 34, no. 12, pp. 1936–1956, 1962.

[45] S. U. Pillai, "Detection of Multiple Signals," in *Array Signal Processing* (C. S. Burrus, ed.), ch. 2, pp. 8–107, Springer New York, 1989.

[46] H. Krim and M. Viberg, "Two decades of array signal processing research: the parametric approach," *IEEE Signal Processing Magazine*, vol. 13, pp. 67–94, jul 1996.

[47] N. Anwar Baig and M. Bilal Malik, "Comparison of Direction of Arrival (DOA) Estimation Techniques for Closely Spaced Targets," *International Journal of Future Computer and Communication*, vol. 2, no. 6, pp. 654–659, 2013.

[48] V. Krishnaveni, T. Kesavamurthy, and Aparna.B, "Beamforming for Direction-of-Arrival (DOA) Estimation-A Survey," *International Journal of Computer Applications*, vol. 61, no. 11, pp. 975–8887, 2013.

[49] S. N. Bhuiya, F. Islam, and M. A. Matin, "Analysis of Direction of Arrival Techniques using Uniform Linear Array," *International Journal of Computer Theory and Engineering*, vol. 4, no. 6, pp. 4–7, 2012.

[50] R. Kumar Dhull and S. Kumar Dhull, "Review on Acoustic Source Localization Techniques," *European Journal of Advances in Engineering and Technology*, vol. 2, no. 9, pp. 72–77, 2015.

[51] C. H. Knapp and G. C. Carter, "The Generalized Correlation Method for Estimation of Time Delay," *IEEE Transactions on Acoustics, Speech, and Signal Processing*, vol. 24, pp. 320–327, aug 1976.

[52] G. C. Carter, "Coherence and time delay estimation," *Proceedings of the IEEE*, vol. 75, no. 2, pp. 236–255, 1987.

[53] A. Sutin, B. Bunin, A. Sedunov, N. Sedunov, L. Fillinger, M. Tsionskiy, and M. Bruno, "Stevens passive acoustic system for underwater surveillance," in *2010 International Waterside Security Conference, WSS 2010*, pp. 1–6, IEEE, nov 2010.

[54] B. Patel, S. R. K. Vadali, S. Nandy, and S. N. Shome, "On methods to improve time delay estimation for underwater acoustic source localization," *Indian Journal of Geo-Marine Sciences*, vol. 44, no. 2, pp. 237–244, 2015.

[55] M. Gassmann, S. M. Wiggins, and J. A. Hildebrand, "Three-dimensional tracking of Cuvier's beaked whales' echolocation sounds using nested hydrophone arrays," *The Journal of the Acoustical Society of America*, oct 2015.

[56] C. O. Tiemann, M. B. Porter, and L. N. Frazer, "Localization of marine mammals near Hawaii using an acoustic propagation model," *The Journal of the Acoustical Society of America*, vol. 115, no. 6, pp. 2834–2843, 2004.

[57] C. W. Clark, "A real-time direction finding device for determining the bearing to the underwater sounds of Southern Right Whales, Eubalaena australis," *The Journal of the Acoustical Society of America*, vol. 68, no. 2, pp. 508–511, 1980.

[58] P. D. Welch, "The Use of Fast Fourier Transform for the Estimation of Power Spectra: A Method Based on Time Averaging Over Short, Modified Peri-

odograms," *IEEE Transactions on Audio and Electroacoustics*, vol. 15, no. 2, pp. 70–73, 1967.

[59] C. Ocker and W. Pannert, "Calculation of the cross spectral matrix with Daniell's method and application to acoustical beamforming," *Applied Acoustics*, vol. 120, pp. 59–69, may 2017.

[60] H. L. Van Trees, *Optimum Array Processing: Part IV of Detection, Estimation, and Modulation Theory*. Detection, Estimation, and Modulation Theory, Wiley, 2004.

[61] M. S. Bartlett, "Periodogram analysis and continuous spectra," *Biometrika*, vol. 37, pp. 1–16, jun 1950.

[62] J. Capon, "High-resolution frequency-wavenumber spectrum analysis," *Proceedings of the IEEE*, vol. 57, no. 8, pp. 1408–1418, 1969.

[63] S. A. Vorobyov, "Principles of minimum variance robust adaptive beamforming design," *Signal Processing*, vol. 93, no. 12, pp. 3264–3277, 2013.

[64] M. Colin, J. Groen, and B. Quesson, "Experimental comparison of bearing estimation techniques for short passive towed sonar arrays," in *Ocean '04 - MTS/IEEE Techno-Ocean '04: Bridges across the Oceans - Conference Proceedings*, vol. 2, pp. 608–612, IEEE, 2004.

[65] J. Gebbie, M. Siderius, P. L. Nielsen, and J. Miller, "Passive localization of noise-producing targets using a compact volumetric array.," *The Journal of the Acoustical Society of America*, vol. 136, no. 1, pp. 80–9, 2014.

[66] F. Wang, J. Wang, and X. Song, "An Improved Diagonal Loading Algorithm," in *Advances in Electronic Commerce, Web Application and Communication*, pp. 45–52, Springer Berlin Heidelberg, 2012.

[67] J. Li, P. Stoica, and Z. Wang, "On robust Capon beamforming and diagonal loading," *IEEE Transactions on Signal Processing*, vol. 51, pp. 1702–1715, jul 2003.

[68] Ning Ma and Joo Thiam Goh, "Efficient method to determine diagonal loading value," *2003 IEEE International Conference on Acoustics, Speech, and Signal Processing, 2003. Proceedings. (ICASSP '03).*, vol. 5, pp. V–341–4, 2003.

[69] K. J. Raghunath and V. U. Reddy, "Finite Data Performance Analysis of MVDR Beamformer with and without Spatial Smoothing," *IEEE Transactions on Signal Processing*, vol. 40, no. 11, pp. 2726–2736, 1992.

[70] C. Pan, J. Chen, and J. Benesty, "On the noise reduction performance of the MVDR beamformer innoisy and reverberant environments," in *ICASSP, IEEE International Conference on Acoustics, Speech and Signal Processing - Proceedings*, pp. 815–819, IEEE, may 2014.

[71] R. Schmidt, "Multiple Emitter Location and Signal Parameter Estimation," *IEEE Transactions on Antennas and Propagation*, vol. 34, pp. 276–280, mar 1986.

[72] A. Swindlehurst and T. Kailath, "A Performance analysis of subspce-based method in the presence of model errors, part I: the MUSIC algorithm," *Signal Processing, IEEE Transactions on*, vol. 40, no. 7, pp. 1758–1774, 1992.

[73] A. Vesa, "Direction of Arrival Estimation using MUSIC and Root – MUSIC Algorithm," *18th Telecommunications forum TELFOR 2010*, no. 7, pp. 582–585, 2010.

[74] M. Kaveh and A. J. Barabell, "The statistical performance of the music and the minimum-norm algorithms in resolving plane waves in noise," *IEEE Transactions on Acoustics, Speech, and Signal Processing*, vol. 34, no. 2, pp. 331–341, 1986.

[75] F. Li and R. J. Vaccaro, "Analysis Of Min-Norm And Music With Arbitrary Array Geometry," *IEEE Transactions on Aerospace and Electronic Systems*, vol. 26, no. 6, pp. 976–985, 1990.

[76] R. Roy and T. Kailath, "ESPRIT - Estimation of Signal Parameters Via Rotational Invariance Techniques," *IEEE Transactions on Acoustics, Speech, and Signal Processing*, vol. 37, pp. 984–995, jul 1989.

[77] C. Qian, L. Huang, and H. C. So, "Computationally efficient ESPRIT algorithm for direction-of-arrival estimation based on Nyström method," *Signal Processing*, vol. 94, no. 1, pp. 74–80, 2014.

[78] H. Krim and J. Cozzens, "A data-based enumeration technique for fully correlated signals," *IEEE Transactions on Signal Processing*, vol. 42, pp. 1662–1668, jul 1994.

[79] J. H. Cozzens and M. J. Sousa, "Source Enumeration in a Correlated Signal Environment," *IEEE Transactions on Signal Processing*, vol. 42, no. 2, pp. 304–317, 1994.

[80] W. Cheng, Z. Zhang, H. Cao, Z. He, and G. Zhu, "A comparative study of information-based source number estimation methods and experimental validations on mechanical systems," *Sensors (Switzerland)*, vol. 14, pp. 7625–7646, apr 2014.

[81] H. Asadi and B. Seyfe, "Signal enumeration in Gaussian and non-Gaussian noise using entropy estimation of eigenvalues," *Digital Signal Processing: A Review Journal*, vol. 78, pp. 163–174, jul 2018.

[82] S. E. Dosso and B. J. Sotirin, "Optimal array element localization," *The Journal of the Acoustical Society of America*, vol. 106, no. 110, pp. 3445–3459, 1999.

[83] W. S. Hodgkiss, "The Effects of Array Shape Perturbation on Beamforming and Passive Ranging," *IEEE Journal of Oceanic Engineering*, vol. 8, no. 3, pp. 120–130, 1983.

[84] M. J. Hinich, "Bearing estimation using a perturbed linear array," *The Journal of the Acoustical Society of America*, vol. 61, no. 6, p. 1540, 1977.

[85] P. Gerstoft, W. S. Hodgkiss, W. A. Kuperman, H. Song, M. Siderius, and P. L. Nielsen, "Adaptive Beamforming of a Towed Array During a Turn," *IEEE Journal of Oceanic Engineering*, vol. 28, no. 1, pp. 44–54, 2003.

[86] J. L. Odom and J. L. Krolik, "Passive Towed Array Shape Estimation Using Heading and Acoustic Data," *IEEE Journal of Oceanic Engineering*, vol. 40, no. 2, pp. 465–474, 2015.

[87] Z. Zheng, T. C. Yang, P. Gerstoft, and X. Pan, "Joint towed array shape and direction of arrivals estimation using sparse Bayesian learning during maneuvering," *The Journal of the Acoustical Society of America*, vol. 147, no. 3, pp. 1738–1751, 2020.

[88] S. E. Dosso and M. Riedel, "Array element localization for towed marine seismic arrays," *The Journal of the Acoustical Society of America*, vol. 110, no. 2, p. 955, 2001.

[89] N. Convers Wyeth, "Methods of array element localization for a towed underwater acoustic array," *IEEE Journal of Oceanic Engineering*, vol. 19, no. 1, pp. 128–133, 1994.

[90] B. G. Ferguson, D. A. Gray, J. L. Riley, and J. K. Riley, "Comparison of sharpness and eigenvector methods for towed array shape estimation," *The Journal of the Acoustical Society of America*, vol. 91, no. 846, pp. 55081–1451, 1992.

[91] D. A. Gray, B. D. Anderson, and R. R. Bitmead, "Towed array shape estimation using kalman filters-theoretical models," *IEEE Journal of Oceanic Engineering*, vol. 18, no. 4, pp. 543–556, 1993.

[92] J. J. Smith, Y. H. Leung, and A. Cantoni, "The partitioned eigenvector method for towed array shape estimation," *IEEE Transactions on Signal Processing*, vol. 44, no. 9, pp. 2273–2283, 1996.

[93] M. Viberg and A. L. Swindlehurst, "A Bayesian Approach to Auto-Calibration for Parametric Array Signal Processing," *IEEE Transactions on Signal Processing*, vol. 42, no. 12, pp. 3495–3507, 1994.

[94] C. Li, J. Jiang, F. Duan, X. Wang, L. Ma, L. Bu, and Z. Sun, "Towed Array Shape Estimation Based on Single or Double Near-Field Calibrating Sources," *Circuits, Systems, and Signal Processing*, vol. 38, pp. 153–172, jan 2019.

[95] G. S. Egeland, "Array Shape Estimation," *OCEANS 82*, vol. Sept, no. 6, pp. 121–122, 1982.

[96] B. E. Howard and J. M. Syck, "Calculation of the Shape of a Towed Underwater Acoustic Array," *IEEE Journal of Oceanic Engineering*, vol. 17, no. 2, pp. 193–203, 1992.

[97] B. K. Newhall, J. W. Jenkins, and J. E. G. Dietz, "Improved estimation of the shape of towed sonar arrays," *IEEE Instrumentation and Measurement Technology Conference*, vol. 2, no. May, pp. 873–876, 2004.

[98] R. Kennedy and E. Strahan, "A linear theory of traverse cable dynamics at low frequencies," tech. rep., NUSC Tech. Rep. 6463, 1981.

[99] M. P. Paidoussis, "Dynamics of flexible slender cylinders in axial flow Part 1. Theory," *Journal of Fluid Mechanics*, vol. 26, no. 4, pp. 717–736, 1966.

[100] R. M. Kennedy, "Crosstrack Dynamics of a Long Cable Towed in the Ocean.," in *Oceans Conference Record (IEEE)*, vol. 2, pp. 966–970, IEEE, 1981.

[101] F. Lu, E. Milios, S. Stergiopoulos, and A. Dhanantwari, "New towed-array shape-estimation scheme for real-time sonar systems," *IEEE Journal of Oceanic Engineering*, vol. 28, pp. 552–563, jul 2003.

[102] C. Peng and X. Zhang, "A dynamic depth estimation method for towed optical fiber hydrophone array," *The Journal of the Acoustical Society of America*, vol. 143, pp. EL399–EL404, may 2018.

[103] D. E. Wahl, "Towed array shape estimation using frequency-wavenumber data," *IEEE Journal of Oceanic Engineering*, vol. 18, no. 4, pp. 582–590, 1993.

[104] H. Bucker, "Beamforming a Towed Line Array of unknown shape," *Journal of Acoustical Society of America*, vol. 63, no. 5, pp. 1451–1454, 1978.

[105] B. G. Ferguson, "Sharpness applied to the adaptive beamforming of acoustic data from a towed array of unknown shape," *The Journal of the Acoustical Society of America*, vol. 88, pp. 2695–2701, dec 1990.

[106] Y. Rockah and P. M. Schultheiss, "Array Shape Calibration Using Sources in Unknown Locations-Part I: Far-Field Sources," *IEEE Transactions on Acoustics, Speech, and Signal Processing*, vol. 35, no. 6, pp. 724–735, 1987.

[107] A. J. Weiss and B. Friedlander, "Array Shape Calibration Using Sources in Unknown Locations - A Maximum Likelihood Approach," *IEEE Trans. ASSP*, vol. 37, no. 12, pp. 1958–1966, 1989.

[108] B. Ng and a. Nehorai, "Active array sensor location calibration," *IEEE International Conference on Acoustics, Speech, and Signal Processing*, vol. 4, pp. 21–24 vol.4, 1993.

[109] B. C. Ng and C. M. S. See, "Sensor-Array Calibration Using a Maximum-Likelihood Approach," *IEEE Transaction on Antennas and Propagation*, vol. 44, no. 6, 1996.

[110] S. E. Dosso, M. R. Fallat, B. J. Sotirin, and J. L. Newton, "Array element localization for horizontal arrays via Occam's inversion," *The Journal of the Acoustical Society of America*, vol. 106, no. 6, pp. 3445–3459, 1998.

[111] F. Arrichiello, G. Antonelli, and E. Kelholt, "Shape estimate of a streamer of hydrophones towed by an Autonomous Underwater Vehicle," *IFAC-PapersOnLine*, vol. 49, no. 23, pp. 181–186, 2016.

[112] N. Zou, Z. Jia, J. Fu, J. Feng, and M. Liu, "A geometric calibration method of hydrophone array based on maximum likelihood estimation with sources in near field," *Journal of Marine Science and Engineering*, vol. 8, no. 9, pp. 1–21, 2020.

[113] B. C. Ng and S. Wee, "Array shape calibration using sources in known locations," *Singapore ICCS/ISITA '92. 'Communications on the Move'*, pp. 836–840 vol.2, 1992.

[114] H. Y. Park, K. M. Kim, H. W. Kang, D. H. Youn, and C. Lee, "A simplified subspace fitting method for estimating shape of a towed array," *IEEE Journal of Oceanic Engineering*, vol. 33, no. 2, pp. 215–223, 2008.

[115] H.-y. Park, C. Lee, H.-g. Kang, and D.-h. Youn, "Generalization of the Subspace-Based Array Shape Estimations," *IEEE Journal of Oceanic Engineering*, vol. 29, no. 3, pp. 847–856, 2004.

[116] N. L. Owsley and G. R. Swope, "Time delay estimation in a sensor array," *Underwater Acoustics and Signal Processing*, vol. 1, no. 1, pp. 421–432, 1981.

[117] A. J. Weiss and B. Friedlander, "Array shape calibration using eigenstructure methods," in *Conference Record - Asilomar Conference on Circuits, Systems & Computers*, vol. 2, pp. 925–929, Maple Press, Inc, 1989.

[118] J. J. Smith, Y. H. Leung, and A. Cantoni, "Broadband eigenvector methods for towed array shape estimation with a single source," *ICASSP, IEEE International Conference on Acoustics, Speech and Signal Processing - Proceedings*, vol. 6, pp. 3193–3196, 1996.

[119] B. G. Quinn, R. F. Barrett, J. Kootsookos, and S. J. Searle, "The estimation of the shape of an array using a Hidden Markov Model," *IEEE Journal of Oceanic Engineering*, vol. 18, no. 4, pp. 557–564, 1993.

[120] M. G. Morley, S. E. Dosso, and N. R. Chapman, "Array element localization using ship noise.," *The Journal of the Acoustical Society of America*, vol. 125, no. 3, pp. 1403–9, 2009.

[121] L. Brooks and P. Gerstoft, "Hydrophone self-localisation using travel times estimated from ocean noise cross-correlations," *20th International Congress on Acoustics, ICA*, no. August, pp. 1–6, 2010.

[122] "OALIB." https://oalib-acoustics.org/.

[123] J. Elfring, E. Torta, and R. V. D. Molengraft, "Particle Filters : A Hands-On Tutorial," *Sensors (Basel, Switzerland)*, vol. 21, no. 438, pp. 1–28, 2021.

[124] A. Doucet and A. M. Johansen, "A Tutorial on Particle Filtering and Smoothing: Fifteen years later," *Oxford Handbook of Nonlinear Filtering*, vol. 12, 2009.

[125] S. C. Surace, A. Kutschireiter, and J.-P. Pfister, "How to Avoid the Curse of Dimensionality Scalability of Particle Filters with and without Importance Weights," *Society for Industrial and Applied Mathematics Review*, vol. 61, no. 1, pp. 79–91, 2017.

[126] P. M. Djuric and M. F. Bugallo, "Particle filtering for high-dimensional systems," in *2013 5th IEEE International Workshop on Computational Advances in Multi-Sensor Adaptive Processing, CAMSAP 2013*, pp. 352–355, 2013.

[127] Z. L. Husz, A. M. Wallace, and P. R. Green, "Tracking with a hierarchical partitioned particle filter and movement modelling," *IEEE Transactions on Systems, Man, and Cybernetics, Part B: Cybernetics*, vol. 41, pp. 1571–1584, dec 2011.

[128] R. Douc, O. Cappé, and E. Moulines, "Comparison of resampling schemes for particle filtering," in *Image and Signal Processing and Analysis, 2005. ISPA 2005. Proceedings of the 4th International Symposium*, vol. 2005, pp. 64–69, 2005.

[129] T. Li, M. Bolić, and P. M. Djurić, "Resampling Methods for Particle Filtering: Classification, implementation, and strategies," *IEEE Signal Processing Magazine*, vol. 32, no. 3, pp. 70–86, 2015.

[130] "Hindcast - MetOceanView." https://app.metoceanview.com/hindcast/.